



Aalborg Universitet

AALBORG UNIVERSITY  
DENMARK

## Structure, Phase Transitions, and Dynamics in Four Special Oxide Glass Systems

Liu, Hao

*Publication date:*  
2018

*Document Version*  
Publisher's PDF, also known as Version of record

[Link to publication from Aalborg University](#)

*Citation for published version (APA):*

Liu, H. (2018). *Structure, Phase Transitions, and Dynamics in Four Special Oxide Glass Systems*. Aalborg Universitetsforlag. Ph.d.-serien for Det Ingeniør- og Naturvidenskabelige Fakultet, Aalborg Universitet

### General rights

Copyright and moral rights for the publications made accessible in the public portal are retained by the authors and/or other copyright owners and it is a condition of accessing publications that users recognise and abide by the legal requirements associated with these rights.

- Users may download and print one copy of any publication from the public portal for the purpose of private study or research.
- You may not further distribute the material or use it for any profit-making activity or commercial gain
- You may freely distribute the URL identifying the publication in the public portal -

### Take down policy

If you believe that this document breaches copyright please contact us at [vbn@aub.aau.dk](mailto:vbn@aub.aau.dk) providing details, and we will remove access to the work immediately and investigate your claim.



**STRUCTURE, PHASE TRANSITIONS,  
AND DYNAMICS IN FOUR SPECIAL  
OXIDE GLASS SYSTEMS**

**BY  
HAO LIU**

DISSERTATION SUBMITTED 2018



**AALBORG UNIVERSITY**  
DENMARK



# **STRUCTURE, PHASE TRANSITIONS, AND DYNAMICS IN FOUR SPECIAL OXIDE GLASS SYSTEMS**

by

Hao Liu



**AALBORG UNIVERSITY**  
DENMARK

Dissertation submitted 2018

Dissertation submitted: January, 2018

PhD supervisor: Professor Yuanzheng Yue,  
Aalborg University, Denmark

PhD committee: Associate Professor Casper Steinmann Svendsen (chair.)  
Aalborg University, Denmark

Professor Pierre Lucas  
University of Arizona, USA

Professor Alex Hannon  
Rutherford Appleton Laboratory, UK

PhD Series: Faculty of Engineering and Science, Aalborg University

Department: Department of Chemistry and Bioscience

ISSN (online): 2446-1636  
ISBN (online): 978-87-7210-137-8

Published by:  
Aalborg University Press  
Langagervej 2  
DK – 9220 Aalborg Ø  
Phone: +45 99407140  
aauf@forlag.aau.dk  
forlag.aau.dk

© Copyright: Hao Liu

Printed in Denmark by Rosendahls, 2018

## PREFACE AND ACKNOWLEDGEMENTS

This thesis has been submitted to the Faculty of Engineering and Science, Aalborg University in partial fulfillment of the Ph.D. degree. The thesis is based on the submitted or published scientific papers which are listed in Section 1.3. The Ph.D. study was carried out from December 2014 to March 2018. The work was primarily conducted at the Section of Chemistry at Aalborg University, with an external stay at State Key Laboratory of Silicate Materials for Architectures at Wuhan University of Technology for three months. The study was financed by both China Scholarship Council and Aalborg University.

I highly appreciate my supervisor Yuanzheng Yue for his dedicated supervision, stimulating discussions, and insightful suggestions. He has brought me to the fascinating world of glass science. His ardent encouragement has facilitated me to work enthusiastically and independently. I have truly enjoyed my Ph.D. study and look forward to collaborating with you on glass science and other projects in the future. Appreciation also goes to Professor G. Neville Greaves from University of Cambridge for fruitful discussions and advices. His persistent spirit on science has inspired me to work hard and efficiently.

I also acknowledge Professors Xiujian Zhao and Haizheng Tao from Wuhan University of Technology in China, who made the recommendation for me to come to Denmark for this degree. They have provided insights into glass science during my external stay. My colleagues from Wuhan University of Technology, Ang Qiao, Zhitao Shan, and Sheng Feng also deserve to be appreciated for performing various measurements and helpful discussions. I wish to keep long term collaboration in the future.

My kind acknowledgements also go to Professor MSO Morten M. Smedskjaer from Aalborg University for his support in paper writing and valuable discussions on glass issues. Guest researchers Yuebo Hu and Shujiang Liu are acknowledged for useful discussions and encouragement. Immense appreciation goes to my colleagues at Aalborg University: Mouritz Nolsøe Svenson, Rasmus Rosenlund Petersen, Christian Hermansen, Georgiana-Laura Paraschiv, René Mossing Thomsen, Ali Farsi, Qiuju Zheng, Saurabh Kapoor, Nerea Mascaraque, Martin Jensen, Kacper Januchta, Chao Zhou, Yang Shen, Jiayan Zhang, Usuma Naknikham, Martin Bonderup Østergaard, Tobias Kjær Bechgaard, Sonja Haastrup, Malwina Stępniewska, Katie Kedwell, and Chengwei Gao for great assistance and helpful discussions during my Ph.D. study.

Finally, special thanks go to my family, particularly my wife Yujie Liao. They have continuously supported and encouraged me to be confidence and gain renewed motivation throughout the project. This thesis is dedicated to them.

## ENGLISH SUMMARY

The mechanism of phase transition and the composition-structure-property relation are critical for understanding the nature of glass transition and for designing glasses with improved properties. However, these issues have not been fully understood owing to the non-equilibrium nature and structural complexity of glasses. The goal of this Ph.D. project is to explore the structure, phase transition, and dynamics of four special oxide glasses and liquids. Based on the classification of glass network former and modifier, we investigate the following: modifier-free system ( $\text{B}_2\text{O}_3\text{-Al}_2\text{O}_3\text{-SiO}_2\text{-P}_2\text{O}_5$ ), modifier-containing systems ( $\text{Na}_2\text{O-CaO-B}_2\text{O}_3\text{-SiO}_2$ ,  $\text{GeO}_2\text{-BaF}_2\text{-AlF}_3$ ), and network former free system ( $\text{CaO-Al}_2\text{O}_3$ ).

For  $\text{B}_2\text{O}_3\text{-Al}_2\text{O}_3\text{-SiO}_2\text{-P}_2\text{O}_5$  system, studied glasses exhibit nano-phase separation, i.e., a droplet phase (50-100 nm) and a matrix phase. The droplet contains boroxol rings and the matrix involves the B-O-Si network. With the substitution of  $\text{SiO}_2$  by  $\text{B}_2\text{O}_3$ , the content of boroxol rings increases in the droplet, and the matrix becomes boron-rich, giving rise to the decrease of glass transition temperatures ( $T_g$ ) of both phases. Furthermore, it is found that ordered domains form in the matrix during heat treatment, implying the structural heterogeneity of the system.

For  $\text{Na}_2\text{O-CaO-B}_2\text{O}_3\text{-SiO}_2$  system, the configurational heat capacity at  $T_g$  ( $C_{p,\text{conf}}(T_g)$ ) increases non-linearly with the substitution of  $\text{SiO}_2$  by  $\text{B}_2\text{O}_3$ . It is discovered that superstructures in the intermediate range order (IRO) govern the major increase of  $C_{p,\text{conf}}(T_g)$  with composition. Furthermore, the configurational entropy at  $T_g$  is mainly governed by IRO superstructures and angular constraints of O-B-O and O-Si-O bonds. For  $\text{GeO}_2\text{-BaF}_2\text{-AlF}_3$  system, nano-clusters (~20 nm) form in the supercooled region (925-986 K). The nano-clusters undergo a reversible order-disorder transition upon heating. The formation and breaking-down of the nano-cluster are associated with the germanium speciation, giving rise to the non-monotonic variation of  $T_g$  with the maximum temperature of dynamic heating.

For  $\text{CaO-Al}_2\text{O}_3$  system, viscosity and density of both stable and metastable liquids are determined using the aerodynamic levitation technique. With the substitution of  $\text{Al}_2\text{O}_3$  by  $\text{CaO}$ , the structural network evolves from oxygen deficient network, through continuous random network at the eutectic (C12A7), to  $[\text{AlO}_4]$  incomplete network, leading to the low-energy atomic packing of C12A7. This structural evolution gives rise to non-monotonic variations of  $T_g$ , thermal expansion, and glass forming ability across the binary system, featuring a threshold at C12A7. Furthermore, these extremely poor glass-forming liquids undergo dynamic fragile-to-strong transitions in the supercooled region upon cooling. Interestingly, considering the four studied systems together, it is found that structural ordering, nano-cluster formation, crystallization, order-disorder transition, and abnormal dynamics take place in the temperature region of  $1.15\text{-}1.2T_g$ .



## DANSK RESUME

Faseovergangsmekanismen samt relationer mellem den kemiske sammensætning, strukturen og egenskaberne er kritisk vigtige for forståelsen af glasovergangen og for at designe glasser med forbedrede egenskaber. Disse aspekter er dog endnu ikke fuldt forståede, hovedsagligt grundet glassernes ude-af-ligevægt tilstand og deres strukturel kompleksitet. Målet med denne afhandling er at udforske strukturen, faseovergangene, og dynamiske egenskaber af fire bestemte oxidglasser og glasdannende væsker. Baseret på opdelingen af glasbestanddele i netværksdannere og netværks-modificerende elementer undersøger vi følgende: et ikke-modificeret system ( $\text{B}_2\text{O}_3\text{-Al}_2\text{O}_3\text{-SiO}_2\text{-P}_2\text{O}_5$ ), to modificerede systemer ( $\text{Na}_2\text{O-CaO-B}_2\text{O}_3\text{-SiO}_2$  og  $\text{GeO}_2\text{-BaF}_2\text{-AlF}_3$ ) samt et netværksdannerfrit system ( $\text{CaO-Al}_2\text{O}_3$ ).

For  $\text{B}_2\text{O}_3\text{-Al}_2\text{O}_3\text{-SiO}_2\text{-P}_2\text{O}_5$  systemet, de undersøgte glasser udviser nano-fase separation, dvs. en dråbefase (50-100 nm) og en matrixfase. Dråberne indeholder boroxol-ringe mens matrixen indeholder et B-O-Si netværk. Som følge af udskiftningen af  $\text{SiO}_2$  med  $\text{B}_2\text{O}_3$  stiger indholdet af boroxol-ringene i dråberne, mens matrixfasen bliver rigere på bor, hvilket resulterer i et fald i glasovergangstemperaturen ( $T_g$ ) af begge faser. Det er fundet, at ordnede domæner dannes i matrixen under opvarmning, hvilket antyder strukturel heterogenitet af systemet.

For  $\text{Na}_2\text{O-CaO-B}_2\text{O}_3\text{-SiO}_2$  systemet, den konfigurationelle varmekapacitet ved  $T_g$  ( $C_{p,\text{conf}}(T_g)$ ) stiger nonlinear med udskiftningen af  $\text{SiO}_2$  med  $\text{B}_2\text{O}_3$ . Det er opdaget, at superstrukturer i mellemrækkende orden (MRO) styrer stigningen af  $C_{p,\text{conf}}(T_g)$  med sammensætningen. Derudover er den konfigurationelle entropi ved  $T_g$  hovedsagligt styret af MRO og bindingsbegrænsninger af O-B-O samt O-Si-O. For  $\text{GeO}_2\text{-BaF}_2\text{-AlF}_3$  systemet, nanodomæner (~20 nm) dannes i det underafkølede temperaturspænd (925-986 K). Nanodomænerne undergår en reversibel orden-uorden overgang under opvarmning. Dannelsen og ødelæggelsen af nanodomænerne er forbundet med germanium-fordelingen, resulterende i en nonmonotonisk variation af  $T_g$  med den højeste temperatur for dynamisk opvarmning.

For  $\text{CaO-Al}_2\text{O}_3$  systemet, viskositeten og densiteten af stabile og metastabile væsker er bestemt vha. en aerodynamisk levitationsteknik. Som følge af udskiftningen af  $\text{Al}_2\text{O}_3$  med  $\text{CaO}$ , det strukturelle netværk omdannes fra et oxygen-manglende netværk, via en kontinuerlig tilfældig netværk ved det eutektiske punkt (C12A7), til  $[\text{AlO}_4]$  ukomplet netværk, resulterende i en lav-energi atomisk pakning af C12A7. Denne strukturelle evolution medfører nonmonotoniske variationer af  $T_g$ , termisk ekspansion og glasdannende egenskaber på tværs af det binære system indtil en grænse ved C12A7. Derudover undergår disse ekstremt dårligt glasdannende væsker en fragil-stærk overgang i det underafkølede domæne ved nedkøling. Ved at betragte disse fire systemer, er det fundet at strukturel orden, nanodomænedannelsen, orden-uorden overgange samt abnormalt dynamik eksisterer i  $1.15\text{-}1.2T_g$  spændet.

# TABLE OF CONTENTS

<b>Chapter 1. Introduction.....</b>	<b>1</b>
1.1. Background and Challenges.....	1
1.2. Objectives.....	3
1.3. Thesis Content.....	3
<b>Chapter 2. Glass Structure.....</b>	<b>5</b>
2.1. Simple Oxide Glasses .....	5
2.2. Borate-Silicates Glasses .....	7
2.3. Mixed Network Former Glasses .....	11
2.4. Oxyfluoride Germanate Glasses.....	16
2.5. Calcium Aluminate Glasses .....	18
<b>Chapter 3. Phase Transitions.....</b>	<b>24</b>
3.1. Borate-Silicate Glasses.....	24
3.2. Mixed Network Former Glasses .....	26
3.3. Oxyfluoride Germanates Glasses .....	31
3.4. Calcium Aluminate Glasses .....	34
<b>Chapter 4. Dynamics.....</b>	<b>36</b>
4.1. Borate-Silicate Glasses.....	36
4.2. Mixed Network Former Glasses .....	38
4.3. Oxyfluoride Germanate Glasses.....	39
4.4. Calcium Aluminate Glasses .....	40
<b>Chapter 5. Correlation between Structure, Phase Transitions, and Dynamics.....</b>	<b>47</b>
5.1. Borate-Silicate Glasses.....	47
5.2. Mixed Network Former Glasses .....	49
5.3. Oxyfluoride Germanate Glasses.....	50
5.4. Calcium Aluminate Glasses .....	53
<b>Chapter 6. General Discussion and Perspective .....</b>	<b>58</b>
<b>Chapter 7. Conclusion .....</b>	<b>61</b>
<b>Chapter 8. Bibliography .....</b>	<b>63</b>

# CHAPTER 1. INTRODUCTION

Glass is a fascinating material, which has been attracting the interests of scientists, engineers and users. It is not only used in daily life as window and cookware, but also in high-tech applications, e.g., as photonic material. Although the technology of glass production is gradually mature, advanced technologies and new types of glasses are still being developed.

Unlike crystal, glass is a “solid” that lacks of long range order (LRO) and translational periodicity, and exhibits glass-liquid transition upon heating [1-3]. Various methods have been developed to prepare glasses, e.g., sol-gel, chemical vapor deposition, and ball-milling [2,4], while the most widely used one is melt-quenching. When heating a crystal above its melting temperature ( $T_m$ ), an equilibrium liquid forms by virtue of the first order phase transformation. In contrast, the liquid will become supercooled upon cooling below  $T_m$ . The supercooled liquid is a metastable state in the view of thermodynamics, which means it always tend to transform to a stable state, i.e., crystal. However, if the cooling rate is high enough to bypass macroscopic crystallization, the relaxation time of the supercooled liquid will exponentially increase upon cooling and finally exceed the timescale of experimental observation, leading to the frozen-in of the supercooled liquid, and hence, the formation of the glass [5]. Being one kind of amorphous solids, the essential feature of a glass is an abrupt change of the second derivative of enthalpy and volume upon heating through glass transition region, i.e., the increase of isobaric heat capacity ( $C_p$ ) and coefficient of thermal expansion (CTE), respectively. Therefore, the presence of glass transition distinguishes glass from other amorphous solids, and is normally characterized by glass transition temperature ( $T_g$ ). The widely accepted definition of  $T_g$  for oxide glasses is the temperature where the viscosity of the supercooled liquid is  $10^{12}$  Pa s [6-8]. Upon cooling from  $T_m$  to  $T_g$ , the dynamics (i.e., viscosity and relaxation time) increase several orders of magnitude, whereas the structural evolution in this temperature region is undetectable or moderate. Besides, for a series of glass forming liquids, variations of dynamics and thermo-physical properties with composition and temperature are complex when supercooled liquids approaching  $T_g$ , e.g., non-linear and/or non-exponential [9,10]. Hence, exploring structural origins of dynamics and thermo-physical properties for glasses and liquids is still a challenge, and the composition-temperature-structure-property relation need to be well understood in various systems.

## 1.1. BACKGROUND AND CHALLENGES

The field of glass science and technology broadens rapidly, and it offers researchers a variety of open questions. Important issues include the basic nature of glass transition and whether it is general for various systems. To explore the condition a liquid can form glass by melt-quenching, glass forming ability (GFA) is proposed

and original characterized by critical cooling rate ( $q_{\text{crit}}$ ), i.e., the lowest cooling rate for glass formation [11-14]. Since the determination of  $q_{\text{crit}}$  is difficult and time-consuming, a number of parameters have been proposed to indirectly reflect GFA, such as the  $T_g/T_m$  ratio, the difference in free energy between liquid and solid, and the liquid viscosity at  $T_m$  [15]. Nevertheless, structure and bonding are essential factors to determine how ease the liquid can form glass. Furthermore, structural evolutions with composition and temperature are fundamental to design glasses with outstanding properties.

For oxide glasses, cations within the glass network are categorized by three types in the view of bonding character: network former, network modifier, and network intermediate. Network formers, e.g., B, Si, P, and Ge, are covalently bonded with oxygen to form polyhedra, constituting the framework of glass structure. In contrast, network modifiers change the topology and the connectivity of the glass network by virtue of the formation of ionic bonds with oxygen. For some oxide glasses such as aluminate and borate glasses, modifier cations play dual roles: in charge balancing network polyhedra such as  $[\text{BO}_4]^-$  and  $[\text{AlO}_4]^-$ ; in modifying the glass network by the formation of non-bridge oxygen (NBO). Network intermediate behaves in a way between network former and modifier, highly relying on the environment of network intermediate. Although a variety of glass systems have been thoroughly studied, the correlation between structure and properties for various glass systems has not been holistically explored. Therefore, it is necessary to make a comprehensive comparison among these correlations for entirely different glass systems. In this thesis, we choose four special glass systems: traditional oxide glass system containing both network former and network modifier ( $\text{Na}_2\text{O}-\text{CaO}-\text{B}_2\text{O}_3-\text{SiO}_2$ ); mixed network former glass system without typical network modifier ( $\text{B}_2\text{O}_3-\text{Al}_2\text{O}_3-\text{SiO}_2-\text{P}_2\text{O}_5$ ); germanate glass system with partial substitution of fluoride for oxide ( $\text{BaF}_2-\text{AlF}_3-\text{GeO}_2$ ); binary oxide glass system without typical network formers ( $\text{CaO}-\text{Al}_2\text{O}_3$ ).

Besides the structure, dynamics and thermodynamics of glasses and liquids are critical for understanding the origin of glass transition. Upon cooling from  $T_m$  to  $T_g$ , the viscosity increases in an Arrhenius or non-Arrhenius way with temperature for different liquids. Angell proposed a classification based on these varied behaviors of viscosity, i.e., liquid fragility [16,17]. The liquid fragility describes how fast the viscosity increases upon cooling, and is quantified by liquid fragility index  $m$ , i.e., the slope of  $\log \eta \sim T_g/T$  curve at  $T_g$ . More fragile the liquid is, bigger  $m$  is. It is meaningful to explore how composition and structure influence  $m$ , providing opportunity to understand the mechanism of viscous flow. Moreover, the relation between liquid fragility and thermodynamics such as configurational heat capacity ( $C_{p,\text{conf}}$ ) and configurational entropy ( $S_{\text{conf}}$ ), is important. Although many studies obtained fruitful achievement [18-20], how to correlate these properties with structure in different systems is still a challenge. In addition, the ordered length scale of structure in glasses and liquids is not limited below 0.5 nm, i.e., short range order

(SRO). Ordered structures such as rings and superstructures have been observed in the length scale of 0.5-2 nm, i.e., intermediate range order (IRO) [21-24]. It is worthwhile to explore the influence of IRO structure on properties and interactions of different IRO structures for glasses and liquids. Revealing these correlations in various systems is helpful to design glasses with optimized properties by modifying compositions and controlling thermal histories. Moreover, these relations are helpful to understand the fundamental physics governing the glass transition.

## 1.2. OBJECTIVES

The objectives of the present Ph.D. thesis are summarized as follows:

1. Reconcile the evolution of structure and thermodynamics with composition during glass transition region.
2. Explore the structure and the dynamics of liquids in stable and metastable states.
3. Investigate the influence of structural heterogeneity on crystallization, phase separation, and phase transition in glasses and supercooled liquids.
4. Clarify the correlation between structure, dynamics, and thermo-physical properties of various supercooled liquids.

## 1.3. THESIS CONTENT

This thesis is presented as a plurality, including an introductory overview followed by four journal papers (either published or submitted for publication). These papers constitute the main body of the thesis, and will be referred to by their roman numerals:

- I. H. Liu, M.M. Smedskjaer, H.Z. Tao, L.R. Jensen, X.J. Zhao, and Y.Z. Yue, “A medium range order structural connection to the configurational heat capacity of borate–silicate mixed glasses”, *Physical Chemistry Chemical Physics*, **18**, 10887 (2016). DOI: 10.1039/c6cp00749j
- II. H. Liu, R.E. Youngman, S. Kapoor, L.R. Jensen, M.M. Smedskjaer, Y.Z. Yue, “Nano-phase separation and structural ordering in silica-rich mixed network former glasses”, *J. Phys. Chem. B*, (under review).
- III. H. Liu, Y.B. Hu, Y.Z. Yue, “Nano-cluster formation in supercooled oxyfluoride germanate liquids”, *J. Am. Ceram. Soc.*, (under review)

- IV. H. Liu, R.K. Pan, W.L. Chen, Z.T. Shan, A. Qiao, J.W.E. Drewitt, L. Henet, S. Jahn, D.P. Langstaff, H.Z. Tao, G.N. Greaves, Y.Z. Yue, "Reconciling rheology, phase transitions and structure across the extensive cementitious calcium-aluminate melts and glasses", (to be submitted).

# CHAPTER 2. GLASS STRUCTURE

Since a variety of glass properties strongly rely on their compositions, it is critical for understanding the structure of glass. Several theories have been proposed, such as Zachariasen's Continuous Random Network Model (CRN) [25], Greaves's Modified Random Network (MRN) [26], Compensated continuous random network model (CCRN) [27], and Phillips' network constraint theory [28]. As classified in Section 1.1, typical network formers include  $\text{SiO}_2$ ,  $\text{B}_2\text{O}_3$ ,  $\text{P}_2\text{O}_5$ , and  $\text{GeO}_2$ . Alkali and Alkaline-earth oxides belong to typical network modifiers, and  $\text{Al}_2\text{O}_3$  is one kind of network intermediates. The general structure of glasses with simple composition will be briefly discussed, and afterwards we will focus on the structure of four special oxide glasses.

Compare to a crystal, the most remarkable difference in the structure of a glass is the lack of symmetry and periodicity in glass network. However, the short-range order of a glass is similar to the crystal with the same chemical composition, and hence can be well-defined and fully discussed in terms of the polyhedra of network former cations. It is manifested that bond lengths and angles within the polyhedra only vary in a narrow range [3]. The disorder of glasses is partly reflected by the broad statistical distribution of inter-polyhedral angles, dihedral angles, and a variety of types and sizes of rings which consist of the polyhedra [3]. In oxide glasses, most network former cations covalently bond with 3 or 4 oxygen to form triangle plane or tetrahedra, which constitute the glass network. Oxygen is distinguished by bridging oxygen (BO) and non-bridging oxygen (NBO), which is linked to two and one network former cation, respectively. The formation of NBO normally results from the addition of network modifier to the glass network.

## 2.1. SIMPLE OXIDE GLASSES

Among oxide glasses, silicate glasses are studied most extensively due to their widespread applications, ranging from window glass to optical fibres [3,29-32]. The network of silica glass at ambient pressure consists of  $\text{SiO}_4$  tetrahedra without NBO. Its distribution of O-Si-O angle within tetrahedra (maximum at  $109.7^\circ$ ) is similar as that of  $\text{SiO}_2$  crystal, while its distribution of Si-O-Si angle between tetrahedra (varies from  $120^\circ$  to  $180^\circ$  and maximum at  $144^\circ$ ) is much broader than that of  $\text{SiO}_2$  crystal [3,33]. The addition of alkali and/or alkaline-earth oxides partially breaks the silicate network by virtue of the formation of NBO [34-36]. As the content of modifier increases,  $\text{SiO}_4$  tetrahedra are gradually converted from  $\text{Si}(\text{Q}^4)$  ( $\text{SiO}_4$  tetrahedra with 4 BO) to  $\text{Si}(\text{Q}^3)$ ,  $\text{Si}(\text{Q}^2)$ ,  $\text{Si}(\text{Q}^1)$ , and  $\text{Si}(\text{Q}^0)$ , i.e., depolymerization of the silicate network.

$\text{P}_2\text{O}_5$  is another typical network former. The high valence electron of  $\text{P}^{5+}$  causes the existence of terminal oxygen (TO) and the formation of P=O double bond in  $\text{PO}_4$

tetrahedra [3,37-40]. It should be noted that this short P=O bond is different with P-NBO bond because of its significant  $\pi$ -bond character, arising from the additional valence electron of  $P^{5+}$  [39,40]. When modifiers enter phosphate network, BO is progressively converted to NBO [39,40]. Furthermore, TO and NBO becomes indistinguishable, which is a result of  $\pi$ -bond delocalization [39,40]. The sequential depolymerization of phosphate network with the addition of network modifier oxides is similar as that for silicate network.

Although  $B_2O_3$  is also a typical glass former, boron trioxide and borate glasses behave differently compared with  $SiO_2$  glasses. For instance,  $B_2O_3$  glasses exhibits low glass transition temperature  $T_g$  (515-575 K) and moderate liquid fragility ( $m=40$ ), whereas  $SiO_2$  glass has high  $T_g$  (1500 K) and low  $m$  (20) [3,18]. Furthermore,  $B_2O_3$  glass consists of a large amount of planar boroxol rings ( $B_3O_6$ ) which are connected by each other or non-ring  $BO_3$  triangles [3,41,42]. Supercooled  $B_2O_3$  liquid hardly crystallize under ambient pressure, because it needs significant structural rearrangement to form  $B_2O_3$  crystal which is totally lack of boroxol ring [3]. When network modifier is added into  $B_2O_3$  glass, three-fold coordinated boron ( $B^{III}$ ) species will be firstly converted to four-fold coordinated boron ( $B^{IV}$ ) species to form  $BO_4$  tetrahedra, which is charge compensated by modifier cations. If the fraction of  $B^{IV}$  reaches a critical value, the excess modifier leads to the formation of NBO with the consumption of  $BO_4$  tetrahedra. In borate glasses, NBO is energetically favorable to bond with  $B^{III}$  rather than  $B^{IV}$  [3,9]. The conversion between  $B^{III}$  and  $B^{IV}$  species causes abnormal changes of physical and thermal properties of glasses, which is called “boron anomaly”. For example, the initial addition of alkali and/or alkaline earth oxides results in an increase of  $T_g$  and a decrease of coefficient of thermal expansion (CTE), while further addition of network modifiers produces opposite trends [18,43,44]. The composition where threshold of property occurs depends on types of network modifiers.

The structure of  $GeO_2$  glass is quite similar as that of  $SiO_2$  glass, i.e., consists of  $GeO_4$  tetrahedra [3,45]. The bond length of Ge-O is larger than that of Si-O and the bond angle of Ge-O-Ge is smaller than that of Si-O-Si, leading to the relative high concentration of structural defects and Ge-Ge bonds in  $GeO_2$  glass compared to  $SiO_2$  glass [1-3]. As modifier oxides are initially added to  $GeO_2$  glass, part of four-fold coordinated Ge ( $Ge^{IV}$ ) species are transformed to five- or six-fold coordinated Ge ( $Ge^V$  or  $Ge^{VI}$ ) species [3,45-47].  $Ge^{V,VI}$  species prefer to connect with  $GeO_4$  tetrahedra through corner-shared oxygen by occupying low energy state instead of bonding with other  $Ge^{V,VI}$  polyhedra [47]. Furthermore, the long bond of Ge-O has effects on the environment of modifier cations in the network, giving rise to the formation of 6-membered rings and cavities where modifier cations might stay in when modifiers are initially added [3,45-47]. After the contents of isolated polyhedra ( $GeO_5$  and  $GeO_6$ ) and 6-membered rings saturate, further increase of modifier oxides causes three main structural changes, the conversion from  $Ge^{V,VI}$  back to  $Ge^{IV}$ , the formation of NBO in  $GeO_4$  tetrahedra, and the break of 6-



membered rings. These changes of germanate structural units have significant effects on glass properties, i.e., “germanate anomaly”, which is similar as “boron anomaly” [45,47].

## 2.2. BORATE-SILICATE GLASSES

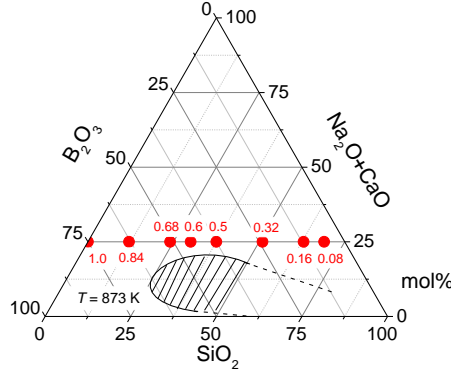
Borate-silicate mixed glass plays an important role in daily life and technologies due to their outstanding properties such as low CTE, high thermal and chemical resistance, and low dielectric constant [48-51]. Although the structure of borate-silicate mixed glasses is complex, the SRO structure have been studied previously by performing Raman spectroscopy, nuclear magnetic resonance (NMR), X-ray and neutron diffraction [48,52-56]. Basically, if  $B_2O_3$  enters silicate network together with network modifiers, there is a competition between  $BO_3$  triangles and  $SiO_4$  tetrahedra to bond with modifier cations, i.e., a competition between the formation of  $BO_4$  tetrahedra and that of NBO. The distribution of modifier cations and the fraction of specific structural units depend on the content and type of the modifier [52,53,57]. Based on the classic model proposed by Yun and Bray [21,58], a vast of studies explored the structural evolution of boron and silicon species with composition in various borate-silicate mixed glasses. It is found that modifier anions prefer to stay in borate network instead of silicate network if the modifier is insufficient [21,58-61]. However, more recent investigations inferred that modifier anions could be more randomly distributed between the silicate and borate network [62]. Moreover, many studies showed that the thermal history of glasses plays a critical role in determining the fraction of structural units. For example,  $B^{III}$  species are more favorable in the glass having high fictive temperature, and  $B^{IV}$  species form upon annealing for borosilicate glass fibers [59,63,64]. Recently, Smedskjaer *et al.* have explored the structural evolution of  $Na_2O$ - $CaO$ - $B_2O_3$ - $SiO_2$  glasses with varying  $B_2O_3/SiO_2$  ratio and successfully predicted glass properties by using two-state model and temperature-dependent constraint theory, respectively [18]. However, besides SRO structural units, borate-silicate mixed glasses also contain abundant intermediate range order (IRO) structural units, i.e., superstructures [21-24,54,65-70]. Studies of Raman spectroscopy and neutron scattering verified the existence of various IRO superstructures containing  $B^{IV}$  throughout the compositional region of alkali borate glasses, giving rise to the multiple four-fold coordinated boron sites [23,24,65-67]. It is also implied that IRO superstructures and mixed Si-O-B units exist in borosilicate glasses [21,22]. Nevertheless, the evolution of IRO structure with composition has not yet been well understood for  $Na_2O$ - $CaO$ - $B_2O_3$ - $SiO_2$  glasses.

Table 2-1 shows the nominal chemical compositions of the studied glasses  $15Na_2O$ - $10CaO$ -( $75q$ ) $B_2O_3$ -( $75(1-q)$ ) $SiO_2$ , where  $q$  represents the mole ratio of  $[B_2O_3]/([B_2O_3]+[SiO_2])$ . The details of glass preparation and characterization are described in Paper I. Fig. 2-1 shows the ternary phase diagram of  $(Na_2O+CaO)$ - $B_2O_3$ - $SiO_2$  obtained from [71]. Due to the existence of multiple network formers,

there is a potential for borate-silicate mixed glasses to exhibit phase separation which significantly affect glass properties [29,72-75]. Although some compositions ( $q=0.5, 0.6$  and  $0.68$ ) are close to the boundary of phase separation region at 873 K, the Raman spectra performed on each sample with five different surface locations exhibit no differences. This confirms that there is no phase separation above size limit of Raman laser ( $\sim 10$   $\mu\text{m}$ ) in all studied glasses. Furthermore, differential scanning calorimetry (DSC) curves are reproducible for each glass (Fig. 3 in Paper I), again verifying that studied glasses show no phase separation.

**Table 2-1** Nominal chemical compositions of  $15\text{Na}_2\text{O}-10\text{CaO}-(75q)\text{B}_2\text{O}_3-(75(1-q))\text{SiO}_2$  glasses.  $R$  and  $K$  values are the molar ratio of  $([\text{Na}_2\text{O}]+[\text{CaO}])/[\text{B}_2\text{O}_3]$  and  $[\text{SiO}_2]/[\text{B}_2\text{O}_3]$ , respectively.

$q$	Nominal chemical composition (mol%)				$R$	$K$
	$\text{B}_2\text{O}_3$	$\text{SiO}_2$	$\text{Na}_2\text{O}$	$\text{CaO}$		
0.08	6	69	15	10	4.17	11.50
0.16	12	63	15	10	2.08	5.25
0.32	24	51	15	10	1.04	2.13
0.5	37.5	37.5	15	10	0.67	1.00
0.6	45	30	15	10	0.56	0.67
0.68	51	24	15	10	0.49	0.47
0.84	63	12	15	10	0.40	0.19
1.0	75	0	15	10	0.33	0



**Figure 2-1** Ternary phase diagram of  $(\text{Na}_2\text{O}+\text{CaO})\text{-B}_2\text{O}_3\text{-SiO}_2$  system obtained from [71]. The numbers refer to the sample ID,  $q$ . The shaded area is the region of isothermal bimodal phase separation at 873 K.

Fig. 2-2 shows the full range ( $250\text{-}1650\text{ cm}^{-1}$ ) Raman spectra of the studied  $\text{Na}_2\text{O}\text{-CaO-B}_2\text{O}_3\text{-SiO}_2$  glasses. In general, the Raman spectra are divided into three main regions: low-frequency ( $300\text{-}550\text{ cm}^{-1}$ ), medium-frequency ( $550\text{-}810\text{ cm}^{-1}$ ), and high-frequency ( $900\text{-}1600\text{ cm}^{-1}$ ) regions [42,76-80]. In the low-frequency region, the

Raman spectrum of each glass exhibits a broad band which is a sum of several Raman peaks. The structural assignments of these Raman peaks depend on composition. According to literature [24,59,61,63,64,70,76,81], for the silica-rich composition ( $q < 0.32$ ), the broad band mainly corresponds to the breathing vibrations of Si-O rings and the stretching and bending vibrations of Si-O-Si bonds. Peaks located at  $\sim 445$  and  $\sim 465$   $\text{cm}^{-1}$  arise from network deformation of large size and small size Si-O rings, respectively. The bands of  $\text{Si}(\text{Q}^4)$ ,  $\text{Si}(\text{Q}^3)$ , and  $\text{Si}(\text{Q}^2)$  appear at  $\sim 495$ ,  $\sim 540$ , and  $\sim 590$   $\text{cm}^{-1}$ , respectively. As the content of  $\text{B}_2\text{O}_3$  increases in the silica-rich compositions ( $q = 0.08$ - $0.32$ ), the broad band shifts towards lower frequency from  $\sim 580$  to  $\sim 500$   $\text{cm}^{-1}$ , implying the decrease of the number of NBO in  $\text{Si}(\text{Q}^n)$ . This is because some of the added boron is  $\text{B}^{\text{IV}}$  species which are charge compensated by modifiers. In addition, NBO is normally bonded to Si and  $\text{B}^{\text{III}}$  instead of  $\text{B}^{\text{IV}}$ , because NBO- $\text{B}^{\text{IV}}$  bonding will accumulate negative charges and induce modifier clusters which are not favorable in the view of thermodynamics. Further increase of  $\text{B}_2\text{O}_3$  content above  $q = 0.32$  leads to the partial conversion from Si-O-Si units to mixed  $\text{B}^{\text{III}}$ -O-Si units, and hence the broad band shifts from  $\sim 500$  to  $\sim 530$   $\text{cm}^{-1}$  [70]. In the high-frequency region, two separated broad bands appear in the region of 900-1200 and 1250-1600  $\text{cm}^{-1}$ , respectively [76]. The broad band in 900-1200  $\text{cm}^{-1}$  consists of multiple peaks attributed to various vibration modes, i.e., stretching vibration of Si-BO in  $\text{Si}(\text{Q}^3)$  and  $\text{Si}(\text{Q}^4)$ , the stretching vibration of  $\text{B}^{\text{III}}$ -O-Si bond, and the asymmetric stretching vibration of B-BO in  $\text{BO}_4$  tetrahedra. The two bands shift towards to lower frequency as increasing  $\text{B}_2\text{O}_3$  content. Furthermore, the band shape changes with composition, indicating that structural species vary as  $\text{B}_2\text{O}_3$  content increases. We infer that the vibration modes corresponding to these peaks gradually change from stretching vibrations of Si-BO in  $\text{Si}(\text{Q}^3)$  and  $\text{Si}(\text{Q}^4)$  to those of  $\text{B}^{\text{III}}$ -O-Si and  $\text{BO}_4$ . In boron-rich compositions, the evolution of the peaks with composition reflects the change in the ratio of  $\text{B}^{\text{IV}}$  to  $(\text{B}^{\text{III}} + \text{B}^{\text{IV}})$ , i.e.,  $N_4$  [23,70,82]. The band in 1250-1600  $\text{cm}^{-1}$  corresponds to the stretching vibrations of  $\text{BO}_3$  units. These  $\text{BO}_3$  units include major non-ring  $\text{BO}_3$  with one or two NBOs and minor  $\text{BO}_3$  in boroxol ring, which are characterized by peaks at  $\sim 1400$  and  $\sim 1250$   $\text{cm}^{-1}$ , respectively [83].

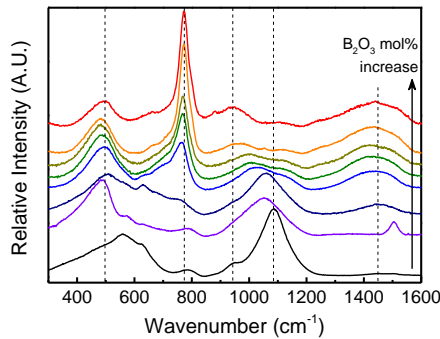


**Figure 2-2** Raman spectra for  $\text{Na}_2\text{O}$ - $\text{CaO}$ - $\text{B}_2\text{O}_3$ - $\text{SiO}_2$  glasses.

IRO structural units give rise to Raman peaks in the medium-frequency region [42,59,61,76,79]. We deconvolute the Raman spectra in 550-810  $\text{cm}^{-1}$  based on literature [23,24,48,84-86]. The method of Raman peak deconvolution and the assignments of deconvoluted peaks are described in Paper I. Fig. 2-3 shows the evolution of IRO structural units with varying  $q$  by assuming the integrated area of each deconvoluted Raman peak is approximately proportional to the content of its corresponding IRO structure [68,87,88]. As  $q$  increases, the content of the mixed B-O-Si network unit (danburite-like ring) first increases and then decreases. The presence of mixed B-O-Si units indicates that initially added boron are mainly in  $\text{B}^{\text{IV}}$  species and distribute in silicate network in a certain way rather than forming isolated clusters [61]. As the content of  $\text{B}^{\text{III}}$  increases, it is favorable for  $\text{BO}_4$  tetrahedra to bond with  $\text{B}^{\text{III}}$  to form borate superstructures instead of staying in the silicate network. This is confirmed by the formation of 6-membered borate rings with  $\text{B}^{\text{IV}}$  by consumption of mixed B-O-Si units with further increase of the  $\text{B}_2\text{O}_3$  content above  $q=0.32$ . Furthermore, the 6-membered borate ring is most sensitive to the  $\text{B}_2\text{O}_3/\text{SiO}_2$  ratio compared to other IRO units. Although  $N_4$  decreases as  $q$  increases [18,86,89,90], the content of  $\text{BO}_4$  tetrahedra increases with  $q$ , leading to the decrease of the fraction of  $\text{SiO}_4$  tetrahedra with NBOs (Fig. 2-2). This is consistent with the previous findings that when the ratio of  $\text{SiO}_2$  to  $\text{B}_2\text{O}_3$  is below 0.5, almost all modifier cations act as charge compensators for  $\text{B}^{\text{IV}}$  [58]. As the  $\text{B}_2\text{O}_3$  content increases,  $\text{Na}^+$  and  $\text{Ca}^{2+}$  cations accumulate around these structural units due to the negative charge localization.

Hence, we propose the structural evolution with varying  $\text{B}_2\text{O}_3/\text{SiO}_2$  ratio for  $\text{Na}_2\text{O}-\text{CaO}-\text{B}_2\text{O}_3-\text{SiO}_2$  glasses. In the silica-rich glasses, most of boron atoms are  $\text{B}^{\text{IV}}$  species bonded with  $\text{SiO}_4$  tetrahedra to form mixed B-O-Si units, which is a result of insufficiency of  $\text{B}^{\text{III}}$  species. As  $\text{B}_2\text{O}_3$  content increases, the fraction of  $\text{B}^{\text{III}}$  species increases, and hence borate superstructure rings form by consumption of mixed B-O-Si units. This indicates the distribution of  $\text{BO}_4$  units has a close correlation with the content of  $\text{BO}_3$  within borate ring. Meanwhile, the contents of chain- and ring-type metaborate groups vary non-monotonically with maximum at  $q=0.5$  and minimum at  $q=0.84$ , respectively, indicating there is a competition between the formation of  $\text{B}^{\text{IV}}$  species and NBO. As  $q$  increases above 0.6, 6-membered borate ring with  $\text{B}^{\text{IV}}$  becomes dominant among IRO structures, and almost all modifier cations are used to charge compensate  $\text{BO}_4$  units.

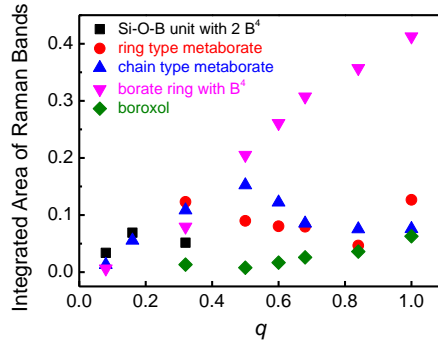


**Figure 2-3** Composition dependence of deconvoluted Raman peak area of various IRO units.

### 2.3. MIXED NETWORK FORMER GLASSES

Mixed network former glasses are technically important due to their low CTE and Young's modulus [91-99]. They also have high liquidus viscosities ( $>3 \times 10^4$  Pa s), which are advantageous for glass formation [91,96]. Furthermore, unique structural features occur in this kind of glasses, e.g., the preferred formation of  $\text{AlPO}_4$  and  $\text{BPO}_4$  units in which P bond to 4 BOs ( $\text{P}(Q^4)$ ) for ternary and quaternary mixed network former glasses [91,93,94,96]. It has been reported that there is a preference for Al-O-P compared to B-O-P association in  $\text{B}_2\text{O}_3$ - $\text{Al}_2\text{O}_3$ - $\text{SiO}_2$ - $\text{P}_2\text{O}_5$  quaternary glasses [91], whereas  $\text{BPO}_4$  units have higher priority to form than  $\text{AlPO}_4$  units in  $\text{B}_2\text{O}_3$ - $\text{Al}_2\text{O}_3$ - $\text{P}_2\text{O}_5$  ternary glasses [94]. However, the existence of these crystal-like structures ( $\text{AlPO}_4$  and  $\text{BPO}_4$ ) and multiple network formers could have great potential to cause phase separation for the mixed network former glasses, which have not been well understood. Therefore, we explored the structure of  $x\text{B}_2\text{O}_3$ - $4\text{Al}_2\text{O}_3$ -( $86-x$ ) $\text{SiO}_2$ - $10\text{P}_2\text{O}_5$  ( $x=17, 23, 25, 27, 29, 31$ ) glasses. The analyzed chemical compositions are shown in Table 2-2, which is in agreement with the nominal compositions.

**Table 2-2** Glass ID and corresponding analyzed chemical composition (mol%) of  $x\text{B}_2\text{O}_3$ - $4\text{Al}_2\text{O}_3$ -( $86-x$ ) $\text{SiO}_2$ - $10\text{P}_2\text{O}_5$  glasses.

Glass ID	Analyzed Composition (mol%)			
	$\text{SiO}_2$	$\text{B}_2\text{O}_3$	$\text{Al}_2\text{O}_3$	$\text{P}_2\text{O}_5$
B16	70	16.06	3.92	9.88
B22	64.3	22.05	3.81	9.78
B24	62.45	23.76	3.83	9.89
B26	60.33	25.86	3.83	9.91
B28	58.41	27.71	3.85	9.95
B30	56.09	29.97	3.84	10.03

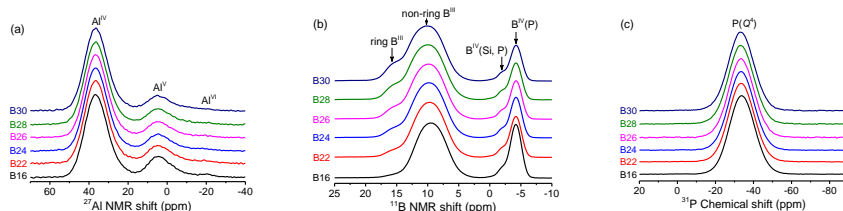
Fig. 2-4a shows the  $^{27}\text{Al}$  MAS NMR spectra of the studied glasses. For the B16 glass, the spectrum consists of three Al resonances centered around 38, 6 and -19 ppm, corresponding to four-, five-, and six-fold coordinated aluminum ( $\text{Al}^{\text{IV}}$ ,  $\text{Al}^{\text{V}}$ , and  $\text{Al}^{\text{VI}}$ ) environments, respectively. These resonances shift to higher shielding compared to those usually observed in aluminosilicate glasses. This is because the existence of P as the next-nearest neighbor (*NNN*) of  $\text{AlO}_x$  polyhedra and the higher electronegativity of P compared to that of Si [100]. This is illustrated by the close similarity of the resonance of  $\text{Al}^{\text{IV}}$  in these studied glasses and that in  $\text{AlPO}_4$  (~40 ppm) [91,101].  $\text{Al}^{\text{V}}$  and  $\text{Al}^{\text{VI}}$  species are present as charge-balancing polyhedra due to the lack of any traditional modifiers in studied glasses [102]. As increasing the  $\text{B}_2\text{O}_3$  content, the spectra remain unchanged in terms of peak positions but slight changes in Al coordination number occur, i.e., the population of  $\text{Al}^{\text{IV}}$  species increases and those of  $\text{Al}^{\text{V}}$  and  $\text{Al}^{\text{VI}}$  species. The resonance of  $\text{Al}^{\text{VI}}$  overlaps with the more intense resonance of  $\text{Al}^{\text{V}}$ . Moreover, the population of  $\text{Al}^{\text{VI}}$  species remains in the range of 2-3 % for all compositions. Therefore, it is difficult to quantify the fraction of  $\text{Al}^{\text{VI}}$  species for each composition. The estimated average coordination number of Al slightly decreases from 4.25 to 4.23 as the  $\text{B}_2\text{O}_3$  content increases.

Fig. 2-4b shows the  $^{11}\text{B}$  MAS NMR spectra, containing a broad line between 2-20 ppm and a narrow peak near -4 ppm, which correspond to the resonances of  $\text{B}^{\text{III}}$  and  $\text{B}^{\text{IV}}$  species, respectively. The deconvoluted  $\text{B}^{\text{III}}$  broad line has three unique resonances. Two of them correspond to ring and non-ring  $\text{B}^{\text{III}}$  species with isotropic chemical shifts of 17.5 and 14 ppm, respectively, which are typically observed in borosilicate glasses. The third peak at 12 ppm is attributed to  $\text{B}^{\text{III}}$  species with P *NNN*. As the  $\text{B}_2\text{O}_3$  content increases, the peak of ring  $\text{B}^{\text{III}}$  becomes more prominent. Specifically, approximately 4.6% of  $\text{B}^{\text{III}}$  species are in ring sites for B16 glass, increasing to 19.7 % for B30 glass.

The narrow peak near -4 ppm in  $^{11}\text{B}$  MAS NMR spectra consists of two resonances of  $\text{B}^{\text{IV}}$  species centered at -4.2 and -2.0 ppm, corresponding to  $\text{B}^{\text{IV}}$  species in  $\text{BPO}_4$  units and those with a mix of P and Si as *NNN*, respectively. As the  $\text{B}_2\text{O}_3$  content increases from B16 to B30 glass,  $N_4$  decreases from 26.8% to 17.5%. 82% of  $\text{B}^{\text{IV}}$  species are in  $\text{BPO}_4$  units for B16 glass, dropping to 78-80% for other glasses.

Fig. 2-4c shows  $^{31}\text{P}$  MAS NMR spectra, which is composition independent. Each spectrum can be fit with a single Gaussian peak at -33.7 ppm. The FWHM is approximately 16 ppm, and the peak position varies less than 0.5 ppm with the composition. This peak corresponds to the resonance of  $\text{P}(\text{Q}^4)$  ( $\text{PO}_4$  tetrahedra with 4 BOs) bonded to Al ( $\text{AlPO}_4$  units) and B ( $\text{BPO}_4$  units). The insensitivity of  $^{31}\text{P}$  MAS NMR spectra with composition indicates that changes in  $\text{B}_2\text{O}_3$  content do not significantly affect the phosphorus speciation. In addition, we cannot fully exclude the existence of other phosphate groups such as  $\text{P}(\text{Q}^3)$ , because they might be hidden by the  $\text{P}(\text{Q}^4)$  resonances. Furthermore, the breadth of the peak at -33.7 ppm makes it difficult to quantitatively resolve P speciation. Nevertheless,  $^{31}\text{P}$  MAS NMR spectra

verify that most P is in  $\text{AlPO}_4$  and  $\text{BPO}_4$  units, which is consistent with the results from  $^{27}\text{Al}$  and  $^{11}\text{B}$  MAS NMR spectra and previous studies [91].



**Figure 2-4** (a)  $^{27}\text{Al}$ , (b)  $^{11}\text{B}$ , and (c)  $^{31}\text{P}$  MAS NMR spectra of studied glasses. In (b),  $B^{IV}(\text{Si, P})$  represents  $\text{BO}_4$  tetrahedra with Si and P as NNN, while  $B^{IV}(\text{P})$  means  $B^{IV}$  species in  $\text{BPO}_4$  environments.

Fig. 2-5 shows the full range ( $200\text{--}1400\text{ cm}^{-1}$ ) Raman spectra of the studied mixed network former glasses. In general, the Raman spectrum of each glass consists of five bands and can be divided into three frequency regions [103-107]. In the low frequency region ( $200\text{--}620\text{ cm}^{-1}$ ), the intense peak at  $\sim 460\text{ cm}^{-1}$  is attributed to symmetric stretching vibration of Si-O-Si bond, while the shoulder at  $\sim 330\text{ cm}^{-1}$  is assigned to pyrophosphate-type species ( $\text{P}(Q^1)$ , i.e.,  $\text{PO}_4$  tetrahedra with 1 BO and 3 NBOs [103]. As the  $\text{B}_2\text{O}_3$  content increases, the intensity of the shoulder slightly decreases, indicating  $\text{P}(Q^1)$  species are partially converted to other phosphate species. In the medium frequency region ( $620\text{--}850\text{ cm}^{-1}$ ), there are two weak bands and one sharp peak in the region of  $660$ ,  $710$ , and  $805\text{ cm}^{-1}$ , respectively. According to literature, we infer that the first two bands could be resulted from vibrations of B-O-B superstructures and  $\text{P}(Q^2)\text{--O--P}(Q^2)$  chain-like structures [103-105], and the sharp peak at  $\sim 805\text{ cm}^{-1}$  corresponds to the breathing vibration of boroxol ring [106]. The two weak bands at  $660\text{ cm}^{-1}$  and  $710\text{ cm}^{-1}$  are composition independence, while the one at  $805\text{ cm}^{-1}$  becomes significantly intense with the addition of  $\text{B}_2\text{O}_3$ , implying that large amount of added boron are  $B^{III}$  species in boroxol rings. In the high frequency region ( $850\text{--}1350\text{ cm}^{-1}$ ), there are three distinct bands in the region of  $850\text{--}980$ ,  $1100\text{--}1250$ , and  $1270\text{--}1350\text{ cm}^{-1}$ , respectively. Vibrations of  $\text{P}(Q^n)$  and  $\text{Si}(Q^n)$  species give rise to the first two bands [103]. A remarkable shoulder exists at  $1080\text{ cm}^{-1}$  in the second band, which is a signature of the presence of  $\text{BPO}_4$  and  $\text{AlPO}_4$  structures [103]. The intensity of this shoulder increases as  $\text{SiO}_2$  is gradually substituted by  $\text{B}_2\text{O}_3$ , indicating the increase of boron has a positive effect on the formation of  $\text{P}(Q^4)$  species. The last band reflects the stretching vibration of  $\text{P=O}$  double bond [107]. As  $\text{B}_2\text{O}_3$  content increases, the intensity of this band decreases obviously, which is consistent with the changing trend of the shoulder at  $1080\text{ cm}^{-1}$ , i.e., more  $\text{P}(Q^4)$  species forms and less  $\text{P}(Q^3\text{--}Q^1)$  species exist by virtue of the partial replacement of  $\text{SiO}_2$  with  $\text{B}_2\text{O}_3$ .

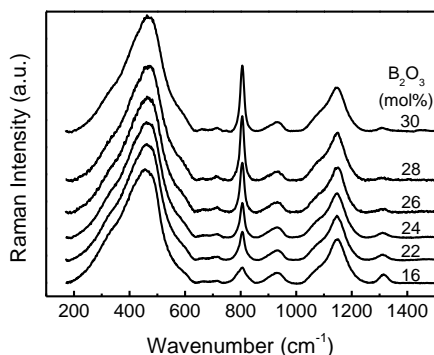


**Figure 2-5** Raman spectra of studied mixed network former glasses.

According to previous studies [91-99], for mixed network former glasses containing  $B_2O_3$ ,  $Al_2O_3$ , and  $P_2O_5$ , there is a competition between  $B^{IV}$  and  $Al^{IV}$  to be associated with  $P^4$  to form  $BPO_4$  and  $AlPO_4$  units, respectively. From NMR results, it is found that the content of  $AlPO_4$  units is approximately constant with the increase of  $B_2O_3$  content, indicating the formation of  $AlPO_4$  is favored over that of  $BPO_4$  in studied  $B_2O_3$ - $Al_2O_3$ - $SiO_2$ - $P_2O_5$  glasses. This implication is consistent with literature [91-96]. However, our structural characterizations (NMR and Raman) also show some unexpected implications. For studied glasses, we maintain a constant P:Al ratio ( $\sim 2.5$ ) larger than 1, and hence, it is expected that all Al should be in  $Al^{IV}$  sites regardless of the substitution of boron for silicon [91,92]. Moreover, the content of  $(Al_2O_3+B_2O_3)$  is much larger than  $P_2O_5$  content, and hence, all P should be in  $P(Q^4)$  species and form  $AlPO_4$  and  $BPO_4$  units [91,93,96]. Strikingly, as illustrated by  $^{27}Al$  MAS NMR results,  $Al^V$  and  $Al^{VI}$  species exist in all studied compositions, implying  $AlPO_4$  units cannot completely form. The presence of  $Al^V$  and  $Al^{VI}$  species accompanies the formation of other P species, e.g.,  $P(Q^2)$ , as illustrated by Raman spectra. As the  $B_2O_3$  content increases, the population of  $Al^V$  and  $Al^{VI}$  slightly decrease while that of  $BPO_4$  unit increases, leading to the increase of  $P(Q^4)$  content. This is consistent with the weakening of the Raman peak at  $1300\text{ cm}^{-1}$ . Therefore, we infer that, for  $B_2O_3$ - $Al_2O_3$ - $SiO_2$ - $P_2O_5$  glasses, there is always a tendency for P to form species other than  $P(Q^4)$  even the ratio of  $(Al_2O_3+B_2O_3)/P_2O_5$  is much larger than 1. However, this tendency becomes weaker as increasing the ratio of  $(Al_2O_3+B_2O_3)/P_2O_5$ .

Since the content of  $Al_2O_3$  is small ( $\sim 4\text{ mol\%}$ ) for all studied glasses, we use the ternary composition diagram of  $B_2O_3$ - $SiO_2$ - $P_2O_5$  (Fig. 2-6) obtained from [108] to explore the immiscible composition region and the possible phase separation. The phase separation becomes easier when the glass composition deviates from that in the glass formation region (region II in Fig. 2-6) towards  $B_2O_3$  apex [108]. Therefore, our studied glasses have possibility to exhibit phase separation. This is confirmed by our results of differential scanning calorimetry (DSC), i.e., the existence of two distinct glass transition regions, which will be discussed in Section 3.2. In contrast, Raman spectra performed on five different surface locations for each glass show no



significant difference, indicating the possible size of phase separation region should be less than 2  $\mu\text{m}$ , i.e., the resolution limit of Raman laser.

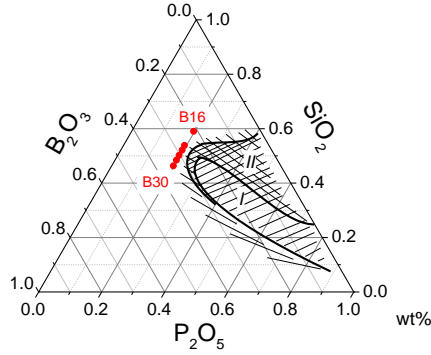


**Figure 2-6** Ternary composition diagram of  $\text{B}_2\text{O}_3$ - $\text{SiO}_2$ - $\text{P}_2\text{O}_5$  system. Regions I and II are the regions of glass-ceramic and glass formation, respectively.

To further explore the phase separation, we performed scanning electron microscopy (SEM) and energy-dispersive X-ray spectroscopy (EDS) on as-prepared and etched B28 glasses. Two acids (HCl and HF) with different concentration (5% and 10%) were used and etching duration varied from 30 s to 10 min. Both HCl and HF etching remove droplets (50-100 nm) from the glass matrix (Fig. 2-7). For HCl etching, the droplets are relatively separate from each other, while those are interconnected in the glass matrix for HF etching, which is similar to the early stage of spinodal phase separation [109]. Due to the light mass of boron, we exclude B and O elements, and calculate the atomic percentage (atom%) of Si, Al, and P for as-prepared and etched B28 glasses based on analyzed composition and EDS results (Table 2-3). After HCl etching, Al and P atom% of the glass significantly decrease, indicating that one glass phase dissolved in HCl is boron-rich and contains some P and Al. After HF etching, Si, Al, and P atom% keep unchanged, indicating two glass phases are simultaneously dissolved in HF. In addition, we performed Raman measurement on B28 glass etched by 10% HCl for 10 min (Fig. 2-8). After HCl etching, the bands at  $\sim 450$ ,  $950$ , and  $1300\text{ cm}^{-1}$  become intense, while the intensity of the peak at  $805\text{ cm}^{-1}$  significantly decreases. This implies that the dissolved glass by HCl is boron-rich and might contain some of  $\text{BPO}_4$  and  $\text{AlPO}_4$  units, which is in good agreement with EDS results. Therefore, the structure of the droplet shown in SEM images (Fig. 2-7) could be rich in boroxol rings and the matrix could consist of B-O-Si network.

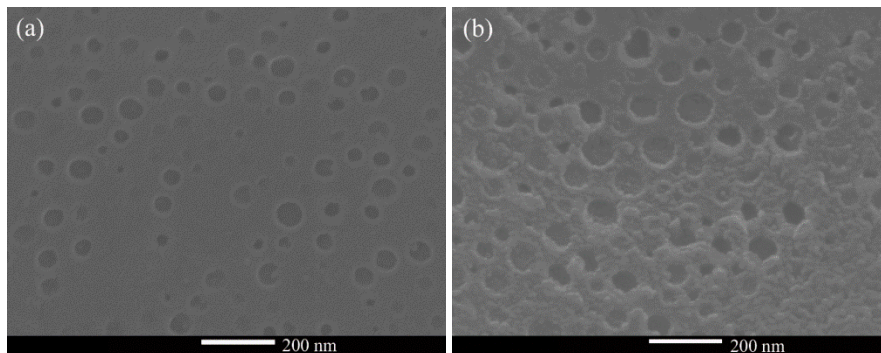


**Figure 2-7** SEM images of B28 glasses etched by (a) 10% HCl and (b) 10% HF for 10 min.

**Table 2-3** Si, Al, and P atom% of as-prepared and etched B28 glasses. B and O atom% are excluded from analyzed composition and EDS results.

Atom%	as-prepared	HCl etched	HF etched
Si	67.91	75.01	67.79
Al	8.95	6.36	8.66
P	23.14	18.63	23.54

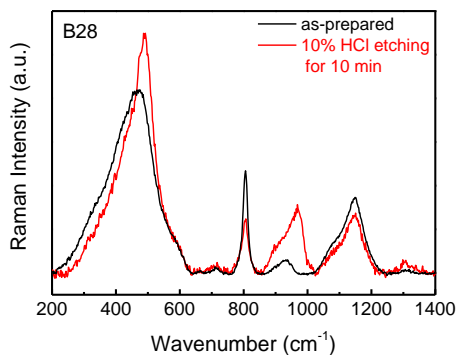


**Figure 2-8** Raman spectra of as-prepared B28 glass (black) and the one etched by 10% HCl for 10 min (red).

## 2.4. OXYFLUORIDE GERMANATE GLASSES

Oxyfluoride germanates have high glass-forming ability, excellent chemical and mechanical stabilities [110-114]. In addition, the heavy mass of germanium guarantees germanate glasses being good candidates of infrared windows operating in the 0.5-5  $\mu\text{m}$  region [115,116]. More importantly, since oxyfluoride germanate

glasses have low phonon energies, they are good candidates of photoluminescence materials if rare-earth ions are doped [45,47,110-113,117-120]. Hence, many studies focused on their luminescence properties and the environment of doped rare-earth ions [113], whereas the relation between structure and phase transition has not been well understood.

As mentioned in Section 2.1,  $\text{Ge}^{4+}$  can covalently bond with different number of oxygen (i.e., 4-, 5-, and 6-fold coordinated Ge species). The distribution of  $\text{Ge}^{\text{IV}}$ ,  $\text{Ge}^{\text{V}}$ , and  $\text{Ge}^{\text{VI}}$  depends on the content and type of network modifiers. When part of  $\text{O}^{2-}$  is substituted by  $\text{F}^-$ , properties of glasses and liquids significantly change, arising from their different degrees of polarization. Although their ionic radii are similar (126 pm for  $\text{O}^{2-}$  and 119 pm for  $\text{F}^-$ ), M-F bond (M: metallic cation) is more ionic than M-O bond, leading to the increase of the crystallization rate upon heating the glass well above  $T_g$  [111,119]. In this section, we explore the structure and crystallization of  $60\text{GeO}_2\text{-}25\text{BaF}_2\text{-}15\text{AlF}_3$  glass by using X-ray diffraction (XRD) and high-resolution transmission electron microscope (HR-TEM). The glass preparation is described in Paper 2. To obtain dynamically heated glasses, the as-prepared glass was heated to different temperatures ( $T_d$ ) above  $T_g$  in differential scanning calorimetry (DSC) at 20 K/min and cooled down to room temperature.  $T_d$  corresponds to either the onset or the peak temperatures of each crystallization peak shown in Fig. 2-9. The dynamically heated glasses are used to identify crystalline phases and explore the structural evolution with  $T_d$ .

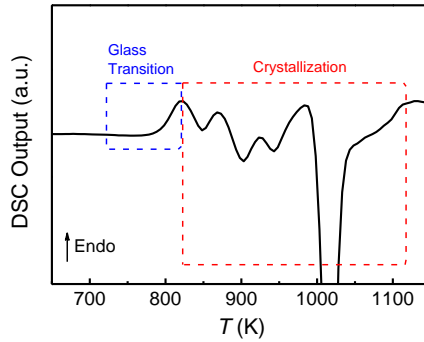


**Figure 2-9** The DSC first upscan curve of as-prepared glass  $60\text{GeO}_2\text{-}25\text{BaF}_2\text{-}15\text{AlF}_3$  at 20 K/min.

Fig. 2-10 shows XRD patterns of as-prepared glass and dynamically heated glasses. It is clearly seen that four crystalline phases progressively form.  $\text{BaGeO}_3$  (JCPDS: 73-1438) starts to form when  $T_d$  reaches 848 K. Further increase of  $T_d$  from 903 to 986 K leads to the formation of  $\text{BaF}_2$  (JCPDS: 85-1342) and  $\text{GeF}_4$  (JCPDS: 84-1559). As  $T_d$  reaches 1017 K, the main crystalline phase  $\text{BaAl}_2\text{Ge}_2\text{O}_8$  (JCPDS: 70-0562) forms. The XRD patterns of the glasses with  $T_d = 903, 925, \text{ and } 943$  K exhibit

same Bragg peaks but enhanced intensities as  $T_d$  increases, indicating  $\text{BaF}_2$  and  $\text{GeF}_4$  form simultaneously in the region of 903-943 K. This is consistent with the partial overlap of the two exothermic peaks at 903 K and 943 K in Fig. 2-9.

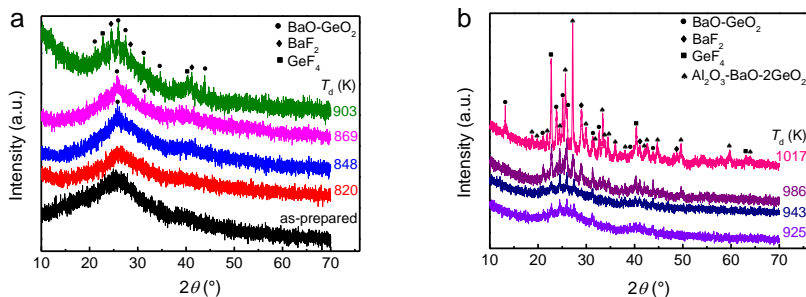


**Figure 2-10** XRD patterns of as-prepared glass and dynamically heated glasses.

Fig. 2-11 shows TEM images of three glasses, i.e., as-prepared glass, dynamically heated glasses with  $T_d=943$  and 1017 K. Strikingly, for the glass with  $T_d=943$  K, three regions are clearly observed: one crystalline phase, one amorphous matrix, and nano-clusters with a size of 5-20 nm. The coexistence of crystalline and amorphous phases is further confirmed by the selected area electron diffraction (SAED) pattern (inset of Fig. 2-11b). The occurrence of nano-clusters indicates the significant structural heterogeneity of the dynamically heated glass. In contrast, the nano-clusters vanish and the glass fully crystallizes when  $T_d$  further goes up to 1017 K (Fig. 2-11c), which corresponds to the temperature of the main crystallization peak in the DSC curve (Fig. 2-9).

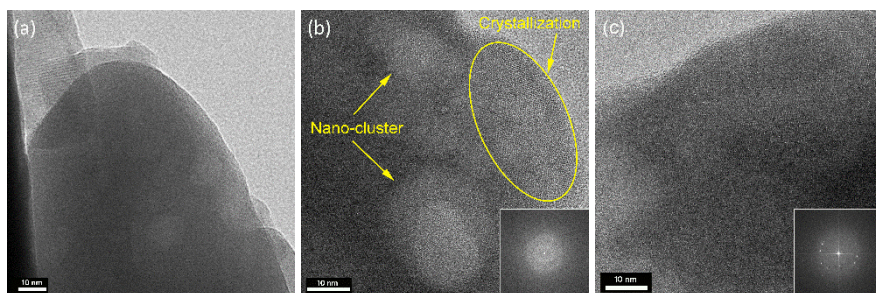


**Figure 2-11** High-resolution TEM images of (a) as-prepared glass, and dynamically heated glasses with (b)  $T_d=943$  K and (c)  $T_d=1017$  K. The insets show the selected area electron diffraction (SAED) patterns.

## 2.5. CALCIUM ALUMINATE GLASSES

Binary calcium aluminate glasses are of technical interest owing to their widespread applications in infrared windows, laser hosts, high-strength optical fibers, and photo-

memory materials [121-123]. However, due to the lack of typical network formers, binary calcium aluminates have poor glass forming ability compared to other typical oxide glass forming systems. Although some  $\text{CaO-Al}_2\text{O}_3$  glasses and liquids have been investigated [124-138], the intervention of fast crystallization upon cooling limits the temperature region of supercooled liquids and the composition region of glass formation. Laser-heated aerodynamic levitation furnaces (ALF) give us opportunities to overcome these difficulties. Due to the high cooling rate ( $10^2$ - $10^3$  K/s) [139] and containless technique, we prepared  $x\text{CaO}-(1-x)\text{Al}_2\text{O}_3$  glasses in a wide compositional region, i.e.,  $0.37 < x < 0.83$  (Table 2-4), which is much wider than that ( $0.6 < x < 0.7$ ) by using conventional melt-quenching method [140-144]. Furthermore, ALF can help us investigate structure, physical properties, and dynamics of the supercooled liquids. In this section, we first introduce ALF and then discuss structure and crystallization of  $\text{CaO-Al}_2\text{O}_3$  glasses and liquids.

**Table 2-4** Glass ID and composition of studied  $\text{CaO-Al}_2\text{O}_3$  glasses.

Glass ID	Chemical composition (mol%)	
	CaO	$\text{Al}_2\text{O}_3$
CA2	33.3	66.7
CA	50	50
C12A7	63.2	36.8
C3A	75	25
C5A	83.3	16.7

#### ***Aerodynamic Levitation Furnace (ALF)***

Fig. 2-12 shows an overview of the ALF. The  $\text{CaO-Al}_2\text{O}_3$  sample in the chamber (2) is fast heated to 3000 K by two  $\text{CO}_2$  laser beams (5) from the top and bottom, respectively. The inert gas enters the chamber together with the bottom  $\text{CO}_2$  laser to levitate the sample. The acoustic excitation system (3) provides a conventional sine wave to activate the levitated droplet to oscillate vertically. After switching off (3), the decay of the oscillation amplitude with time is monitored by the high speed camera (4) and hence the radius and the viscosity are determined. The temperature measurements are carried out using the single-color pyrometer (1). After switching off (5), the liquid droplet will be quenched to form glass sphere.

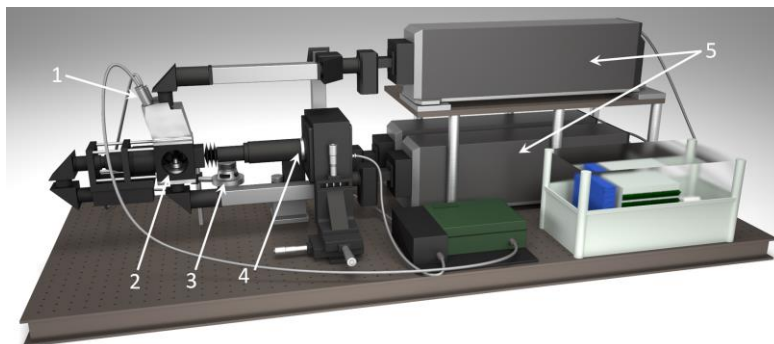


**Figure 2-12** Schematic of the aerodynamic levitation furnace. (1) pyrometer, (2) aerodynamic levitation chamber, (3) acoustic excitation system, (4) high-speed camera, and (5) top and bottom  $\text{CO}_2$  lasers.

### **Structure of $\text{CaO-Al}_2\text{O}_3$ liquids and glasses**

Fig. 2-13 shows pair distribution functions  $G(r)$  of  $\text{CaO-Al}_2\text{O}_3$  liquids derived from experimental neutron diffraction and molecular dynamic (MD) simulation. For the four compositions, there are three peaks at  $\sim 1.8$ ,  $\sim 2.4$ , and  $\sim 3$  Å, corresponding to Al-O, Ca-O, and O-O bond, respectively. The insensitivity of the peak positions of the first and third peaks with composition indicates  $\text{AlO}_4$  tetrahedra are little distorted by the addition of CaO. As the fraction of CaO mole content ( $C/(C+A)$  ratio) increases, Ca-O peak becomes obvious, indicating the formation of  $\text{CaO}_x$  polyhedra, i.e., less  $\text{Ca}^{2+}$  is used to charge compensating  $\text{AlO}_4$  tetrahedra. In addition, it is clearly seen that the simulation results are in good agreement with the experiments, confirming the reasonability of the liquid structure obtained from MD simulation. Fig. 2-14 shows abundant structural features of  $\text{CaO-Al}_2\text{O}_3$  liquids derived from MD simulations. As  $C/(C+A)$  ratio increases from CA2 to C3A,  $\text{Al}^{\text{IV}}$  species become dominant (from 74.79% to 93.04%), while the fraction of  $\text{Al}^{\text{V}}$  decreases to less than 10% in C3A.  $\text{Al}^{\text{VI}}$  species only exist in CA2 glass (1.59%). For O species, tricluster oxygen ( $\text{O}^3$ ) exists in the glasses from CA2 to C12A7. As increasing  $C/(C+A)$  ratio, the fraction of NBO and that of free oxygen ( $\text{O}^0$ ) increase, while that of BO exhibits a non-monotonic trend with a maximum at CA. The MD results confirm the existence of abundant structural species in  $\text{CaO-Al}_2\text{O}_3$  liquids such as  $\text{O}^3$ ,  $\text{O}^0$ , and  $\text{Al}^{\text{V,VI}}$  species.

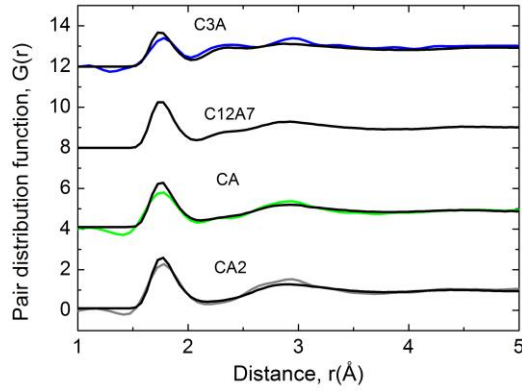


**Figure 2-13** Pair distribution function  $G(r)$  of studied  $\text{CaO-Al}_2\text{O}_3$  liquids. Black curves are derived from molecular dynamics simulations and colorful curves are derived from neutron scattering results.

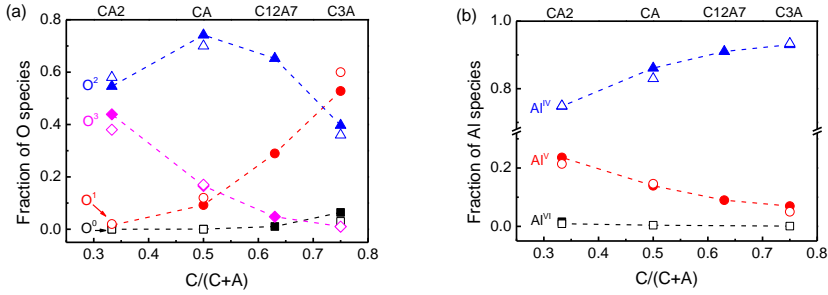


**Figure 2-14** Composition dependence of (a) O species and (b) Al species in  $\text{CaO-Al}_2\text{O}_3$  liquids.  $\text{O}^3$ ,  $\text{O}^2$ ,  $\text{O}^1$ , and  $\text{O}^0$  represent tricluster, BO, NBO, and free oxygen, respectively.  $\text{Al}^{\text{IV}}$ ,  $\text{Al}^{\text{V}}$ , and  $\text{Al}^{\text{VI}}$  represent four-, five-, and six-fold coordinated Al species, respectively. The filled data connected by dashed lines are MD simulation results and the hollow data are neutron diffraction results.

Fig. 2-15 shows the Raman spectra of studied  $\text{CaO-Al}_2\text{O}_3$  glasses in the range of 50-1100  $\text{cm}^{-1}$ . In the THz region of each spectrum, the peak at  $\sim 88 \text{ cm}^{-1}$  is the boson peak, and the peak at  $\sim 120 \text{ cm}^{-1}$  corresponds to the rattling motion of  $\text{Ca}^{2+}$  in its oxygen cage. In the high frequency region (400-1000  $\text{cm}^{-1}$ ), each spectrum consists of two broad bands in the region of 400-650  $\text{cm}^{-1}$  and 650-1000  $\text{cm}^{-1}$ , respectively. The former one is attributed by the vibration of BO in Al-O-Al linkage [145-147], and the latter one corresponds to the Al-O stretching vibrations in  $\text{Al}(\text{Q}^n)$ . As  $\text{C}/(\text{C}+\text{A})$  ratio increases, the peak position of the low-frequency band has no significant change, whereas that of the high-frequency one shifts non-monotonically, i.e., firstly to lower frequency and then to higher frequency. This indicates the average angle of BO keeps at  $\sim 120^\circ$  and C12A7 has the structure with most efficient atomic packing. Furthermore, as  $\text{C}/(\text{C}+\text{A})$  increases, the intensity of the low-

frequency band changes non-monotonically with a minimum at C12A7, indicating the degree of glass network connectivity initially decreases and increases further. This is consistent with the variation of  $T_g$  with composition as will be discussed in Section 3.4. In contrast, the high-frequency band becomes asymmetrically broad. According to previous studies [147-151], there is no consistent interpretation of the broadness, remaining ambiguous without a detailed theoretical vibrational analysis. We infer that the broadness might be associated with the distribution of different  $\text{Al}(Q^n)$  tetrahedra in the network.

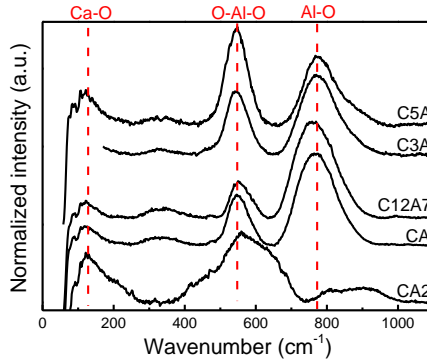


**Figure 2-15** Raman spectra of studied C-A glasses.

Fig. 2-16 shows the compositional dependence of calcium clusters containing different number of  $\text{CaO}_x$  polyhedra, which is derived from MD and RMC simulations of  $G(r)$  [140]. For  $\text{CaO-Al}_2\text{O}_3$  melts, isolated and small clusters aggregate to form medium clusters from CA2 to CA, and ultimately form large clusters when the CaO content reaches 75%. For glasses, the development of cluster aggregation starts at lower CaO content, indicating the accumulation of  $\text{CaO}_x$  polyhedra to form large clusters upon quenching the melts.

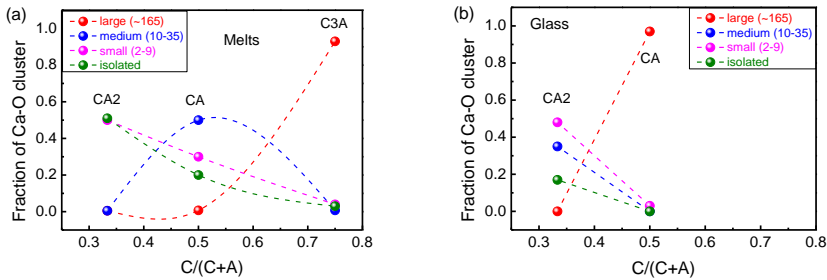


**Figure 2-16** Distribution of clusters containing  $\text{CaO}_x$  polyhedra with various sizes for  $\text{CaO-Al}_2\text{O}_3$  (a) melts and (b) glasses. Out of 172 units: Large ~165 units (red), Medium 10-35 units (blue), Small units 2-9 units (pink), Isolated units (olive).



Crystalline phases are examined by performing XRD on heat-treated  $\text{CaO-Al}_2\text{O}_3$  glasses (Fig. 2-17). The temperatures of heat treatments are crystallization peak temperatures determined by DSC measurements (see Section 3.4). Since there are two crystallization peaks in the DSC curve for C12A7 glass, two peak temperatures are used to obtain two heat-treated C12A7 samples, i.e., high temperature one (C12A7-HT) and low temperature one (C12A7-LT), respectively. It can be seen that  $\text{Ca}_{12}\text{Al}_{14}\text{O}_{33}$  and  $\text{Ca}_3\text{Al}_2\text{O}_6$  are main crystalline phases of heat-treated C12A7, C3A, C5A, and CA. For CA2, the main crystalline phase is of  $\text{CaAl}_4\text{O}_7$ . All the identifications of crystals in our heat-treated  $\text{CaO-Al}_2\text{O}_3$  samples are consistent with those in the binary phase diagram reported previously [152,153].

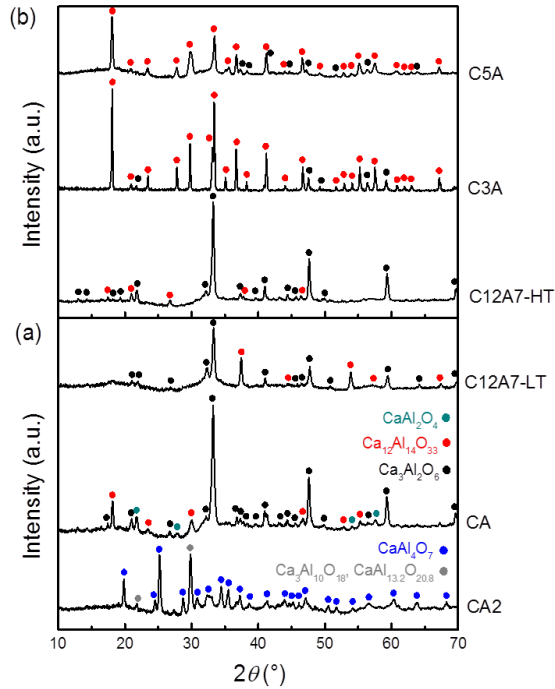


**Figure 2-17** XRD patterns of heat-treated  $\text{CaO-Al}_2\text{O}_3$  glasses. C12A7 glasses were heat-treated at two crystallization peak temperatures, corresponding to the high temperature heat-treated sample (C12A7-HT) and the low temperature heat-treated sample (C12A7-LT), respectively.

## CHAPTER 3. PHASE TRANSITIONS

Phase transitions involve many critical issues, e.g., glass transition, crystallization, and melting. The thermodynamics characterizing these phase transitions include enthalpic and entropic responses, and characteristic temperatures such as  $T_g$ ,  $T_c$  (crystallization peak temperature), and  $T_m$ . When equilibrium liquid is cooled below its melting point ( $T_m$ ), it will become supercooled, and its Gibbs free energy continues increase and surpasses that of its crystalline phase, leading to the thermodynamic favor of the formation of the crystal [154-157]. However, the supercooled liquid can bypass the crystallization and ultimately be frozen-in to form glasses if the cooling rate is high enough, because the viscous flow hinders efficient atomic arrangements. During the supercooling process, both atomic vibrations and the structural configurations continuously decreases, which are reflected by a loss of the vibrational and configurational entropy ( $S_{vib}$  and  $S_{conf}$ ), respectively, constituting the excess entropy of the supercooled liquid to the crystal. During the glass transition, most part of  $S_{vib}$  and  $S_{conf}$  vanishes. The fraction of  $S_{vib}$  in the excess entropy at  $T_g$  depends on the kinetic fragility of the liquid [158]. The liquid-to-glass transition can be seen as a partitioning process involving a break of ergodicity, avoiding the continuous decrease of the excess entropy of the liquid and circumventing the Kauzmann paradox [159]. In this chapter, we mainly investigate thermodynamics of glass transition, crystallization and phase separation.

### 3.1. BORATE-SILICATE GLASSES

To explore thermodynamics of glass transition, we performed DSC on the studied  $\text{Na}_2\text{O-CaO-B}_2\text{O}_3\text{-SiO}_2$  glasses as described in Paper I. The glass transition temperature ( $T_g$ ) is determined as the onset temperature of the glass transition in the isobaric heat capacity ( $C_p$ ) curve where its upscan rate and prior downscan rate are 10 K/min [6,8,160]. The  $C_p$  jump is the difference of the  $C_p$  between that of the glass and that of the liquid at  $T_g$ , i.e.,  $\Delta C_p$ .  $C_p$  consists of vibrational and configurational contributions, i.e.,  $C_{p,vib}$  and  $C_{p,conf}$ , respectively. The glassy state primarily contains vibrational degrees of freedom, i.e.,  $C_{pg} \approx C_{p,vib}$ , where  $C_{pg}$  is the glass  $C_p$  [43,161,162]. The liquid state contains both vibrational and configurational degrees of freedom, i.e.,  $C_{pl} = C_{p,vib} + C_{p,conf}$ , where  $C_{pl}$  is the liquid  $C_p$  [44,163]. For relatively strong glass forming liquid, i.e., liquid fragility index  $m$  is below 60,  $C_{p,vib}$  changes little through glass transition, i.e.,  $C_{p,vib}$  (glass) is nearly equal to  $C_{p,vib}$  (liquid) at  $T_g$ . Hence, the  $\Delta C_p$  primarily consists of  $C_{p,conf}$ , i.e.,  $C_{p,conf}(T_g) \approx C_{pl} - C_{pg} = \Delta C_p$ . This is the case for our studied glasses according to previous study [18].

As shown in Fig. 3-1,  $T_g$  exhibits a non-monotonic variation with a maximum at  $q=0.16$  as increasing  $\text{B}_2\text{O}_3$  content. Since  $T_g$  depends on the bonding strength and the network connectivity, the non-monotonic evolution of  $T_g$  with composition indicates

the polymerization of silicate network increases upon the initial addition of  $B_2O_3$  until  $q=0.16$ , and then decreases with further addition of  $B_2O_3$  until the formation of borate network. The formation of NBO and the structural transformation between  $BO_3$  and  $BO_4$  units significantly influence the connectivity of glass network. In addition,  $C_{p,conf}(T_g)$  increases rapidly with increasing  $q$  for both the silica- and borate-rich compositions, while keeps an approximately constant value in the compositional range  $0.32 < q < 0.84$ . The difference in  $C_{p,conf}(T_g)$  of silica-rich glass ( $q=0.08$ ) and borate glass ( $q=1.0$ ) is  $32 \text{ J mol}^{-1} \text{ K}^{-1}$ . In Fig. 3-2, we can see the  $N_4$  value (ratio of  $B^{IV}$  to total B) cannot fully explain the composition dependence of  $C_{p,conf}(T_g)$ . For borate glasses, the  $C_{p,conf}(T_g)$  is found to be mainly caused by the structural change in SRO, i.e., the enthalpy change ( $\Delta H$ ) of the conversion between  $B^{III}$  and  $B^{IV}$  determined by using Van't Hoff equation at different fictive temperatures [164,165]. However, this structural change can only give minor contribution (25%) to  $C_{p,conf}(T_g)$  for borate-silicate glasses (Fig. 3-3). Therefore, neither  $N_4$  nor the structural transformation from  $BO_3$  to  $BO_4$  give rise to the main change of  $C_{p,conf}(T_g)$  with composition in borate-silicate glasses. We infer IRO structural units could have effects on  $C_{p,conf}(T_g)$  [166,167], which will be discussed in Section 5.1.

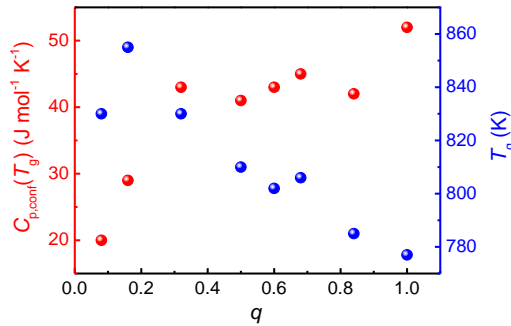


**Figure 3-1** The evolution of  $C_{p,conf}(T_g)$  (red) and  $T_g$  (blue) with composition for studied borate-silicate glasses.

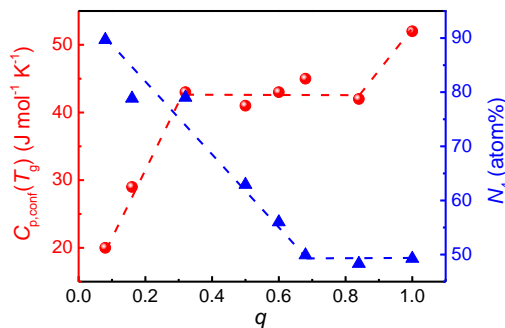


**Figure 3-2** The composition dependence of  $C_{p,conf}(T_g)$  (red sphere) and  $N_4$  value (blue triangle). The  $N_4$  value is calculated from our Raman data by using the method in Ref [69,168], and is consistent with  $N_4$  calculated from NMR results reported in Ref. [18].

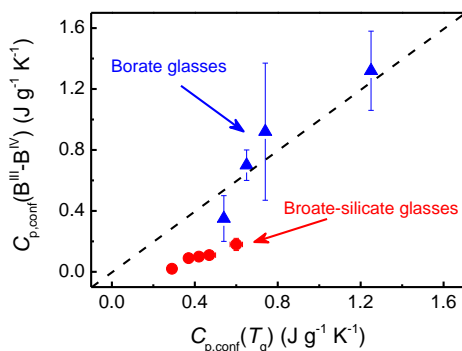


**Figure 3-3** Comparison of the  $C_{p,conf}$  change during structural transformation  $B^{III}$ -to- $B^{IV}$  with  $C_{p,conf}(T_g)$  for borate (blue triangle) and borate-silicate (red circle) glasses. The  $C_{p,conf}$  change of  $B^{III}$ -to- $B^{IV}$  is derived from the Van't Hoff equation. The data are taken from Refs [69,164,169-172].

### 3.2. MIXED NETWORK FORMER GLASSES

The DSC first upscan curves of  $x\text{B}_2\text{O}_3$ - $4\text{Al}_2\text{O}_3$ -( $86-x$ ) $\text{SiO}_2$ - $10\text{P}_2\text{O}_5$  glasses at 10 K/min show glass transition region and multi-crystallization region (Fig. 3-4a). As  $\text{B}_2\text{O}_3$  content increases, the first crystallization peak ( $P_1$ ) becomes more intense. When  $\text{B}_2\text{O}_3$  content reaches 26 mol%, a crystallization peak ( $P_2$ ) occurs and the last crystallization peak ( $P_4$ ) splits to two ( $P_3$  and  $P_4$ ). The two glass transition regions become evident with the increase of  $\text{B}_2\text{O}_3$  content (Fig. 3-4b), indicating the studied glasses are phase separated to two glass phases,  $G_1$  and  $G_2$ , characterized by  $T_{g1}$  and  $T_{g2}$ , respectively. The phase separation in  $x\text{B}_2\text{O}_3$ - $4\text{Al}_2\text{O}_3$ -( $86-x$ ) $\text{SiO}_2$ - $10\text{P}_2\text{O}_5$  glasses

is consistent with the immiscible composition region shown in ternary composition diagram of  $B_2O_3$ - $SiO_2$ - $P_2O_5$  if the small content of  $Al_2O_3$  (~4 mol%) is neglected (Fig. 2-6). Moreover, both the two  $T_g$ s decrease linearly with the addition of  $B_2O_3$ , and  $T_{g1}$  decreases faster than  $T_{g2}$  (Fig. 3-5a). Therefore, the substitution of  $B_2O_3$  for  $SiO_2$  plays a critical role in network connectivity of both  $G_1$  and  $G_2$ . On the other hand, the crystallization peak temperatures ( $T_p$ ) decrease with the addition of  $B_2O_3$  (Fig. 3-5b), reflecting the ease of crystallization. The occurrence of  $P_2$  (characterized by  $T_{p2}$ ) and the split of  $P_4$  (characterized by  $T_{p3}$  and  $T_{p4}$ ) imply that crystals formed in low- $B_2O_3$  glasses are thermodynamically unstable and transformed to other crystals when there is enough  $B_2O_3$  content (26 mol%).

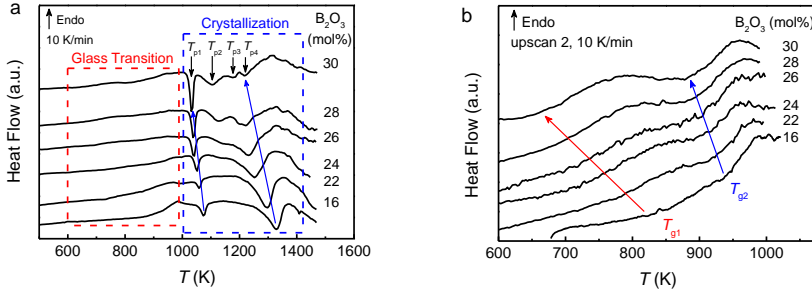


**Figure 3-4** (a) The first DSC upscan curves at 10 K/min for  $xB_2O_3$ - $4Al_2O_3$ -( $86-x$ ) $SiO_2$ - $10P_2O_5$  glasses. (b) The second DSC upscan curves at 10 K/min subsequent to a downscan with the same scanning rate. The two arrows show shifts of the two glass transition temperatures ( $T_{g1}$  and  $T_{g2}$ ) with increasing  $B_2O_3$  content.

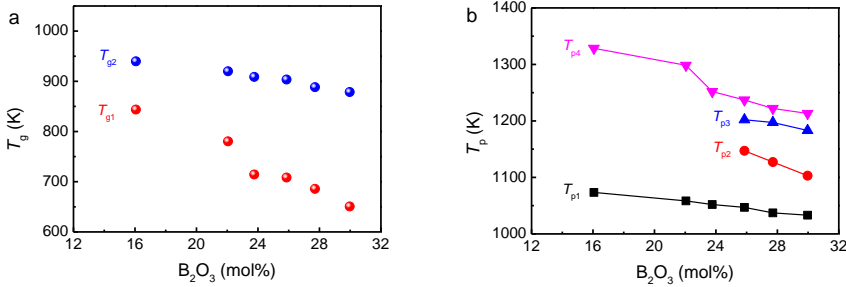


**Figure 3-5** Composition dependence of (a) Glass transition temperatures and (b) crystallization peak temperatures.

In addition, we have calculated three parameters to characterize the thermodynamics of the glass transition (Fig. 3-6).  $\Delta T_g$  and  $(dC_p/dT)_{\max}$  are the width and the steepness of the glass transition, respectively.  $\Delta C_p$  shows no clear trend with  $B_2O_3$  content for both  $G_1$  and  $G_2$ .  $(dC_p/dT)_{\max}$  of  $G_1$  keeps unchanged, while that of  $G_2$  continuously decreases with the increase of  $B_2O_3$  content.  $\Delta T_g$  of both  $G_1$  and  $G_2$  increase but with different changing rates as increasing  $B_2O_3$  content. For oxide glass forming systems,

$\Delta T_g$  and  $(dC_p/dT)_{\max}$  are inversely proportional in a series of glasses, which is the case for  $G_2$ , i.e., the narrow glass transition region is matched by its increased  $(dC_p/dT)_{\max}$ . However, for  $G_1$ , the glass transition region becomes significantly wider while  $(dC_p/dT)_{\max}$  remains unchanged with increasing  $B_2O_3$  content, leading to a large enthalpy change during the glass transition region. In addition, we have calculate  $\Delta T_c$ , i.e., the temperature range between the offset of glass transition and the onset of the first crystallization peak, reflecting glass stability against crystallization.  $\Delta T_c$  increases until  $B_2O_3$  content reaches 26 mol% and keeps almost unchanged with further increase of  $B_2O_3$  content. This indicates that substitution of  $B_2O_3$  for  $SiO_2$  in the studied glasses is helpful to stabilize glasses against crystallization, whereas it promotes liquid-liquid phase separation.

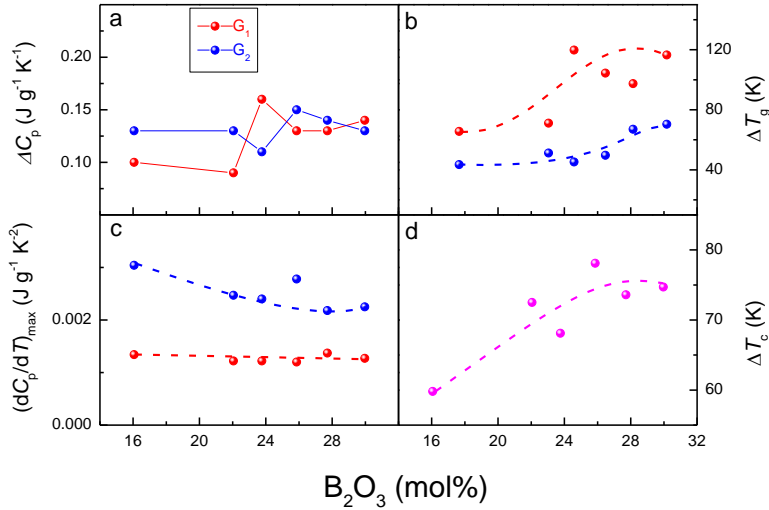


**Figure 3-6** Composition dependence of (a)  $\Delta C_p$ , (b) width of glass transition  $\Delta T_g$ , (c) slope at the inflection point of the sharp rise curve of  $C_p$  in the glass transition zone, i.e.,  $(dC_p/dT)_{\max}$ , (d) temperature range between the offset of glass transition and the onset of the first crystallization peak, i.e.,  $\Delta T_c$ . The properties of two glass phases  $G_1$  and  $G_2$  are shown as red and blue spheres, respectively.

To explore the phase separation, isothermal treatment and dynamic heating were performed on as-prepared B28 glass. The isothermal treatment and dynamic heating are defined in Paper II. The isothermal treatment temperature ( $T_h$ ) and duration ( $t_h$ ) are in the range of 694 ( $T_{g1}$ ) - 902 K ( $T_{g2}+10$  K) and 5-2880 min, respectively. Fig. 3-7 shows the first upscan  $C_p$  curves of B28 glasses heat-treated at varied  $T_h$  for 120 min. It can be seen that isothermal treatments influence both  $T_{g1}$  and  $T_{g2}$ . Moreover, as  $T_h$  increases to 892 K (i.e.,  $T_{g2}$  of as-prepared B28 glass), crystallization interrupts the second glass transition, i.e., low temperature (LT) crystallization. The occurrence

of *LT* crystallization indicates that isothermal treatments above  $T_{g2}$  induce the formation of ordered domains in the glass. Upon heating the glass containing these ordered domains, crystal growth leads to the *LT* crystallization peak.

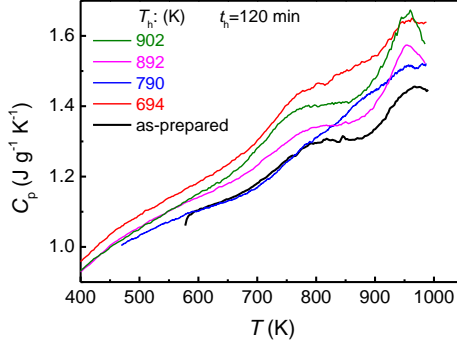


**Figure 3-7** The first upscan  $C_p$  curves of heat-treated B28 glasses with varied  $T_h$  for 120 min.

In contrast, Fig. 3-8 shows the first upscan  $C_p$  curves of B28 glasses heat-treated at (a) 790 K and (b) 892 K for varied durations. For  $T_h=790$  K, as  $t_h$  increases up to 120 min, the isothermal treatment has little influence on  $G_1$ , whereas  $G_2$  becomes unobservable. As  $t_h$  increases to 480 min, the glass transition region of  $G_2$  restores characterized by an enhanced  $\Delta C_p$ . Furthermore, the re-occurred glass transition of  $G_2$  exhibits an overshoot, which becomes intense as  $t_h$  increases till to 2880 min. For  $T_h=892$  K, the increase of  $t_h$  from 5 to 40 min causes slight change of  $T_{g1}$  and  $T_{g2}$ , but significant increase of  $\Delta C_p$  during the second glass transition region. Further increase of  $t_h$  from 80 to 480 min causes the *LT* crystallization. Therefore, ordered domains form during heat treatments if  $T_h$  enters the second glass transition region (892 K) and  $t_h$  is appropriate long (40 min). In contrast, the isothermal treatment with relative low  $T_h$  (790 K) induces significant overshoot of the second glass transition when the duration is long enough (480 min).

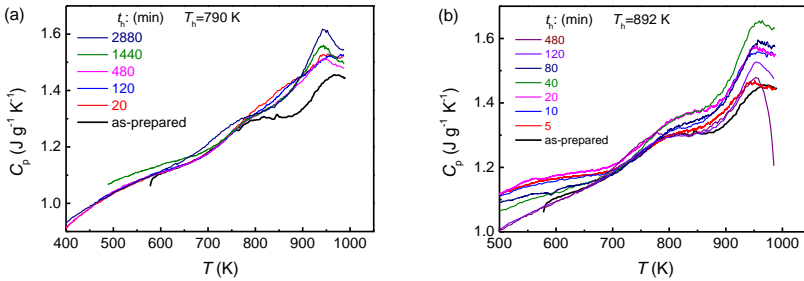


**Figure 3-8** The first upscan  $C_p$  curves of heat-treated B28 glasses with (a)  $T_h=790$  K, and (b)  $T_h=892$  K for varied  $t_h$ .

Fig. 3-9 shows multiple upscan  $C_p$  curves of four heat-treated B28 glasses. Remarkably, for the glass heat-treated at  $T_h < T_{g2}$  for 5 min,  $LT$  crystallization occurs after multiple DSC scans, indicating the dynamic heating (up to 993 K) can also induce the formation of ordered domains. Furthermore, an increase of the degree of the isothermal treatment (i.e., increase of  $t_h$  and/or  $T_h$ ) makes the  $LT$  crystallization easier during the subsequent dynamic heating. In addition, after multiple scans, the DSC upscan curves become overlapped with each other, e.g., scans 7-8 in Fig. 3-9(a) and (b), scan 5 in (c), and scan 3 in (d). This indicates that after the  $LT$  crystallization, the residual part of  $G_2$  is stable against crystallization during heating up to 993 K. Table 3-1 lists the numbers of DSC scans needed to induce and accompanish the  $LT$  crystallization, i.e.,  $N_{in}$  and  $N_{ac}$ , respectively. As  $T_h$  and/or  $t_h$  increases,  $N_{in}$  and  $N_{ac}$  decrease.

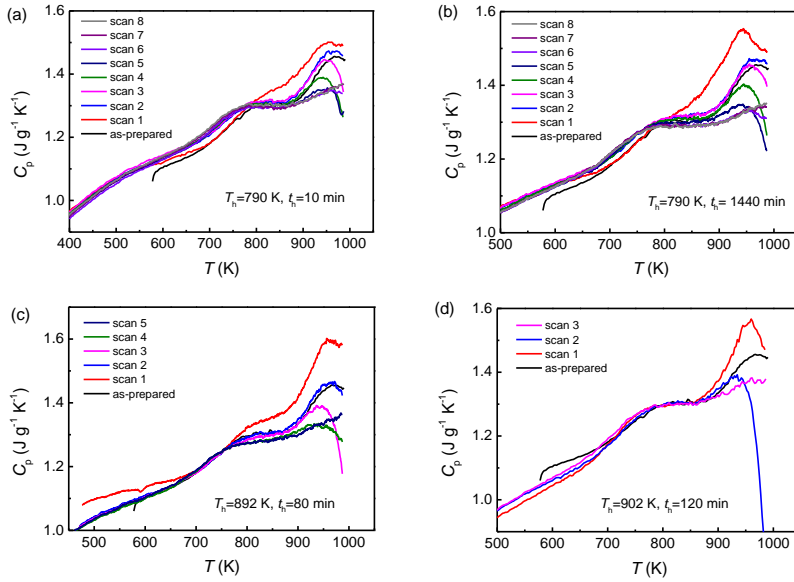


**Figure 3-9** Multiple upscan  $C_p$  curves of heat-treated B28 glasses with (a)  $T_h = 790$  K,  $t_h = 10$  min, (b)  $T_h = 790$  K,  $t_h = 1440$  min, (c)  $T_h = 892$  K,  $t_h = 80$  min, and (d)  $T_h = 902$  K,  $t_h = 120$  min.



**Table 3-1** The number of DSC scans needed to induce ( $N_{in}$ ) and accomplish ( $N_{ac}$ ) the LT crystallization for heat-treated B28 glasses.

Isothermal treatments		$N_{in}$	$N_{ac}$
$T_h$ (K)	$t_h$ (min)		
790	5-2880	3-6	7
	5-20	3-6	7
	40	2-5	6
892	80	1-4	5
	120	1-3	4
	240-480	1-2	3
902	120	1-2	3

To further explore the association between *LT* and high temperature crystallization features, we reheat the *LT* crystallized B28 glass, and compare its calorimetric response with that of the as-prepared glass (Fig. 3-10). It can be seen that the first crystallization peak at ~1050 K of the as-prepared glass is not observed for the *LT* crystallized B28 glass, indicating that crystals formed during the *LT* crystallization correspond to those formed at ~1050 K in the as-prepared B28 glass. Furthermore, the two separated crystallization peaks at ~1120 and 1210 K of the as-prepared glass merge to a broad one for the *LT* crystallized B28 glass. This indicates that the residual part of  $G_2$  interacts with  $G_1$  in the temperature range of 993-1330 K, i.e., they are micro-separated.

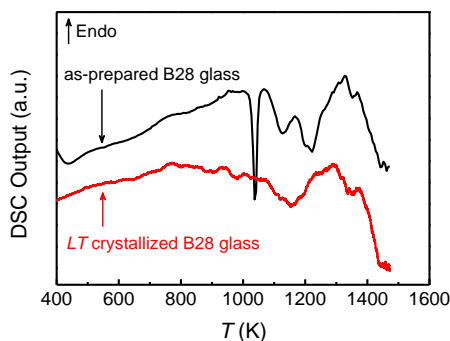


**Figure 3-10** The first DSC upscan curves up to 1473 K at 10 K/min for as-prepared B28 glass (black) and *LT*-crystallized B28 glass (red).

### 3.3. OXYFLUORIDE GERMANATE GLASSES

The first DSC upscan curve of as-prepared glass  $60\text{GeO}_2\text{-}25\text{BaF}_2\text{-}15\text{AlF}_3$  shows the glass transition (750-820 K) and crystallization (820-1050 K) (Fig. 2-9). As

described in Section 2.4, dynamically heated glasses are obtained to explore structural evolution with  $T_d$  (dynamic heating temperature) and crystallization. In Fig. 3-11a, the first three crystallization peaks become weaker and vanish with the increase of  $T_d$ . The glass network connectivity changes significantly during dynamic heating as illustrated by the evolution of  $T_g$  with  $T_d$  (Fig. 3-11b). The non-monotonic variation of  $T_g$  with  $T_d$  exhibits three stages. In stage 1 ( $T_d=820-903$  K),  $T_g$  continuously increases. In stage 2 ( $T_d=903-925$  K),  $T_g$  exceeds that of  $\text{GeO}_2$  glass and reaches a maximum. In stage 3 ( $T_d=925-986$  K),  $T_g$  decreases to approach that of  $\text{GeO}_2$  glass. The evolution of  $T_g$  with  $T_d$  in the two latter stages is similar to the composition dependence of  $T_g$  in germanate glasses [45-47,173], indicating a possible existence of germanate anomaly zone, which will be discussed in Section 5.3. In addition, since  $60\text{GeO}_2\text{-}25\text{BaF}_2\text{-}15\text{AlF}_3$  belongs to relative strong liquid ( $m \approx 60$ , see Section 4.3),  $C_{p,\text{conf}}(T_g) \approx C_{\text{pl}} - C_{\text{pg}} = \Delta C_p$ . As  $T_d$  increases,  $C_{p,\text{conf}}(T_g)$  exhibits a non-monotonic change with a maximum when  $T_d=848$  K (Fig. 3-12).

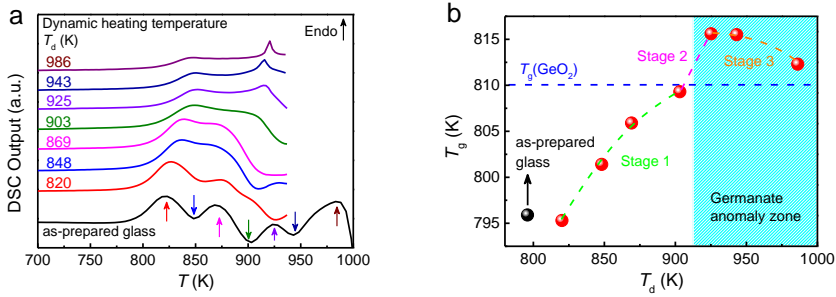


**Figure 3-11** (a) DSC first upscan curves of the glasses dynamically heated to different  $T_d$ . Arrows show the temperature positions of  $T_d$ . (b) The evolution of  $T_g$  with  $T_d$  exhibiting three stages illustrated by the dashed curves.  $T_g(\text{GeO}_2)$  is the glass transition temperature of the  $\text{GeO}_2$  glass. The blue region displays the possible germanate anomaly zone.

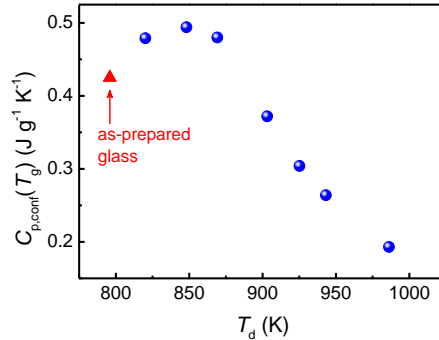


**Figure 3-12** The change of  $C_{p,\text{conf}}(T_g)$  with  $T_d$ .

In Fig. 3-11a, besides the change of glass transition and crystallization peak, a remarkable endotherm occurs at 925 K for the dynamically heated glasses with  $T_d$  in the range of 925-986 K. To the best of our knowledge, this endothermic response has not been discovered before in oxyfluoride germanate glasses. We perform DSC multiple DSC scans on these glasses to explore in-depth the features of this endotherm. In Fig. 3-13a, it can be seen that the endotherm in upscans corresponds to an exothermic peak in downscans, indicating the structural transition giving rise to these thermal responses is reversible in cycles of heating and cooling. Furthermore, these thermal responses are reproducible in the subsequent scans (Fig. 3-13b), implying that no further structural changes such as crystallization happen during the multiple scans. In addition, when the as-prepared glass is heated up to 1173 K, i.e., before melting, neither glass transition nor the endotherm appears in the subsequent scans (Fig. 3-13c). In contrast, when the as-prepared glass is heated up to 1473 K, i.e., above  $T_m$ , both the glass transition and the endotherm occur in the subsequent scans (Fig. 3-13d), implying that the endotherm could be caused by glass rather than crystals formed during heating. In addition, there are two ways to induce the endotherm: dynamic heating the as-prepared glass to the temperature region of 925-986 K or to the temperature above 1473 K.

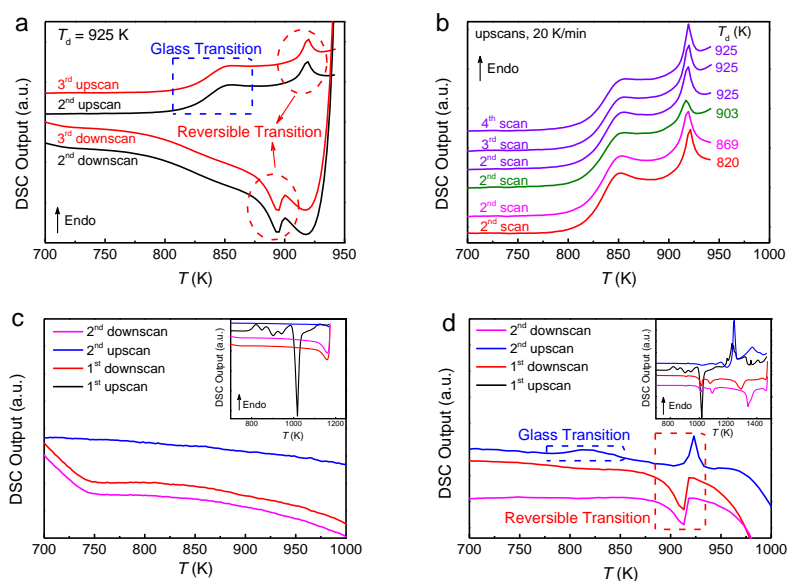


**Figure 3-13** (a) DSC curves of dynamically heated glass with  $T_d=925$  K. (b) Multiple DSC scans of dynamically heated glasses with  $T_d=820, 869, 903$ , and  $925$  K. The maximum temperature of DSC scans in (a) and (b) is  $943$  K. (c) and (d): DSC curves of as-prepared glass. The maximum temperatures of DSC scans in (c) and (d) are  $1173$  K and  $1473$  K, respectively. The main figures of (c) and (d) show DSC curves from  $700$  to  $1000$  K, and insets show those from  $700$  K to the maximum temperature.

### 3.4. CALCIUM ALUMINATE GLASSES

Fig. 3-14a displays the DSC first upscans of studied  $\text{CaO-Al}_2\text{O}_3$  glasses at 20 K/min. The presence of glass transition and subsequent crystallization for all  $\text{CaO-Al}_2\text{O}_3$  compositions confirms their amorphous nature. Fig. 3-14b shows the composition dependence of characteristic temperatures. The presence of minimum of  $T_m$  at C12A7 is because the thermal barrier of the first-order transition is lowest at the eutectic composition in the binary system. Strikingly, the variations of  $T_g$  and  $T_p$  with composition follow the similar trend as that of  $T_m$ , which is in strong contrast to that reported in literature [147,174-177]. We prepared  $\text{CaO-Al}_2\text{O}_3$  glasses by using sol-gel method and ALF to insure homogeneous dispersion of ions and to avoid heterogeneous crystallization during quenching. Furthermore, ALF significantly extends the composition region of glass forming, and hence our finding of  $T_g$  reveals a more universal trend compared to previous studies. In addition, it is found that  $T_g$  determined by DSC is not equal to the temperature where the viscosity is  $10^{12}$  Pa s for  $\text{CaO-Al}_2\text{O}_3$  glasses. Let  $\Delta T_g = T(\log \eta = 12) - T_g(\text{DSC})$ , we found that  $\Delta T_g$  is 91 K, 71 K, and -18 K for CA, C12A7, and C3A glasses, respectively. The values of  $T(\log \eta = 12)$  are obtained from Refs. [147,174-177]. This result implies that the frozen-in mechanism of structural rearrangement in of  $\text{CaO-Al}_2\text{O}_3$  liquids changes as the composition varies from  $\text{Al}_2\text{O}_3$ -rich to  $\text{CaO}$ -rich.

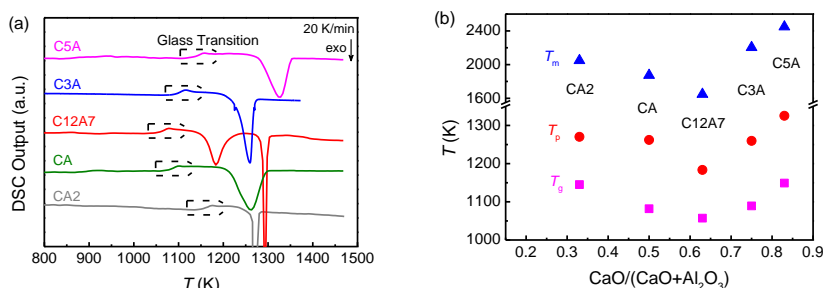


**Figure 3-14** (a) DSC first upscan of studied  $\text{CaO-Al}_2\text{O}_3$  glasses at 20K/min. (b) Composition dependence of glass transition temperature ( $T_g$ ), crystallization peak temperature ( $T_p$ ), and melting temperature ( $T_m$ ).  $T_m$  is obtained from the binary phase diagram of  $\text{CaO-Al}_2\text{O}_3$ .

As the  $\text{C}/(\text{C}+\text{A})$  ratio increases, the glass density ( $\rho_g$ ) shows a maximum at eutectic composition, i.e., C12A7, while the atomic density displays a monotonous decrease with an inflection point at C12A7 (Fig. 3-15). In  $\text{Al}_2\text{O}_3$ -rich composition from CA2 to C12A7, most  $\text{Ca}^{2+}$  cations play a role in charge-balancer of the  $\text{AlO}_4$  tetrahedra, which constitute the glass network. Therefore,  $\text{Ca}^{2+}$  cations occupy interstitial sites among  $\text{AlO}_4$  tetrahedra, leading to the decrease of free volume, and hence the increase of  $\rho_g$ . The decrease of the atomic density in this composition region is caused by the decrease of the atomic number per mole. In  $\text{CaO}$ -rich composition

from C12A7 to C5A, the gradual depolymerization of  $\text{AlO}_4$  network causes the decrease of both glass and atomic density.

Fig. 3-16a shows the liquid atomic density measured by using ALF. According to the temperature dependence of liquid density, we calculate the mean linear coefficient of thermal expansion (CTE) of  $\text{CaO-Al}_2\text{O}_3$  liquid in the temperature region of 1700-2800 K. Since the configurational entropy is frozen-in when the supercooled liquid is transformed to the glass, the CTE of solids is chiefly vibrational, and hence the CTE of the glass should be approximately equal to that of the crystal with the same composition. We collect the CTE data from Refs. [142,178-181] and combine them with our measured liquid CTE, as shown in Fig. 3-16b. The CTE of C12A7 liquid is exceptionally low. This indicates that it occupies the deep and least anharmonic interatomic potential, and hence its structure is most atomic packed.

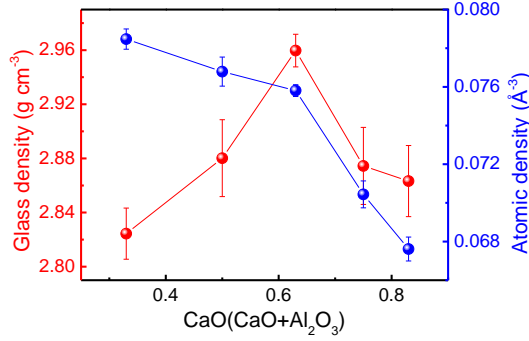


**Figure 3-15** Glass density and atomic density of studied  $\text{CaO-Al}_2\text{O}_3$  compositions.

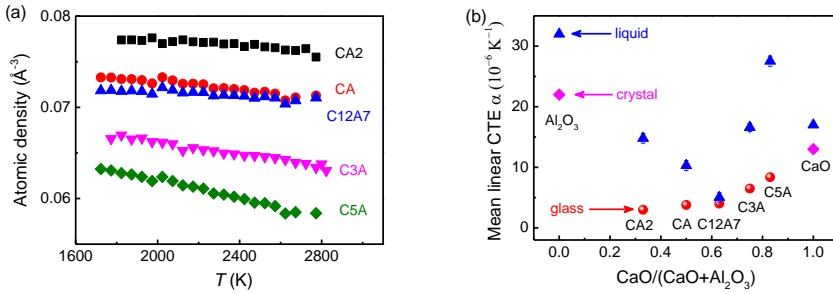


**Figure 3-16** (a) liquid atomic density of studied  $\text{CaO-Al}_2\text{O}_3$  compositions. (b) Coefficient of thermal expansion (CTE) of  $\text{CaO-Al}_2\text{O}_3$  glasses (red), liquids (blue), and crystals (pink). The CTEs of liquids are calculated by using liquid atomic density in (a), while those of glasses and crystals are collected from Refs. [142,178-181].

## CHAPTER 4. DYNAMICS

Understanding the temperature and composition dependence of liquid dynamics is critical for glass manufacturing and fiber spinning since this changing trend determines kinetic barriers of crystal nucleation and growth [32]. Furthermore, liquid dynamics is also central for exploring the origin of glass transition and the mechanism of relaxation. As mentioned before, although moderate structural changes are observed, the viscosity and relaxation time of the supercooled liquid rapidly rises by more than ten orders of magnitudes towards  $10^{12}$  Pa s upon cooling. The liquid fragility index  $m$  proposed by Angell is widely accepted to describe how far the temperature dependence of viscosity departs from the Arrhenius behavior [16,158], as given by

$$\left. \frac{\partial \log \eta}{\partial \frac{T_g}{T}} \right|_{T=T_g} = m \quad (4.1)$$

where  $\eta$  is the viscosity of the liquid and  $T_g$  is the glass transition temperature where its viscosity is  $10^{12}$  Pa s for most oxide glasses. The low/high value of  $m$  reflects the Arrhenius-like/non-Arrhenius dependence of  $\log \eta$  with  $T_g/T$  and hence the liquid is strong/fragile. For most liquids, the temperature dependence of  $\eta$  is non-Arrhenius, indicating the activation energy barrier of viscous flow is temperature dependent. In addition, it has been found recently that DSC method can be used to calculate liquid fragility  $m$  by virtue of the relation between fictive temperature ( $T_f$ ) and cooling rate ( $q_c$ ) [7,182]:

$$\frac{d \log(1/q_c)}{d(T_g/T_f)} = \frac{E_q(T_f)}{RT_g} = m \quad (4.2)$$

where  $E_q(T_f)$  is the activation energy of the structural relaxation and  $R$  is the ideal gas constant. The cooling rate  $q_c$  is given in K/s and the viscosity  $\eta$  is in Pa s. The fundamental finding to support DSC method is that the activation energy of structural relaxation is equal to that of viscous flow. The fictive temperature ( $T_f$ ) of a glass refers to the temperature at which the structure of an equilibrium liquid is frozen-in, and is proportional to  $q_c$  [160]. In this chapter, we investigate dynamics and/or liquid fragility in the four special oxide systems.

### 4.1. BORATE-SILICATE GLASSES

We performed DSC scans on one of studied borate-silicate glasses ( $15\text{Na}_2\text{O}-10\text{CaO}-51\text{B}_2\text{O}_3-24\text{SiO}_2$ ,  $q=0.68$ ) at different scanning rates (Fig. 4-1). By using Eq. 4.2, we calculated its liquid fragility index, i.e.,  $m=45 \pm 5$ , which is in consistent with previous studies [18]. Therefore, we use previous data to analysis the evolution of  $m$

with composition (Fig. 4-2a). It can be seen that initial addition of  $B_2O_3$  causes rapid increase of  $m$  from  $q=0.08$  to 0.32, while further addition of  $B_2O_3$  leads to a slow increase of  $m$  from  $q=0.32$  to 1.0, indicating the viscosity increases faster upon cooling to  $T_g$  for the liquid containing more  $B_2O_3$ . Furthermore, the rapid increase of  $m$  in  $SiO_2$ -rich compositions ( $0.08 < q < 0.32$ ) reflects that the evolution of viscosity with temperature is sensitive to the added  $B_2O_3$  in this composition region. According to structural results, most boron is  $B^{IV}$  and bonds with Si to form danburite-like rings in this composition region. Therefore, we infer that the danburite-like rings are easy to break down to decrease the viscosity upon heating above  $T_g$ , because they are not energetic favorable compared to other borate rings. Further moderate increase of  $m$  in  $B_2O_3$ -rich compositions ( $0.32 < q < 1.0$ ) is a result of the existence of large amount of borate structural units with large freedom and the lack of rigid silicate structure network. In addition,  $C_{p,conf}(T_g)$  has similar composition dependence as  $m$ , implying a closely association between them (Fig. 4-2b). The structural origin of  $C_{p,conf}(T_g)$  will be discussed in detail in Section 5.1.

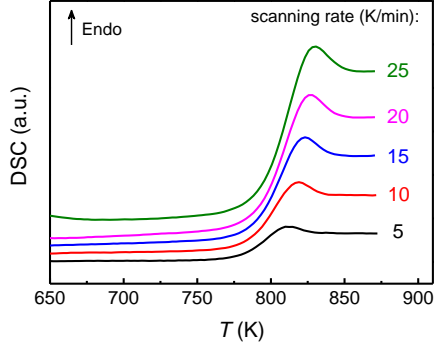


**Figure 4-1** DSC upscan curves of  $15Na_2O-10CaO-51B_2O_3-24SiO_2$  glass ( $q=0.68$ ) at different scanning rates (5-25 K/min). For each upscan curve, its heating rate is equal to the cooling rate of its prior downscan curve.

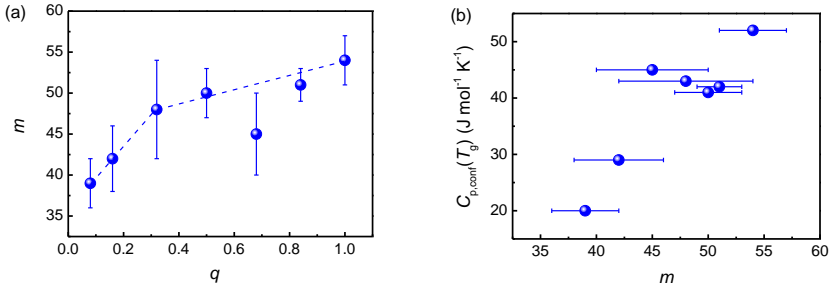


**Figure 4-2** (a) Composition dependence of liquid fragility  $m$ .  $q$  represents the mole ratio of  $[B_2O_3]/[B_2O_3] + [SiO_2]$ . (b) Relation between  $C_{p,conf}(T_g)$  and liquid fragility index  $m$  of studied borate-silicate glasses.

## 4.2. MIXED NETWORK FORMER GLASSES

Fig. 4-3a shows the DSC upscans of B28 glass ( $28\text{B}_2\text{O}_3\text{-}4\text{Al}_2\text{O}_3\text{-}58\text{SiO}_2\text{-}10\text{P}_2\text{O}_5$ ) at different scanning rates (5 and 10 K/min). The low scanning rate significantly promotes the crystallization. This indicates the time needed for crystal growth is short and some ordered domains can form in the second glass transition region of 850-950 K. In addition, we try to use DSC method to determine the liquid fragility index  $m$  for studied glasses. However, the large shift of fictive temperature ( $T_f$ ) with the changing of scanning rate leads to extremely small value of  $m$ , e.g.,  $m$  is even below 10 for B16, B28, and B30 (Fig. 4-3b). Therefore, it is inadequate to obtain  $m$  by DSC method for studied glasses. Nevertheless, the high sensitivity of  $T_f$  to the scanning rate implies the some domains of the glass structure relax much faster, i.e., the presence of structural heterogeneity.

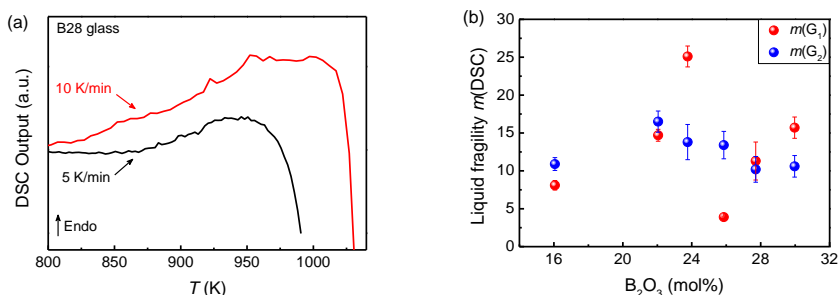


**Figure 4-3** (a) DSC curves of B28 glass at 5 K/min (black) and 10 K/min (red). (b) Liquid fragility index  $m$  calculated by using DSC method.

We also measured the viscosity of B28 glass near 780 K (Fig. 4-4) by using a ball penetration viscometer (BÄHR, VIS405) [183]. It can be seen that  $m$  determined by using Eq. 4.1 is similar to the one calculated by using Eq. 4.2. In addition, we found that the temperature where the viscosity is  $10^{12}$  Pa s locates between  $T_{g1}$  and  $T_{g2}$  for B28 glass. The viscosity results indicate the extremely strong nature of the studied mixed network former glass forming liquids. However, since the viscosity measured is the equilibrium viscosity, the viscosity data obtained near  $10^{12}$  Pa s could be influenced by the formation of ordered domains during the measurement in the temperature region near the second glass transition, and hence there is a potential for crystal nucleation and growth.



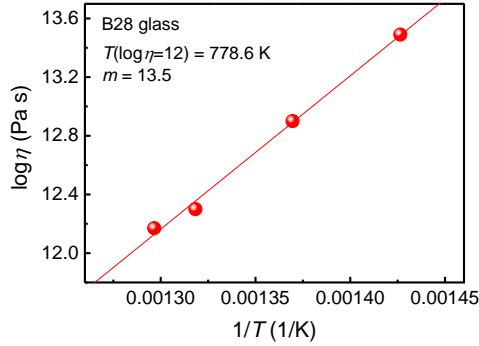


**Figure 4-4** Viscosity near  $10^{12}$  Pa s for B28 glass.

### 4.3. OXYFLUORIDE GERMANATE GLASSES

Fig. 4-5 shows DSC upscan curves with different scanning rate for all studied glasses, and the liquid fragility index  $m$  is calculated by using Eq. 4.2 (Fig. 4-6a). Compare to the as-prepared glass,  $m$  increases for the dynamically heated glass with  $T_d=848$  K. As  $T_d$  increases from 848 to 986 K,  $m$  continuously decreases and approaches that of  $\text{GeO}_2$  ( $m \approx 15$ ). The initial increase of  $m$  could be caused by the completion of modifiers, and the later decrease of  $m$  could be associated with the interaction between different  $\text{GeO}_x$  polyhedra and  $\text{GeO}_4$  rings. In addition, as similar to borate-silicate glasses,  $C_{p,\text{conf}}(T_g)$  is closely associated with  $m$  for oxyfluoride germanate glass forming liquids (Fig. 4-6b), although the value of  $m$  for dynamically heated glasses is much higher than that of borate-silicate glasses.

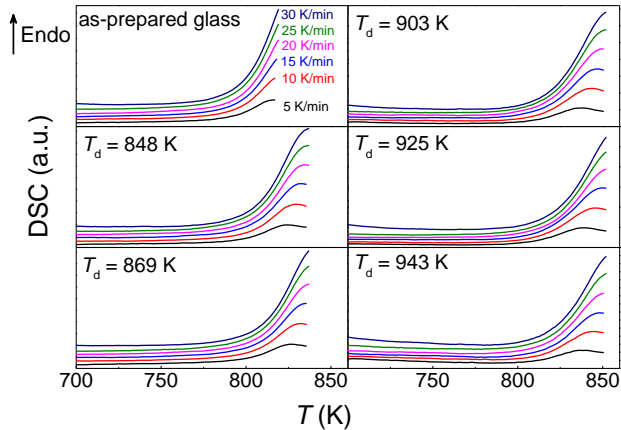


**Figure 4-5** DSC upscan curves at different scanning rates (5-30 K/min) for the glasses dynamically heated to various  $T_d$ . The heating rate is equal to the cooling rate of the prior downscan curve.

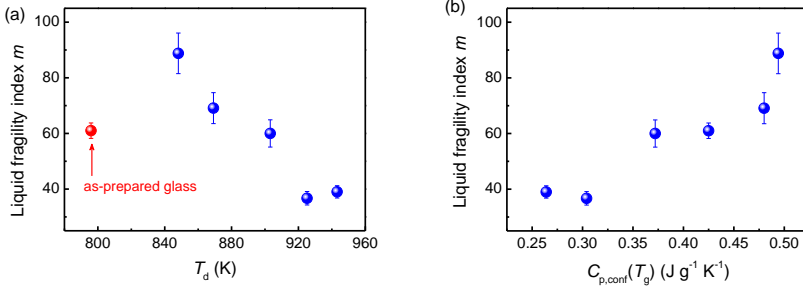


**Figure 4-6** (a) Evolution of liquid fragility index  $m$  with heat treatment temperature  $T_d$ . (b) Relation between  $m$  and configurational heat capacity at  $T_g$  in oxyfluoride germanate system.

#### 4.4. CALCIUM ALUMINATE GLASSES

According to literature,  $x\text{CaO}-(1-x)\text{Al}_2\text{O}_3$  liquid belongs to relative fragile type, and it becomes more fragile as the content of CaO decreases in the range of  $0.5 < x < 0.75$  [121]. However, the previous studied composition and temperature regions are limited due to the ease of crystallization. Although the structure of some  $\text{CaO}-\text{Al}_2\text{O}_3$  liquids have been investigated [140,141], the dynamics have not been fully studied. In this section, we measured viscosity of equilibrium and supercooled  $\text{CaO}-\text{Al}_2\text{O}_3$  liquids in high temperature region (1500–2800 K) by using ALF. The relation between  $\eta$  and the damping constant of the oscillation  $\Gamma$  is given by [141]:

$$\eta = \frac{1}{(l-1)(2l+1)} \frac{3M\Gamma}{4\pi a} \quad (4.3)$$

where  $M$  is the droplet mass,  $a$  is its radius, and  $l$  is the number of the mode. Typically,  $l$  equals 2 for not too large excitation amplitudes. To determine  $\Gamma$ , the droplet was acoustically excited for a short time close to the primary resonance frequency. After removing the excitation, the decayed oscillation amplitude was monitored, which consists of the harmonic and damped parts [142]. The harmonic oscillator motion for the steady state is given by:

$$r_{h/v}(t) = A \cdot \sin[2\pi\nu_{h0}(t - t_0)] + r_0 \quad (4.4)$$

where  $r_{h/v}(t)$  is the ratio of horizontal to vertical radius,  $A$  is the amplitude,  $\nu_{h0}$  is the excitation frequency,  $t_0$  is an offset, and  $r_0$  is the mean radius of the droplet. For the damped decay:

$$r_{h/v}(t) = A \cdot \exp[-\Gamma(t - t_1)] \cdot \sin[2\pi\nu_{dh0}(t - t_0)] + R_{av} \quad (4.5)$$

where  $t_1$  is the starting time,  $\nu_{\text{dho}}$  is the resonance frequency of the droplet,  $R_{\text{av}}$  is the radius of the droplet in rest. Therefore, the damping constant  $\Gamma$  can be determined by Eq. 4.5 and hence  $\eta$  is obtained by Eq. 4.3.

Fig. 4-7 shows the viscosity of studied CaO-Al<sub>2</sub>O<sub>3</sub> liquids. As the C/(C+A) ratio increases, the viscosity at  $T_m$ ,  $\eta(T_m)$ , initially increases from CA2 to C12A7 and then decreases from C12A7 to C5A, implying that the mechanism of viscous flow in Al<sub>2</sub>O<sub>3</sub>-rich compositions is different with that in CaO-rich compositions. Furthermore, the low values of  $\eta(T_m)$  for all CaO-Al<sub>2</sub>O<sub>3</sub> liquids indicate that the kinetic barriers of nucleation and crystal growth are small, and hence the liquids are difficult to bypass crystallization to form glasses compared to most of oxide liquids, i.e., poor glass forming ability of CaO-Al<sub>2</sub>O<sub>3</sub> liquids. In addition, the viscosity increases rapidly through  $T_m$  upon cooling. The non-Arrhenius rapid increase of viscosity indicates that the activation energy of viscous flow increases. Normally, the rapid increase of viscosity in high temperature range near  $T_m$  is closely associated with the decrease of ion exchange (mainly for oxygen) and rearrangement of structural units [131,132].

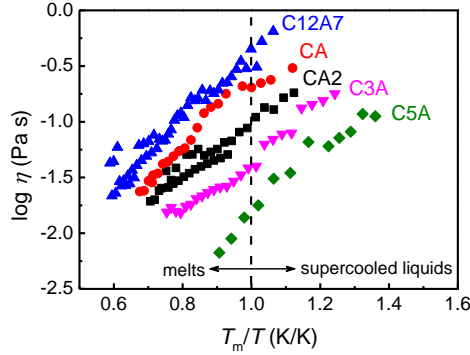


**Figure 4-7**  $T_m$  scaled viscosity of studied CaO-Al<sub>2</sub>O<sub>3</sub> liquids in the temperature region of 1500-2800 K.

Due to the size limit of glass spheres prepared by ALF, the viscosity of CaO-Al<sub>2</sub>O<sub>3</sub> near  $T_g$  cannot be measured by ball penetration viscometer as described in Section 4.2 for mixed network former glass. Therefore, we prepared C3A bulk glass to measure its viscosity near  $T_g$ , and then used DSC method to obtain the viscosity near  $T_g$  for other compositions. The relation between viscosity ( $\eta$ ), fictive temperature ( $T_f$ ), and cooling rate ( $q_c$ ) is given by [184]:

$$\log \eta(T) = \log K_c - \log q_c(T_f) \quad (4.6)$$

where  $K_c$  is the shift factor. Eq. 4.6 is applied in this case when  $T=T_f$ . For the silicate glasses,  $\log K_c=11.35$  [184]. For CaO-Al<sub>2</sub>O<sub>3</sub> glasses, we modified the

parameter  $\log K_c=11$  based on the viscosity of C3A bulk glass and  $q_c(T_f)$  of C3A glass sphere as illustrated by Fig. 4-8. Therefore, the viscosity near  $T_g$  of other CaO- $\text{Al}_2\text{O}_3$  glasses are obtained based on Eq. 4.6.

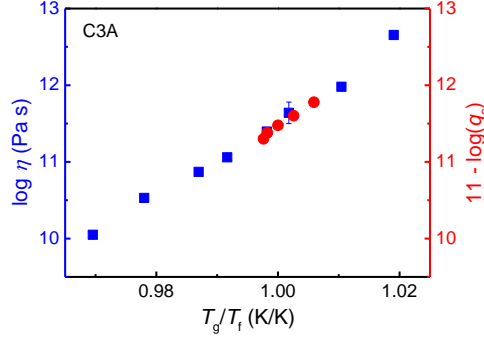


**Figure 4-8** Relation between viscosity, fictive temperature, and cooling rate for C3A. The viscosity data are obtained by ball penetration viscometer.

Fig. 4-9 shows the viscosity of three studied CaO- $\text{Al}_2\text{O}_3$  liquids in two temperature regions, i.e., around  $T_m$  and near  $T_g$ , respectively. Here we use Mauro-Yue-Ellison-Gupta-Allan (MYEGA) model to fit the viscosity data, which is given by [185]:

$$\log \eta(T) = \log \eta_0 + (\log \eta(T_g) - \log \eta_0) \frac{T_g}{T} \exp\left[\left(\frac{m}{\log \eta(T_g) - \log \eta_0} - 1\right)\left(\frac{T_g}{T} - 1\right)\right] \quad (4.7)$$

where  $\eta_0$  is the high temperature limit of viscosity. We applied MYEGA to fit the viscosity data in two temperature regions, respectively. Strikingly, the dynamics behave differently in the two temperature regions (see the fitted lines in Fig. 4-9), i.e., the derived  $m$  is different. Let the  $m$  obtained from the viscosity data near  $T_g$  is written as  $m_1$ , and that around  $T_m$  is written as  $m_2$ , then  $m_1 < m_2$ . According to previous studies [186,187], this mismatch of dynamics in different temperature regions implies that a fragile-to-strong ( $f$ - $s$ ) transition takes place in the liquid upon cooling from  $T_m$  to  $T_g$ .

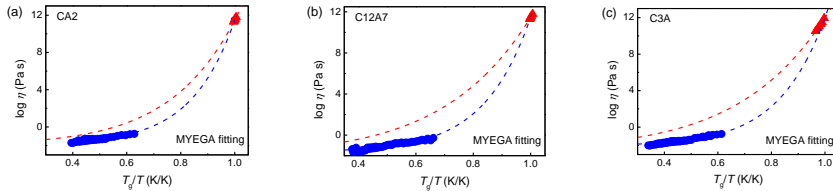


**Figure 4-9** Viscosity of three studied CaO- $\text{Al}_2\text{O}_3$  liquids (a) CA2, (b) C12A7, and (c) C3A in the temperature region near  $T_g$  and around  $T_m$ . Dashed lines refer to MYEGA fittings.

To simultaneously fit viscosity data in the two temperature regions, we use the generalized MYEGA equation which is given by [186]:

$$\log \eta = \log \eta_0 + \frac{1}{T[W_1 \exp(-\frac{C_1}{T}) + W_2 \exp(-\frac{C_2}{T})]} \quad (4.8)$$

where  $\eta_0$  has the same meaning as in Eq. 4.7.  $C_1$  and  $C_2$  qualitatively represent the two different structural mechanisms controlling the dynamics in fragile and strong regimes, respectively. Based on Adam-Gibbs equation and temperature-dependent constraints theory [185-190],  $C_1$  and  $C_2$  correspond to the two constraint onsets of different structural mechanisms resulting in floppy-to-rigid transitions.  $W_1$  and  $W_2$  are normalized weighting factors, corresponding to the contributions of fragile and strong part to the whole CaO-Al<sub>2</sub>O<sub>3</sub> system. As illustrated in Fig. 4-10, the viscosity of the studied CaO-Al<sub>2</sub>O<sub>3</sub> liquids can be captured by using the generalized MYEGA equation, i.e., the dynamics are reconciled in the temperature region from equilibrium liquids to deep supercooled liquids for CaO-Al<sub>2</sub>O<sub>3</sub> system. The temperature and viscosity of the  $f$ - $s$  transition point are given by [187]:

$$T_{f-s} = \frac{C_1 - C_2}{\ln W_1 - \ln W_2} \quad (4.9)$$

and

$$\log \eta_{f-s} = \log \eta_0 + \frac{1}{2} \frac{\ln(W_1/W_2)}{C_1 - C_2} \cdot \frac{W_2 [-C_1/(C_1 - C_2)]}{W_1 [-C_2/(C_1 - C_2)]} \quad (4.10)$$

The  $f$ - $s$  transition point is the temperature at which the fragile and strong phases have the same contribution to the whole liquid dynamics. For CaO-Al<sub>2</sub>O<sub>3</sub> liquids, the  $f$ - $s$  transition occurs at  $\sim 1.15T_g$ , corresponding to a viscosity of about  $10^5$  Pa s, which is hidden by crystallization upon normal cooling. Physically, the fragile/strong phase is characterized by high/low activation enthalpy and high/low transition point entropy. The relation  $C_1 > C_2$  is indicative of a higher activation enthalpy for the dynamics in the fragile phase. However, at high temperature this is more than compensated by the relation  $W_1 > W_2$ , indicating a much greater number of transition paths (i.e., transition point entropy) for the fragile phase. In the potential energy landscape, the fragile/strong phase would sample phase space with deeper/shallower inherent structures (ISs) and a much greater/fewer number of basins [191]. The competition between entropy and enthalpy is essential for the existence of  $f$ - $s$  transition [186].

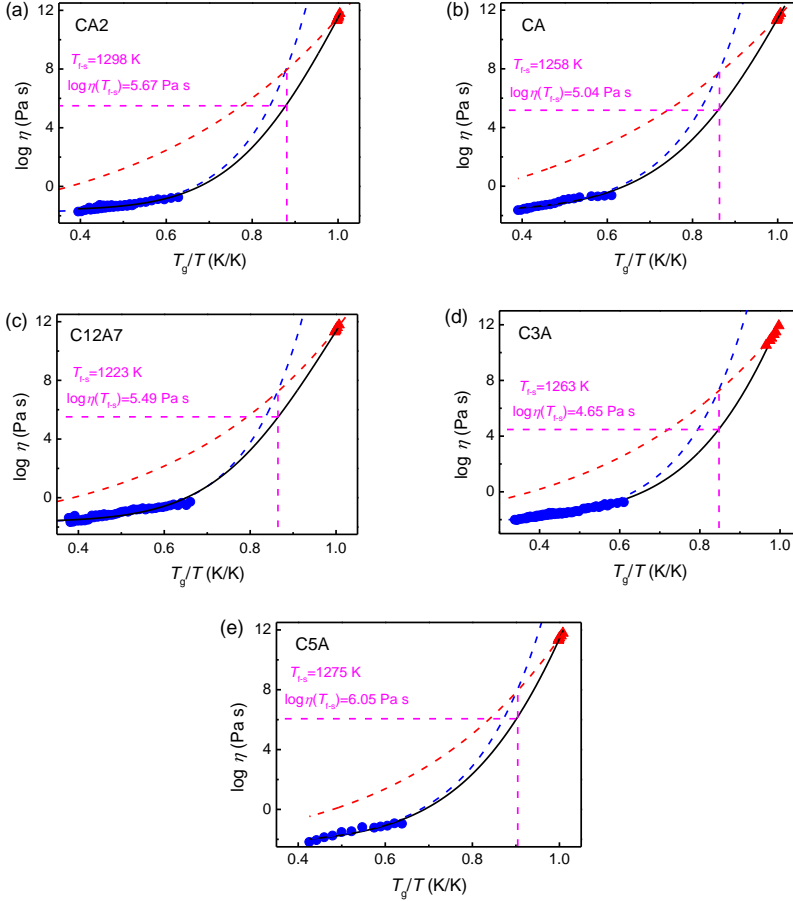


**Figure 4-10** Viscosity as a function of the  $T_g$  scaled temperature  $T$ . Black lines: fits of Eq. 4.8 to the viscosity for (a) CA2, (b) CA, (c) C12A7, (d) C3A, and (e) C5A. Blue and red dashed lines: a fragile term dominant at high temperatures and a strong term dominant at low temperatures, respectively. The two terms give contribution to the overall viscous behavior. Pink dashed lines: the temperature and viscosity where the  $f$ - $s$  transition occurs.

Since the MYEGA model is based on Adam-Gibbs (AG) model concerning configurational entropy  $S_c(T)$  [185], we use AG model to fit viscosity data of the fragile and strong phases, respectively, and hence, the excess entropy as a function of  $T$  is obtained (Fig. 4-11). Remarkable, a complementary reduction in excess entropy at  $T_{f-s}$  ( $\Delta S_{f-s}$ ) circumvent the Kauzmann paradox [159]. Furthermore, a step-wise reduction at  $T_{f-s}$  in atomic volume ( $\Delta V_{f-s}$ ) also occurs (Fig. 4-12), substantiating the  $f$ - $s$  transition.

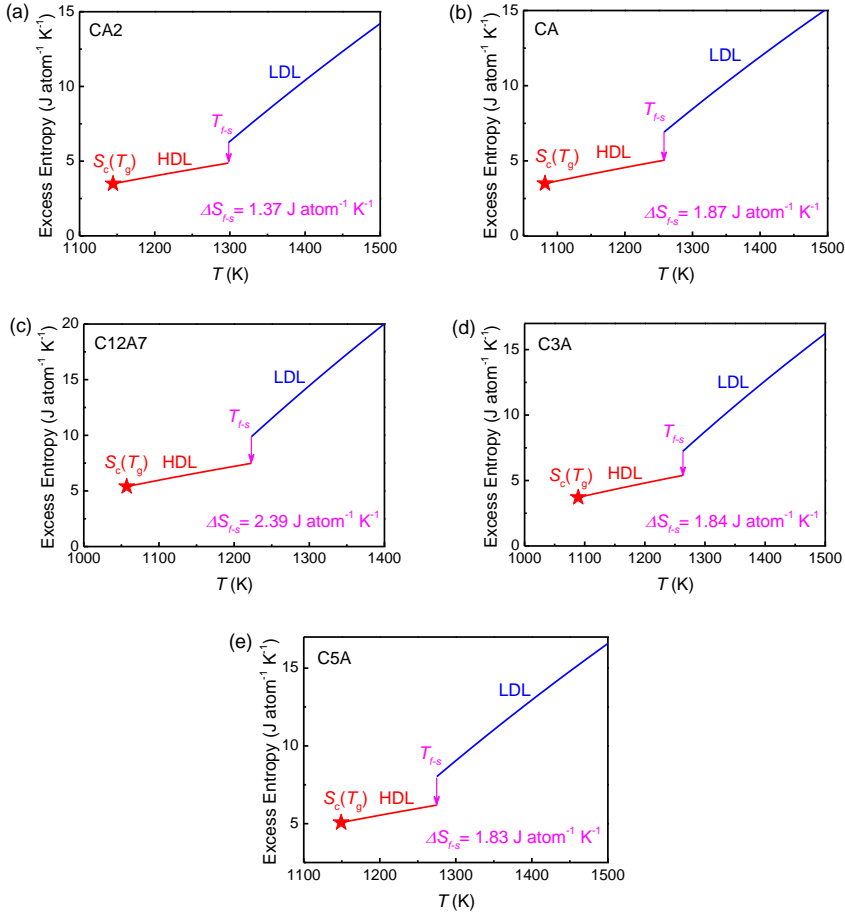


**Figure 4-11** Excess entropy as a function of the temperature for (a) CA2, (b) CA, (c) C12A7, (d) C3A, and (e) C5A. The fragile (low density liquid, LDL) and strong (high density liquid, HDL) phases are shown as blue and red curves, respectively, which are calculated by using Adam-Gibbs model to fit the viscosity data. The reduction step during the  $f$ - $s$  transition upon cooling is shown as the pink arrow.

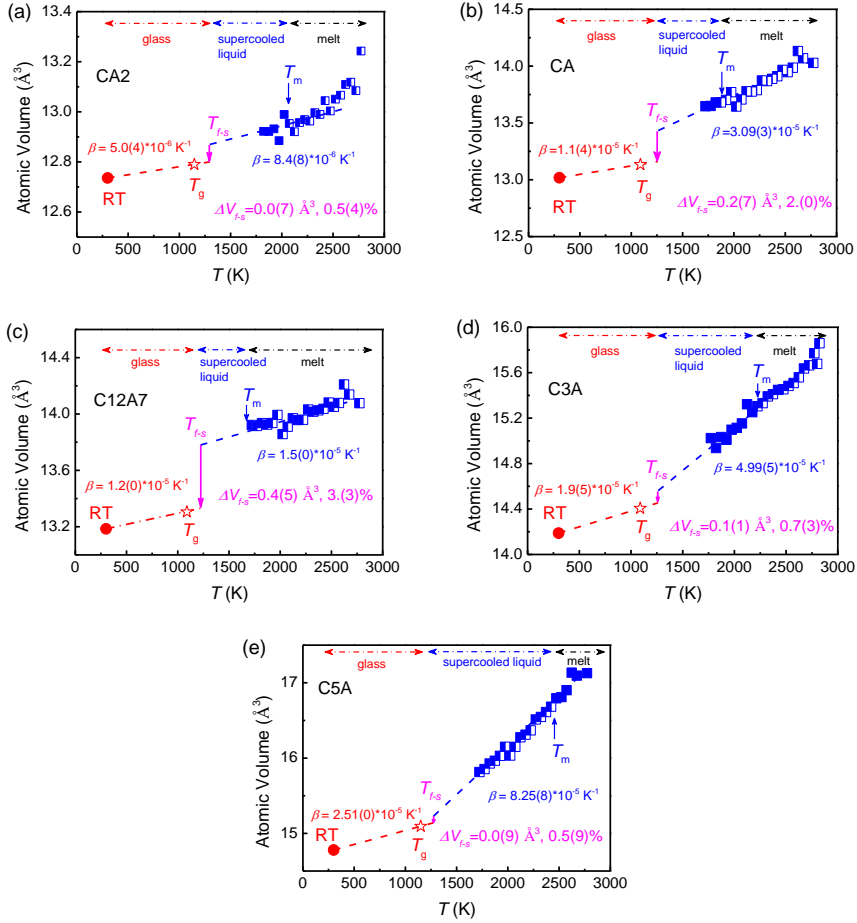


**Figure 4-12** Atomic volume as a function of the temperature for (a) CA2, (b) CA, (c) C12A7, (d) C3A, and (e) C5A. The fragile and strong phases are shown as blue and red curves, respectively. The volume CTEs ( $\beta$ ) of glasses are collected from literature [142,178-181], while those of liquids are determined from the temperature dependence of liquid density (blue data) measured in ALF. The reduction step during the  $f$ - $s$  transition upon cooling is shown as the pink arrow.



# CHAPTER 5. CORRELATION BETWEEN STRUCTURE, PHASE TRANSITIONS, AND DYNAMICS

Due to the complex structural behavior of amorphous states which include liquids and glasses, the composition-structure-property relation is a longstanding issue in glass science and technology. Although this relation has been thoroughly explored by numerous studies in various systems, it still remains elusive in many aspects, e.g., the origin of  $C_{p,conf}(T_g)$ , phase separation, phase transition, and  $f$ - $s$  transition.

## 5.1. BORATE-SILICATE GLASSES

As discussed in Section 3.1,  $T_g$  first increases from 830 to 855 K as  $B_2O_3$  is initially added, and rapidly decreases to 777 K with increasing  $q$  for  $q > 0.16$  (Fig. 3-1). According to previously studies of the temperature-constraint theory and “boron anomaly”, the non-monotonic variation of  $T_g$  with composition is mainly caused by the constraints (linear  $\alpha$  and angular  $\beta$ ) and the SRO structural conversion between  $B^{III}$  and  $B^{IV}$  species [18]. However, the non-linear variation of  $C_{p,conf}(T_g)$  cannot well explained in terms of SRO structure as discussed in Section 3.1 (Fig. 3-2, 3-3). For borate systems, it has been found that the freezing-in temperature of IRO structures ( $T_{gIRO}$ ) determined by in-situ high temperature Raman spectroscopy coupled well with  $T_g$ , whereas that of SRO structures ( $T_{gSRO}$ ) was much larger than  $T_g$  [53,106], indicating interactions between SRO structures happen at higher temperature than  $T_g$ . Furthermore, IRO structural units (borate rings) can thermally break without the structural changes in SRO [166,167]. The displacement of atoms in IRO structural units could give rise to the increase of the heat capacity, while no significant changes of SRO units occur. According to our Raman results, abundant superstructures containing different number of borate rings exist, giving excess conformational states to the glass network and a higher probability to sample high energy configurations in the energy landscape [42,48,79,80]. Besides, the number of types of IRO units reflects the abundance of microscopic states, giving rise to the increase of configurational entropy. Therefore, the rearrangement and inter-cooperation of IRO structural units could play a critical role in the structural relaxation and hence in influencing the  $C_{p,conf}(T_g)$ .

Fig. 5-1 shows the relation between  $C_{p,conf}(T_g)$  and the content of IRO structural units. The linear relationship confirms that IRO superstructures have a major contribution to  $C_{p,conf}(T_g)$  in borate-silicate glasses. In the silica-rich compositions ( $0.08 < q < 0.32$ ), danburite-like unit (mixed Si-O-B structure) and six-membered borate ring with  $B^{IV}$  have a major effect on the rapid increase of  $C_{p,conf}(T_g)$  as  $B_2O_3$

content increases. In the composition region of  $0.32 < q < 0.68$ , the danburite-like units diminish, and the counteraction between the decrease of the fraction of two types of metaborate groups and the increase of the fraction of other borate superstructural units (particularly six-membered borate rings) keeps the  $C_{p,conf}(T_g)$  unchanged. In the borate-rich compositions ( $q > 0.68$ ), both the six-membered borate rings with  $B^{IV}$  and boroxol has a positive effect on the increase of  $C_{p,conf}(T_g)$  with  $q$ . Therefore, the overall results suggest a strong correlation between IRO superstructures and  $C_{p,conf}(T_g)$  for  $Na_2O$ - $CaO$ - $B_2O_3$ - $SiO_2$  glasses.

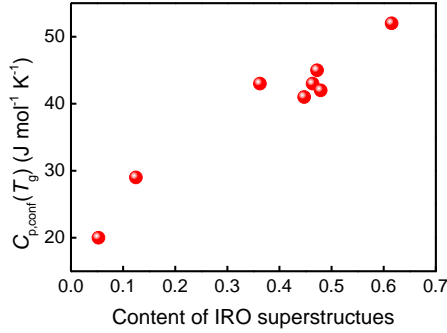


**Figure 5-1** The relation between  $C_{p,conf}(T_g)$  and the content of IRO superstructures.

Besides, we also explore the evolution of  $S_{conf}(T_g)$  with composition. According to Adam-Gibbs theory, for a series of glasses,  $S_{conf}(T_g)$  is inversely proportional to the value of  $T_g$  [188]. Therefore, in our studied borate-silicate glasses,  $S_{conf}(T_g)$  is expected to decrease initially in  $SiO_2$ -rich composition and rapidly increase with further increase of  $q$ . The different evolutions of  $S_{conf}(T_g)$  and  $C_{p,conf}(T_g)$  with composition indicate that the abundant IRO superstructures cannot fully contribute to the  $S_{conf}(T_g)$ . According to laws of thermodynamics,  $C_{p,conf}(T)$  can be written as below:

$$C_{p,conf}(T) = \left( \frac{\partial H_{conf}(T)}{\partial T} \right)_P = \left( \frac{\partial H_{conf}(T)}{\partial S_{conf}(T)} \right)_P \cdot \left( \frac{\partial S_{conf}(T)}{\partial T} \right)_P = T_{conf} \cdot \left( \frac{\partial S_{conf}(T)}{\partial T} \right)_P \quad (5.1)$$

where  $H_{conf}(T)$  is the configurational enthalpy, and  $T_{conf}$  is the configurational temperature at constant pressure, which is equal to  $T_g$  for a standard cooling rate (10 K/min) [18,192]. The relation between  $S_{conf}(T_g)$ ,  $C_{p,conf}(T_g)$ , and kinetic liquid fragility index  $m$  can be explored by combining Adam-Gibbs equation with Eqs. 4.1 and 5.1:

$$S_{conf}(T_g) = \frac{C_{p,conf}(T_g)}{\frac{m}{m_0} - 1} \quad (5.2)$$

Therefore, we infer that  $S_{\text{conf}}(T_g)$  is influenced by  $m$  and  $C_{\text{p,conf}}(T_g)$ . As  $q$  increases from 0 to 0.32,  $m$  has a major contribution to  $S_{\text{conf}}(T_g)$ . Specifically, the high kinetic barrier of atomic diffusion (low  $m$ ) limits the system to sample various basins in the energy landscape and hence occupy less microstates, leading to the decrease of  $S_{\text{conf}}(T_g)$  with the initial addition of  $\text{B}_2\text{O}_3$  in  $\text{SiO}_2$ -rich compositions. As  $q$  increase from 0.32 to 1.0,  $C_{\text{p,conf}}(T_g)$  has a dominant effect on  $S_{\text{conf}}(T_g)$ , i.e., the large amount and abundant types of IRO superstructures guarantee the increase of  $S_{\text{conf}}(T_g)$  with further addition of  $\text{B}_2\text{O}_3$ .

## 5.2. MIXED NETWORK FORMER GLASSES

As shown in Fig. 3-5(a), both  $T_{g1}$  and  $T_{g2}$  decrease linearly with substitution of  $\text{SiO}_2$  by  $\text{B}_2\text{O}_3$ . In the glasses containing multiple network formers, glass properties vary non-monotonically with the substitution between network formers, i.e., mixed network former effect, e.g., non-linear change of glass transition temperature ( $T_g$ ) with composition in  $\text{Na}_2\text{O}$ - $\text{B}_2\text{O}_3$ - $\text{P}_2\text{O}_5$  glasses [193]. The mixed network former effect is a result of the competition between different network formers to attract network modifier [193,194]. In contrast, for studied mixed network former glasses, the changing trends of two  $T_g$ s with composition are linear because of a lack of traditional modifiers. Moreover, the simultaneous decreases of  $T_{g1}$  and  $T_{g2}$  with  $\text{B}_2\text{O}_3$  content indicate that boron enters both the two glass phases ( $G_1$  and  $G_2$ ) to lower the network connectivity. The temperature range of  $T_{g1}$  is 650-840 K in the studied glasses, which is smaller than that in non-phase separated  $\text{B}_2\text{O}_3$ - $\text{Al}_2\text{O}_3$ - $\text{P}_2\text{O}_5$  glasses (840-1100 K) which is prepared by sol-gel method [95]. However, the  $T_g$  of the glass prepared by sol-gel method is much higher than that of melt-quenched glass ( $\sim 80$  K difference in Ref. [95]). In addition, the  $T_{g2}$  of the studied glasses (900-950 K) is in the temperature region of that for  $\text{B}_2\text{O}_3$ - $\text{P}_2\text{O}_5$ - $\text{SiO}_2$  glasses (770-970 K) [96]. Therefore, we infer that  $G_1$  (droplet) contains a B-O-B network with some  $\text{P}_2\text{O}_5$  and  $\text{Al}_2\text{O}_3$ , while  $G_2$  (matrix) contains a B-O-Si network with the remaining amount of  $\text{P}_2\text{O}_5$  and  $\text{Al}_2\text{O}_3$ . When  $\text{B}_2\text{O}_3$  substitutes  $\text{SiO}_2$ , the two phases compete to incorporate  $\text{B}_2\text{O}_3$ . For  $G_1$ , the increase of  $\text{B}_2\text{O}_3$  content leads to the increase of boroxol ring content and the decrease of the relative fraction of  $\text{B}^{\text{IV}}$  species in  $\text{BPO}_4$  units, leading to the decrease of  $T_{g1}$ . For  $G_2$ , the network changes from silica-rich to boron-rich network, giving rise to the decrease of  $T_{g2}$ .

The phase separation in mixed network former glasses has not previously been explored, and hence, it is essential to understand its mechanism. Stable immiscibility and metastable (sub-liquidus) immiscibility occurs at temperatures above and below the liquidus temperature, respectively. Furthermore, they can be distinguished by different macroscopic structures of glasses. For stable immiscibility, the melt-quenched glasses feature either layered structure or strongly opalescent appearance [109]. In contrast, the high viscosity (slow diffusion rate) of the liquids with metastable immiscibility often leads to the visually undetectable opalescence of the melt-quenched glasses. The fine-scale micro-separated phases can be “frozen in”, which are droplets and matrix phase, and may only be observed by electron

microscopy [109]. Therefore, we infer that the metastable immiscibility is the case for the studied glasses, which could be caused by the migration of oxygen vacancies. In the supercooled region, oxygen vacancies with relative high diffusivity rotate and react with neighboring oxygens, resulting in the change of the  $NNN$  of boron and the separated B-O-B and B-O-Si phases. The nano-phase separation in our studied glasses is similar to the spinodal phase separation found in sodium borosilicate glasses [195].

In addition, the observed nano-phase separation is associated with the structural ordering of  $G_2$  during heat treatments. As mentioned in Section 3.2, isothermal and multiple dynamic heating can induce the formation of ordered domains in  $G_2$ . Upon heating, these ordered domains grow at the temperature well below the offset of the second glass transition, leading to the partial crystallization of  $G_2$ . The existence of ordered domains reflects the high degree of structural heterogeneity in the melt-quenched glasses. Moreover, the degree of structural heterogeneity is especially significant in the  $G_2$  glass phase.

### 5.3. OXYFLUORIDE GERMANATE GLASSES

#### *Structural origin of $T_g$ changing trend with $T_d$*

As discussed in Section 3.3 (Fig. 3-11b), the evolution of  $T_g$  with  $T_d$  shows a three-stages variation, indicating that the mechanism of structural evolution changes during the dynamic heating. Based on our XRD and TEM results and previous studies, we propose a structural mechanism during the dynamic heating. When the as-prepared glass (60GeO<sub>2</sub>-25BaF<sub>2</sub>-15AlF<sub>3</sub>) is heated to the region of 820-903 K, the crystalline phase BaGeO<sub>3</sub> forms. Since BaO/GeO<sub>2</sub> ratio (i.e., the mole ratio of network modifier to network former) in BaGeO<sub>3</sub> crystal is much higher than that in as-prepared glass, the fraction of network former in the glass increases after precipitation of BaGeO<sub>3</sub>. Hence, the glass network becomes polymerized, leading to the increase of  $T_g$  with  $T_d$  in stage 1 (Fig. 3-11b). As  $T_d$  increases from 903 K to 925 K, BaF<sub>2</sub> and GeF<sub>4</sub> crystals form, and hence the composition of the glass becomes GeO<sub>2</sub>-rich. Therefore, the germanate speciation is associated with the variation of  $T_g$  with  $T_d$  in stages 2 and 3 (Fig. 3-11b). According to literature [47], the initial addition of network modifiers (alkali or alkaline earth oxides) into GeO<sub>2</sub> glass leads to abnormal changes of various properties including  $T_g$ , i.e., “germanate anomaly”. The “germanate anomaly” normally occurs in the composition region with 5-20 mol% modifier. Since the content of modifier in as-prepared glass is close to 20 mol%, we infer that the non-monotonic variation of  $T_g$  with  $T_d$  in stages 2 and 3 is a results of “germanate anomaly”.

The presence of “germanate anomaly” could be result from the conversion between different Ge species and the formation of six-membered rings with GeO<sub>4</sub> tetrahedra [45,47]. As modifiers are initially added into GeO<sub>2</sub> glass, part of four-fold coordinated Ge species (Ge<sup>IV</sup>) are converted to five- or six-fold coordinated Ge

species ( $\text{Ge}^{\text{V}}$  or  $\text{Ge}^{\text{VI}}$ ), which are bonded to  $\text{GeO}_4$  tetrahedra through corner-shared oxygen [45]. Furthermore, the long bond of Ge-O leads to the formation of six-membered rings and cavities in which modifiers stay. When the contents of  $\text{Ge}^{\text{V,VI}}$  species and six-membered rings reach critical values, further addition of modifiers leads to the conversion from  $\text{Ge}^{\text{V,VI}}$  back to  $\text{Ge}^{\text{IV}}$  and the break of six-membered rings.

Therefore, in stage 2, the formation of  $\text{BaF}_2$  and  $\text{GeF}_4$  induces the conversion from  $\text{Ge}^{\text{IV}}$  to  $\text{Ge}^{\text{V, VI}}$  and the formation of six-membered rings by the consumption of NBO and  $\text{F}^-$  in the glass, giving rise to the increase of  $T_g$  with  $T_d$ . This structural evolution continuous until  $T_d$  reaches 925 K. In stage 3,  $\text{Ge}^{\text{V, VI}}$  species are converted back to  $\text{Ge}^{\text{IV}}$  species and germanate rings break down by virtue of the formation of  $\text{Al}_2\text{BaGe}_2\text{O}_8$  together with  $\text{BaF}_2$  and  $\text{GeF}_4$  in the glass. Therefore, this structural evolution lowers the network connectivity of the glass and its structure tends to  $\text{GeO}_2$ -like, i.e.,  $T_g$  decreases and approaches to that of  $\text{GeO}_2$  glass in the stage 3.

### ***Order-Disorder Transition***

As mentioned in Section 3.3, a reversible endotherm occurs at 925 K upon heating the glasses with  $T_d=925\text{-}986$  K. We argue that the endotherm is not a signature of glass transition, because its intensity is comparable to that of the corresponding exothermic peak in DSC downscan (Fig. 3-13a). Typically, a glass transition exhibits a much weak exothermic response upon cooling compared to the endotherm upon heating. According to TEM results, we infer that the endotherm is a result of structural transformation of nano-clusters (20 nm) from ordered to disordered structure. The occurrence of this order-disorder transition accompanies the split of the main crystallization peak at 1020 K (Fig. 5-2), indicating the disordered domains evolved from the nano-clusters are different with the amorphous matrix. Moreover, XRD patterns of the glasses with  $T_d=903$ , 925, and 943 K are similar (Fig. 2-10), whereas only two of them ( $T_d=925$  and 943 K) undergo the order-disorder transition upon heating (Fig. 3-11a). On one hand, the similarity of their XRD patterns illustrates that the nano-cluster lacks of long range order, i.e., disordered nature. However, the nano-cluster should have some degree of IRO, leading to the endothermic order-disorder transition. On the other hand, it indicates that the thermal fluctuation at 903 K is not high enough for the supercooled liquid to overcome the activation energy of the nano-cluster formation, although the chemical composition of the glass with  $T_d=903$  K fulfills the condition of the nano-cluster formation. Therefore, the structural heterogeneity of the oxyfluoride germanate glass becomes significant (i.e., large amount of nano-clusters) only when  $T_d$  is in the region of 925-986 K.

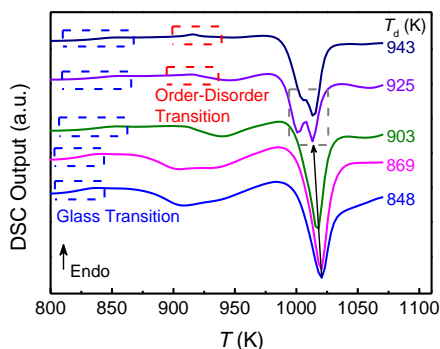


**Figure 5-2** DSC first upscans of the glasses dynamically heated to various  $T_d$ . Glass transition, order-disorder transition, and the split of the main crystallization peak are marked by blue, red, and gray box, respectively. The arrow shows the decrease of the crystallization peak temperature with increasing  $T_d$ .

To further reveal the formation mechanism of the nano-cluster, we consider the order-disorder transition together with  $T_g$ . Strikingly, the glass having maximum  $T_g$  starts to exhibit the order-disorder transition, i.e., the glass with  $T_d=925$  K. Therefore, we infer the nano-cluster could contain  $\text{Ge}^{\text{V, VI}}$  species and germanate rings. However, the structural evolution of the nano-cluster during this transition still needs to be revealed.

Fig. 5-3 shows the characteristic temperatures as a function of  $T_d$ . As  $T_d$  increases, the composition of the glass evolves from  $60\text{GeO}_2\text{-}25\text{BaF}_2\text{-}15\text{AlF}_3$  to  $\text{GeO}_2$ -rich. Upon heating, all glasses exhibit glass transition and crystallization, characterized by  $T_g$  and  $T_p$ , respectively. Moreover, the changing trends of  $T_g$  and  $T_p$  with the increase of  $T_d$  are non-monotonous, which is a result of “germanate anomaly”. For the glasses with  $T_d \geq 925$  K, nano-clusters form in amorphous matrix and undergo the order-disorder transition upon heating. The disordered domains evolved from the nano-clusters crystallize together with the amorphous matrix, giving rise to the splitting of the main crystallization peak.

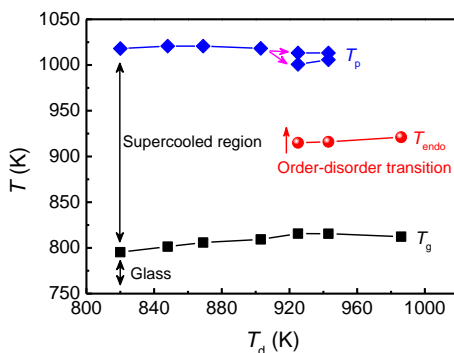


**Figure 5-3** Characteristic temperatures ( $T$ ) as a function of the dynamic heating temperature ( $T_d$ ) for  $60\text{GeO}_2\text{-}25\text{BaF}_2\text{-}15\text{AlF}_3$  glass system.  $T_g$ ,  $T_{\text{endo}}$ , and  $T_p$  refer to the glass transition temperature, the peak temperature of the endotherm characterizing the order-disorder transition, and the crystallization peak temperature, respectively. The pink arrows show the splitting of the crystallization peak into two sub-peaks.

As discussed in Section 4.3,  $C_{p,\text{conf}}(T_g)$  is proportional to  $m$  for studied glasses (Fig. 4-6). In  $60\text{GeO}_2\text{-}25\text{BaF}_2\text{-}15\text{AlF}_3$  liquid, the existence of large amount of  $\text{Ba}^{2+}$  and  $\text{F}^-$  guarantees the low viscosity, and hence the viscosity rapidly increases upon supercooling towards to  $T_g$ , leading to the high  $m$  and  $C_{p,\text{conf}}(T_g)$ . As  $T_d$  increases,  $\text{Ge}^{\text{V, VI}}$  polyhedra and six-membered rings strengthen the network and give rise to the high viscosity of the liquid, leading to the decrease of  $m$  and  $C_{p,\text{conf}}(T_g)$ . In addition, the liquid fragility and viscosity are closely associated with  $S_{\text{conf}}(T_g)$ . As discussed in Section 5.1,  $S_{\text{conf}}(T_g)$  is inversely proportional to  $T_g$  for a series of glasses [18,189]. Therefore, the evolution of  $S_{\text{conf}}(T_g)$  with  $T_d$  should exhibit a non-monotonic feature with a minimum at  $T_d=925$  K. There are two principal contributions - chemical and topological contributions - giving rise to the configurational entropy [196]. The chemical contribution mainly results from mixing of chemically distinguishable units and the degree of disorder of the network. The topological contribution is determined by the distributions of bond lengths and angles of polyhedra. As  $T_d$  increases from 820 K to 903 K, the decrease of NBO leads to the decrease of the distribution of various structural units, and hence chemical  $S_{\text{conf}}(T_g)$  decreases. As the composition of the glass enters “germanate anomaly” zone, the abundant structural species have significant effect on  $S_{\text{conf}}(T_g)$ .

## 5.4. CALCIUM ALUMINATE GLASSES

According to our MD results and experimental characterizations of structure, it can be seen that a variety of cation and oxygen configurations exist in  $\text{CaO-Al}_2\text{O}_3$  glasses and liquids, which are seldom found in conventional oxide glasses.

Furthermore, the simulated viscosity and  $G(r)$  are in good agreements with experiments, confirming the validity of MD results and reconciling rheology with atomic structure for this unusual oxide glass forming system. As the CaO content increases, the structural network of CaO-Al<sub>2</sub>O<sub>3</sub> evolves from compensated oxygen deficient random network (ODRN), through continuous random network (CRN) to incomplete random network (IRN) [3,197,198]. The evolution of structural network with composition across the binary calcium aluminate system provides insights to thermo-physical properties, thermodynamics, and rheology.

As mentioned in Section 3.4, a remarkable non-monotonic changing trend of  $T_g$  with  $C/(C+A)$  ratio is found in studied CaO-Al<sub>2</sub>O<sub>3</sub> glasses. The initial addition of CaO from CA2 to C12A7 leads to a decrease of the fraction of Al<sup>V, VI</sup> and tricluster oxygen and an increase of the fraction of NBO, and thereby lowers the connectivity of the [AlO<sub>4</sub>] network. However, the effect of NBO on depolymerization of glass network becomes weak as further increase of  $C/(C+A)$  ratio from C12A7 to C5A. Besides charge-balancing [AlO<sub>4</sub>] and forming NBO, excess CaO produces free oxygen in Ca-rich compositions, which does not participate in lowering the connectivity of the network. The shortage of enough Al<sup>3+</sup> results in a transformation from CRN (C12A7) to IRN (C5A) connected by CaO<sub>x</sub> polyhedra. This kind of topology is analogous to that of the invert glass, e.g., 2MgO-SiO<sub>2</sub> and 60CaO-30P<sub>2</sub>O<sub>5</sub>-3TiO<sub>2</sub>-7Na<sub>2</sub>O glasses [199,200]. The structure of these glasses can be regarded as an assemblage of different anionic polyhedra and cations. The negatively charged anionic polyhedra are held together by cations despite a certain degree of possible interlinking of the polyhedra by weak forces. Therefore, the network connectivity could be mainly governed by Ca-O network rather than Al-O network in Ca-rich composition region, and hence the increase of  $C/(C+A)$  ratio makes a positive contribution to  $T_g$ . On the other hand, in terms of the intermediate range order, CaO-rich glasses are believed to possess topologically disordered network consisting of large sized rings [121], which can also increase the degree of network connectivity.

In addition, the structural changes also result in non-monotonic variations of configurational entropy, viscosity, liquid fragility, and density [201]. As  $C/(C+A)$  ratio increases from CA2 to C12A7, the fraction of Al<sup>IV</sup> species and BO increases, leading to the increase of viscosity. In the meantime, the modifiers have high possibility to occupy the free volume of the network containing rich of AlO<sub>4</sub> tetrahedra, and hence the decrease of the free volume causes the increase of glass and liquid density. From C12A7 to C5A, since there are not enough Al<sup>IV</sup> sites, the broken AlO<sub>4</sub> network with CaO<sub>x</sub> polyhedra and the existence of free oxygen cause the decrease of density and viscosity.

We plot characteristic temperatures as a function of composition in the binary calcium-aluminates as shown in Fig. 5-4. Interestingly, all the changing trends exhibit a minimum at C12A7, which is consistent with the unique structure of



C12A7 (CRN). In addition, we also calculate three parameters characterizing the glass forming ability (GFA) as shown in Fig. 5-5. The original definition of GFA is the critical cooling rate of liquids, i.e.,  $q_{\text{crit}}$ . However, it is difficult and time-consuming to measure  $q_{\text{crit}}$ . Many researchers proposed various parameters for quantifying GFA [12,14,202-205]. Most of them correlated GFA with three main factors: structural information (e.g., bond type, molecular symmetry), thermodynamics (e.g., driving force of crystallization, cohesive energy) and kinetics (e.g., viscosity, nucleation and growth rate).  $T_g/T_m$  and  $\eta(T_m)$  reflect the depth of supercooling and the atomic diffusion to form periodic cells, respectively, both being proportional to the improved GFA.  $\Delta\rho_{\text{cryst-melt}}/\rho_{\text{melt}}$  shows the density mismatch of crystal and melt, reflecting how ease the structural arrangements proceed during the first order phase transition and how heterogeneous crystallization close to  $T_m$  preferentially favors nucleation. The GFA metrics shown in Fig 5-5 indicates the best GFA of C12A7 across the binary CaO-Al<sub>2</sub>O<sub>3</sub> system.

In addition, the existence of  $f$ - $s$  transition in supercooled CaO-Al<sub>2</sub>O<sub>3</sub> liquids causes the reductions of atomic volume and excess entropy at  $T_{f-s}$ , giving rise to the positive Clapeyron slope which is given by:

$$\frac{dT}{dP} = \frac{\Delta V_{f-s}}{\Delta S_{f-s}} \quad (5.3)$$

This indicates that supercooled CaO-Al<sub>2</sub>O<sub>3</sub> liquids behave in a similar way as supercooled metallic liquids [186,206,207], but different from the network structural liquids with liquid-liquid transitions ( $dT/dP < 0$ ) such as Y<sub>2</sub>O<sub>3</sub>-Al<sub>2</sub>O<sub>3</sub> and water [121,208-210]. For metallic liquids,  $dT/dP > 0$  could be caused by icosahedral packed structures with non-directional bonds. Although CaO-Al<sub>2</sub>O<sub>3</sub> liquids clearly have network topology, they can be envisaged as assembling of close packed AlO<sub>x</sub> and CaO<sub>x</sub> polyhedra. Fig. 5-6 shows the composition dependence of  $\Delta S_{f-s}$ ,  $\Delta V_{f-s}$  and the Clapeyron slope. Interestingly, their changing trends follow those characterizing GFA. Based on the structural information, C12A7 has a structure of CRN with improved atomic packing and complex structural species (e.g., AlO<sub>x</sub>, CaO<sub>x</sub>, tricluster oxygen, and free oxygen), giving rise to special characteristics of C12A7 glass and liquid in CaO-Al<sub>2</sub>O<sub>3</sub> system, i.e., the lowest characteristic temperatures and liquid CTE, the best GFA, and the largest step reductions at  $T_{f-s}$  in atomic volume and excess entropy, and the highest value of the Clapeyron slope.

Although the essential origin of  $f$ - $s$  transition is still on debate, numerous researchers tried to clarify its possible origin in different systems [211-218]. The simulation of silica energy landscape revealed that the  $f$ - $s$  transition might be related to the polymorphism behavior of silica glass [213]. The  $f$ - $s$  transition in water has been seen as the crossover from a non-glass forming to a glass-forming phase [186,211]. For CaO-Al<sub>2</sub>O<sub>3</sub> glass forming liquids, Hennet *et al.* found that an increase in the degree of intermediate-range order occurred at around  $1.25T_g$  for CA liquid, which is close to the dynamical crossover temperature [219]. This is consistent with our

finding that  $T_{f-s}$  is around  $1.15T_g$ , implying that structural evolution in intermediate-range order could have effects on  $f-s$  transition. Furthermore, it can be seen that  $T_{f-s}$  and  $T_p$  couple well through all compositions (Fig. 5-4), indicating that the heterogeneous crystallization is closely associated with the coexistence of strong and fragile polymorphs.

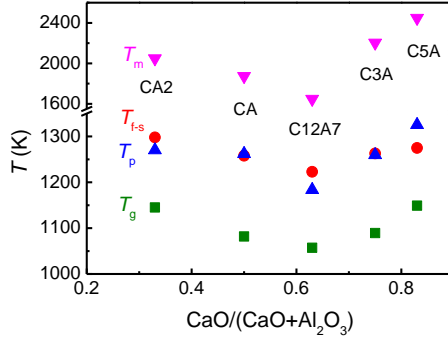


**Figure 5-4** Composition dependence of characteristic temperatures.  $T_g$ ,  $T_p$ ,  $T_{f-s}$ , and  $T_m$  refer to the glass transition temperature, crystallization peak temperature,  $f-s$  transition temperature, and melting temperature.  $T_g$  and  $T_p$  are determined by DSC curve.  $T_m$  data are obtained from the binary phase diagram.  $T_{f-s}$  data are calculated by using Eq.4.9.

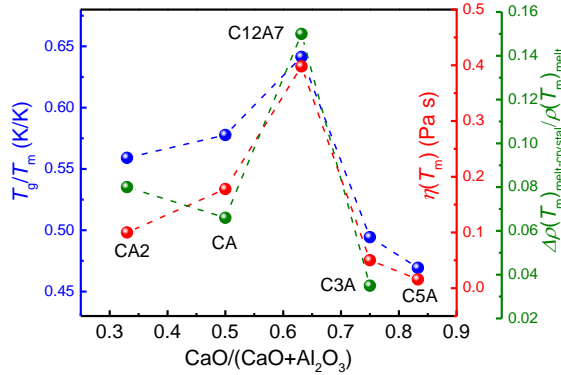


**Figure 5-5** GFA metrics  $T_g/T_m$ ,  $\eta(T_m)$ , and  $\Delta\rho(T_m)_{\text{melt-crystal}}/\rho(T_m)_{\text{melt}}$ . The density data of crystals and melts are obtained from MD simulation.

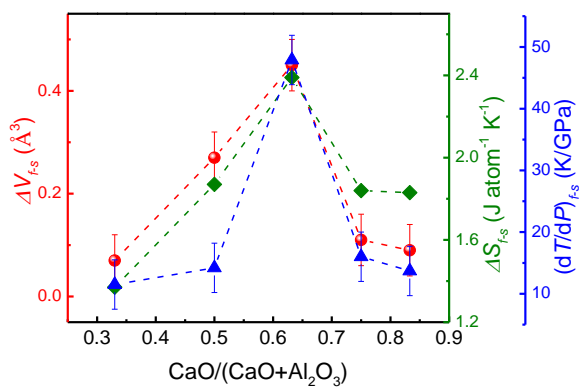


**Figure 5-6** The reduction step at  $T_{f-s}$  in atomic volume  $\Delta V_{f-s}$  and excess entropy  $\Delta S_{f-s}$  and the Clapeyron slope at  $T_{f-s}$ .

## CHAPTER 6. GENERAL DISCUSSION AND PERSPECTIVE

Since properties of glasses and liquids are essentially associated with microscopic structures, it is critical for understanding composition-structure-property relations for various systems. For the four studied oxide system, it can be seen that not only structural units in short-range order such as network former polyhedra, but also superstructures in intermediate-range order greatly influence properties such as  $T_g$ , liquid fragility, and entropy. Furthermore, temperature dependence of structural evolution plays a key role in thermodynamics of the cooling process from liquids to crystals or glasses. Therefore, an expanded relation, i.e., composition-temperature-structure-property, is proposed, which is helpful to design glasses with desirable properties and optimize parameters of glass manufacturing.

As one of the most crucial features in amorphous state, structural heterogeneity attracts great interests for exploring its physical meaning and underlying effects on various properties. For instance, structural heterogeneity is closely associated with the non-exponential slowing down of dynamics and phase separation in supercooled liquid [5,220-222]. Moreover, it can be retained in the glass by virtue of hyperquenching and result in complex enthalpic relaxation if the glass is re-heated to  $T_g$  [223-225]. In addition, ordered structures can still survive in equilibrium silicate liquid [226], indicating the memory effect of equilibrium liquids. Recently, zeolitic imidazolate frameworks (ZIFs) glass has been successfully prepared using melt-quenching method [227]. The ZIF glass exhibits polyamorphic transition upon heating, implying the presence of structural heterogeneity in this hybrid glass. We found three of the studied oxide systems exhibit structural heterogeneity in different degrees. For mixed network former glasses, ordered domains form in the glass matrix ( $G_2$ ) during isothermal heat treatments and/or multiple dynamic heating. The growth of the ordered domains interrupts the glass transition of  $G_2$  upon heating, and results in the interaction between the droplet ( $G_1$ ) and the residual part of  $G_2$ . For studied oxyfluoride germinate system, nano-clusters form during dynamic heating, leading to a reversible order-disorder transition. Both the two systems exhibit significant structural heterogeneity, which highly influence thermodynamics and glass transition. For binary calcium-aluminate system, the coexistence of fragile and strong phases around  $T_{f-s}$  results in abnormal change of dynamics ( $f-s$  transition).

As a property reflecting the glass network connectivity, the composition dependence of  $T_g$  is sensitive to SRO structural units and their interactions. For  $\text{Na}_2\text{O}-\text{CaO}-\text{B}_2\text{O}_3-\text{SiO}_2$  glasses, the non-monotonic variation of  $T_g$  with the  $\text{SiO}_2/\text{B}_2\text{O}_3$  substitution is mainly governed by  $N_4$  value, the fraction of NBO, and linear constraints of B-O and Si-O bonds. When  $\text{Na}_2\text{O}$  and  $\text{CaO}$  are replaced by  $\text{Al}_2\text{O}_3$  and  $\text{P}_2\text{O}_5$ , i.e.,  $\text{B}_2\text{O}_3-\text{Al}_2\text{O}_3-\text{SiO}_2-\text{P}_2\text{O}_5$  glasses, crystal-like units ( $\text{BPO}_4$  and  $\text{AlPO}_4$ ) form and nano-phase

separation takes place. In this case, boroxol rings and  $B^{III}$  non-ring species mainly governs the monotonic decrease of  $T_g$  with increasing  $B_2O_3$  content for borate and mixed borate-silicate glassy phase, respectively. When oxygen is partially substituted by fluorine, e.g., oxyfluoride germanate glasses ( $GeO_2$ - $BaF_2$ - $AlF_3$ ),  $F^-$  and NBO break the glass network, while  $Ge^{V, VI}$  species and germanate rings polymerize the glass network, leading to the non-monotonic variation of  $T_g$  with  $T_d$ . When there is a lack of traditional network former, e.g.,  $CaO$ - $Al_2O_3$  glasses, the structural network evolves from ODRN, through CRN to IRN containing  $AlO_x$  and  $CaO_x$  polyhedra with increasing  $CaO$  content. The oxygen tricluster and NBO mainly govern the network connectivity for  $Al_2O_3$ -rich compositions, whereas clusters of  $CaO_x$  polyhedra become predominant in governing  $T_g$  for  $CaO$ -rich compositions. For all the four system, it is observed that the change of the coordination number of network former cation significantly influence  $T_g$ .

The thermodynamics of glasses and liquids are investigated. In borate-silicate glasses, borate superstructures and mixed B-O-Si rings have major influence on  $C_{p,conf}(T_g)$ . In addition,  $S_{conf}(T_g)$  could be simultaneously governed by superstructures and angular constraints of O-B-O and O-Si-O bonds. In mixed network former glasses, structural heterogeneity and structural ordering greatly influence the degree of micro phase separation and crystallization. In oxyfluoride germanate glasses, the change of SRO germanate units and the existence of germanate rings results in the formation of nano-clusters (IRO units), which causes reversible order-disorder transition. In the binary calcium aluminate glass forming liquids, polyamorphism causes mismatching of atomic volume and excess entropy in the low and high temperature regions and hence an abrupt change at  $T_{f-s}$ . Therefore, the structural heterogeneity in IRO scale has great influence on thermodynamics of liquids and quenching-derived glasses.

In addition, the dynamics are also discussed in terms of viscosity and liquid fragility. For borate-silicate system, the liquid fragility is mainly governed by angular constraints of O-Si-O and O-B-O bonds. For mixed network former system, although it is difficult to precisely obtain  $m$  for each glass phase, we infer that this kind of glass-forming liquid is extremely strong due to a lack of traditional modifiers and the existence of crystal-like units such as  $BPO_4$  and  $AlPO_4$ . For oxyfluoride germanate system, the presence of  $F^-$  guarantees the ease of viscous flow in high temperature region, leading to the high value of  $m$ . For the binary calcium-aluminate system,  $f$ - $s$  transition exists across a wide composition range from CA2 to C5A – representing 50% of  $CaO$ - $Al_2O_3$  compositions. Furthermore, we try to explore the association between structure, glass transition, crystallization, and dynamics. Strikingly, various phase transitions occur in the temperature region of  $1.15$ - $1.2T_g$  regardless of the type of the system. For mixed network former glass forming system, the first crystallization peak temperature ( $T_p$ ) locates in the region of  $1.15$ - $1.18T_{g2}$ . For oxyfluoride germanate system, the peak temperature of the endotherm characterizing the order-disorder transition ( $T_{endo}$ ) is  $\sim 1.16T_g$ . For the

binary  $\text{CaO-Al}_2\text{O}_3$  system,  $T_{f-s}$  and  $T_p$  are  $\sim 1.15T_g$ , the dynamic cross-over temperature is  $\sim 1.2T_g$ , and the degree of IRO increases at  $\sim 1.25T_g$  [219]. Hence, the coherence of the three special oxide systems reconciles the structural heterogeneity, anomalous phase transition, and abnormal dynamics in this special temperature region, i.e.,  $1.15-1.2T_g$ . As supercooled liquid is cooled to approach  $\sim 1.2T_g$ , the ergodicity of the liquid is lost, the slow relaxation processes emerge, and the reciprocity between viscosity and ionic diffusion is broken, leading to the occurrence of a dynamic cross-over in structural heterogeneity.

## CHAPTER 7. CONCLUSION

We explored the evolution of structure and thermodynamics with substitution of  $\text{SiO}_2$  by  $\text{B}_2\text{O}_3$  in a series of  $\text{Na}_2\text{O-CaO-B}_2\text{O}_3\text{-SiO}_2$  glasses and liquids. The intermediate range order (IRO) structural units are found to govern the major change of the configurational heat capacity at  $T_g$  ( $C_{p,\text{conf}}(T_g)$ ) with composition. Specifically, in the  $\text{SiO}_2$ -rich glasses, the contents of B-O-Si (danburite-like) structural units and six-membered borate rings have a major contribution to the increase of  $C_{p,\text{conf}}(T_g)$ . In the intermediate compositions, the competition between the disruption of B-O-Si units and metaborate structure and the formation of other borate superstructures causes  $C_{p,\text{conf}}(T_g)$  to be approximately constant. In the  $\text{B}_2\text{O}_3$ -rich glasses, the continuous formation of six-membered borate rings causes a further increase of  $C_{p,\text{conf}}(T_g)$ . In addition, it is found that  $C_{p,\text{conf}}(T_g)$  is closely associated with the kinetic liquid fragility index  $m$ . Furthermore, the configurational entropy at  $T_g$  ( $S_{\text{conf}}(T_g)$ ) is mainly governed by IRO superstructures and angular constraints of O-B-O and O-Si-O bonds.

For mixed network former glass-forming system ( $\text{B}_2\text{O}_3\text{-Al}_2\text{O}_3\text{-SiO}_2\text{-P}_2\text{O}_5$ ), we investigated the structure, glass transition, nano-phase separation, and crystallization. With substitution of  $\text{SiO}_2$  by  $\text{B}_2\text{O}_3$ , all studied glasses exhibit nano-phase separation, i.e., droplets ( $G_1$ ) with length scales of 50-100 nm and the glassy matrix ( $G_2$ ). Based on the structural characterizations, we suggest that  $G_1$  is rich in boroxol rings and  $G_2$  mainly involves the B-O-Si network, but both contain  $\text{BPO}_4$  and  $\text{AlPO}_4$  units. As  $\text{B}_2\text{O}_3$  content increases, three-fold coordinated boron ( $\text{B}^{\text{III}}$ ) species become dominant, the content of four-fold coordinated aluminum ( $\text{Al}^{\text{IV}}$ ) species slightly increases, and the P speciation remains unchanged. These structural evolutions result in a decrease of the  $\text{BPO}_4$  units in  $G_1$  and boron-rich network of  $G_2$ , leading to the  $T_g$  decrease of for both phases. Structural ordering takes place in  $G_2$  during isothermal and dynamic heating, implying the structural heterogeneity in the melt-quenched  $\text{B}_2\text{O}_3\text{-Al}_2\text{O}_3\text{-SiO}_2\text{-P}_2\text{O}_5$  glasses. The ordered domains lower the activation energy of crystal growth, promoting the partial crystallization of  $G_2$  and the interaction between  $G_1$  and the residual part of  $G_2$  upon heating.

For oxyfluoride germinate glass-forming system ( $60\text{GeO}_2\text{-}25\text{BaF}_2\text{-}15\text{AlF}_3$ ), we studied the glass transition, crystallization, and order-disorder transition. Minor crystalline phases ( $\text{BaGeO}_3$ ,  $\text{GeF}_4$ ,  $\text{BaF}_2$ ) and major crystalline phase ( $\text{Al}_2\text{BaGe}_2\text{O}_8$ ) progressively form upon heating to  $\sim 50$  K above  $T_g$ . After heating the glass to the temperature region of 925-986 K, nano-clusters ( $\sim 20$  nm) form, which could contain five- and six-fold coordinated germanium species, and six-membered  $\text{GeO}_4$  rings. The nano-clusters undergo an order-disorder transition during DSC upscanning, giving rise to a reversible endotherm at 925 K. The formation and breaking-down of the nano-cluster are associated with the increase and decrease of  $T_g$  with increasing dynamic heating temperature, respectively.

For calcium-aluminate glass-forming system, we reconciled its structure, rheology, thermo-physics, and phase transition across wide composition and temperature regions. By using aerodynamic levitation furnace (ALF), the composition region of glass-forming is extended, i.e., from  $\text{CaO-2Al}_2\text{O}_3$  (CA2) to  $5\text{CaO-Al}_2\text{O}_3$  (C5A), and the supercooled region can be accessed without heterogeneous crystallization. With the substitution of CaO for  $\text{Al}_2\text{O}_3$ , the structural network evolves from oxygen deficient random network (ODRN) to incomplete random network (IRN) through continuous random network (CRN) at the deep eutectic (C12A7). Besides typical structural units, e.g.,  $\text{Al}^{\text{IV}}$ , BO and NBO, large amount of  $\text{Al}^{\text{V, VI}}$  species and tricluster oxygen exist in the liquids and glasses of ODRN and CRN, which are seldom found in traditional oxide glass-forming systems. As the CaO content increases from CA2 to C12A7, these special structures become less, resulting in the structure of CRN with improved atomic packing (C12A7). Further increase of the CaO content breaks the continuous  $\text{AlO}_4$  network, giving rise to the mix of  $\text{AlO}_4$  and  $\text{CaO}_x$  polyhedra. This structural evolution causes non-monotonic variations of characteristic temperatures, atomic density, CTE, and GFA metrics across the binary calcium-aluminate liquids and glasses, featuring a threshold at C12A7. Remarkably, a fragile-to-strong transition ( $f$ - $s$ ) is found to be ubiquitous in the supercooled  $\text{CaO-Al}_2\text{O}_3$  liquids. The  $f$ - $s$  transition is further confirmed by the drops of atomic volume and excess entropy at  $T_{f-s}$  upon cooling. The positive Clapeyron slope indicates calcium aluminate liquids can be envisaged as close packed polyhedra, although they have network topology.



## CHAPTER 8. BIBLIOGRAPHY

- [1] A. K. Varshneya, *Fundamentals of inorganic glasses*. Academic Press, 1994.
- [2] J. E. Shelby, *Introduction to Glass Science and Technology*. Cambridge: Royal Society of Chemistry, 2005.
- [3] G. N. Greaves, S. Sen, *Adv. Phys.* **56** (2007) 1–166.
- [4] A. Qiao, H. Tao, Y. Yue, *J. Am. Ceram. Soc.* **100** (2017) 968–974.
- [5] P. G. Debenedetti, F. H. Stillinger, *Nature* **410** (2001) 259–267.
- [6] Y. Z. Yue, *J. Non-Cryst. Solids* **354** (2008) 1112–1118.
- [7] Y. Z. Yue, *J. Non-Cryst. Solids* **355** (2009) 737–744.
- [8] G. Parisi, B. Seoane, *Phys. Rev. E* **89** (2014) 22309.
- [9] H. Doweidar, *J. Mater. Sci.* **25** (1990) 253–258.
- [10] P. Richet, *Geochim. Cosmochim. Acta* **48** (1984) 471–483.
- [11] W. Huang, C. S. Ray, D. E. Day, *J. Non-Cryst. Solids* **86** (1986) 204–212.
- [12] D. Turnbull, *Contemp. Phys.* **10** (1969) 473–488.
- [13] C. S. Ray, S. T. Reis, R. K. Brow, W. Höland, V. Rheinberger, *J. Non-Cryst. Solids* **351** (2005) 1350–1358.
- [14] Z. P. Lu, C. T. Liu, *Phys. Rev. Lett.* **91** (2003) 115505.
- [15] K. F. Kelton, A. L. Greer, *Nucleation in condensed matter : applications in materials and biology*. Pergamon, 2010.
- [16] C. A. Angell, *J. Non-Cryst. Solids* **73** (1985) 1–17.
- [17] C. A. Angell, *Science* **267** (1995) 1924–1935.
- [18] M. M. Smedskjaer, J. C. Mauro, R. E. Youngman, C. L. Hogue, M. Potuzak, Y. Z. Yue, *J. Phys. Chem. B* **115** (2011) 12930–12946.
- [19] D. Huang, G. B. McKenna, *J. Chem. Phys.* **114** (2001) 5621–5630.
- [20] S. Corezzi, L. Comez, D. Fioretto, *Eur. Phys. J. E* **14** (2004) 143–147.
- [21] Y. H. Yun, P. J. Bray, *J. Non-Cryst. Solids* **27** (1978) 363–380.
- [22] S. Z. Xiao, *J. Non-Cryst. Solids* **45** (1981) 29–38.
- [23] B. N. Meera, J. Ramakrishna, *J. Non-Cryst. Solids* **159** (1993) 1–21.
- [24] W. L. Konijnendijk, J. M. Stevels, *J. Non-Cryst. Solids* **20** (1976) 193–224.
- [25] W. H. Zachariasen, *J. Am. Chem. Soc.* **54** (1932) 3841–3851.
- [26] G. N. Greaves, *J. Non-Cryst. Solids* **71** (1985) 203–217.
- [27] G. N. Greaves, K. L. Ngai, *Phys. Rev. B* **52** (1995) 6358–6380.
- [28] J. C. Phillips, *J. Non-Cryst. Solids* **34** (1979) 153–181.
- [29] V. McGahay, M. Tomozawa, *J. Non-Cryst. Solids* **109** (1989) 27–34.
- [30] S. K. Lee, J. F. Stebbins, *Geochim. Cosmochim. Acta* **66** (2002) 303–309.
- [31] J. C. Mauro, C. S. Philip, D. J. Vaughn, M. S. Pambianchi, *Int. J. Appl. Glas. Sci.* **5** (2014) 2–15.
- [32] Y. Yue, Q. Zheng, *Int. J. Appl. Glas. Sci.* **8** (2017) 37–47.
- [33] P. F. Mcmillan, B. T. Poe, P. H. Gillet, B. Reynard, *Geochim. Cosmochim. Acta* **58** (1994) 3653–3664.
- [34] R. Kerner, J. C. Phillips, *Solid State Commun.* **117** (2000) 47–51.

- [35] G. Tricot, *Phys. Chem. Chem. Phys.* **18** (2016) 26764–26770.
- [36] W. Qu, S. Liu, Z. Xiao, J. Ma, M. Wei, *J. Alloys Compd.* **661** (2016) 1–5.
- [37] A. E. R. Westman, M. K. Murthy, *J. Am. Ceram. Soc.* **44** (1961) 475–480.
- [38] R. K. Brow, C. A. Click, T. M. Alam, *J. Non-Cryst. Solids* **274** (2000) 9–16.
- [39] R. Brow, *J. Non-Cryst. Solids* **263–264** (2000) 1–28.
- [40] J. J. Hudgens, R. K. Brow, D. R. Tallant, S. W. Martin, *J. Non-Cryst. Solids* **223** (1998) 21–31.
- [41] Y. D. Yiannopoulos, G. D. Chryssikos, E. I. Kamitsos, *Phys. Chem. Glas.* **42** (2001) 164–172.
- [42] T. Yano, N. Kunimine, S. Shibata, M. Yamane, *J. Non-Cryst. Solids* **321** (2003) 147–156.
- [43] J. C. Mauro, P. K. Gupta, R. J. Loucks, *J. Chem. Phys.* **126** (2007) 184511.
- [44] P. K. Gupta, J. C. Mauro, *J. Chem. Phys.* **126** (2007) 224504.
- [45] G. S. Henderson, *J. Non-Cryst. Solids*, **353** (2007) 1695–1704.
- [46] D. Di Martino, L. F. Santos, A. C. Marques, R. M. Almeida, *J. Non-Cryst. Solids* **293–295** (2001) 394–401.
- [47] A. C. Hannon, D. Di Martino, L. F. Santos, R. M. Almeida, *J. Non-Cryst. Solids* **353** (2007) 1688–1694.
- [48] M. Hubert, A. J. Faber, *Phys. Chem. Glas. Eur. J. Glas. Sci. Technol. B* **55** (2014) 136–158.
- [49] A. Ellison, I. A. Cornejo, *Int. J. Appl. Glas. Sci.* **1** (2010) 87–103.
- [50] K. Chun, S. Kim, C. Kang, *J. Nucl. Mater.* **298** (2001) 150–154.
- [51] B. G. Parkinson, D. Holland, M. E. Smith, A. P. Howes, C. R. Scales, *J. Non-Cryst. Solids* **351** (2005) 2425–2432.
- [52] P. Zhao, S. Kroeker, J. F. Stebbins, *J. Non-Cryst. Solids* **276** (2000) 122–131.
- [53] A. Winterstein-Beckmann, D. Möncke, D. Palles, E. I. Kamitsos, L. Wondraczek, *J. Non-Cryst. Solids* **401** (2014) 110–114.
- [54] P. M. Aguiar, S. Kroeker, *Solid State Nucl. Magn. Reson.* **27** (2005) 10–15.
- [55] G. D’Angelo, G. Carini, C. Crupi, M. Koza, G. Tripodo, C. Vasi, *Phys. Rev. B* **79** (2009) 14206.
- [56] A. Winterstein-Beckmann, D. Möncke, D. Palles, E. I. Kamitsos, L. Wondraczek, *J. Non-Cryst. Solids* **376** (2013) 165–174.
- [57] T. Edwards, T. Endo, H. Walton, S. Sen, *Science* **345** (2014) 1027–1029.
- [58] W. J. Dell, P. J. Bray, S. Z. Xiao, *J. Non-Cryst. Solids* **58** (1983) 1–16.
- [59] S. Sen, Z. Xu, J. . Stebbins, *J. Non-Cryst. Solids* **226** (1998) 29–40.
- [60] A. H. Silver, P. J. Bray, *J. Chem. Phys.* **29** (1958) 984–990.
- [61] A. H. Silver, P. J. Bray, *J. Chem. Phys.* **32** (1960) 288–292.
- [62] D. Manara, A. Grandjean, D. R. Neuville, *J. Non-Cryst. Solids* **355** (2009) 2528–2531.
- [63] J. F. Stebbins, S. E. Ellsworth, *J. Am. Ceram. Soc.* **79** (1996) 2247–2256.
- [64] T. J. Kiczinski, L.-S. Du, J. Stebbins, *J. Non-Cryst. Solids* **351** (2005) 3571–3578.
- [65] B. G. Parkinson, D. Holland, M. E. Smith, a. P. Howes, C. R. Scales, *J.*

- Phys. Condens. Matter* **19** (2007) 1–12.
- [66] R. N. Sinclair, C. E. Stone, A. C. Wright, I. G. Polyakova, N. M. Vedishcheva, B. A. Shakhmatkin, S. A. Feller, B. C. Johanson, P. Venhuizen, R. B. Williams, A. C. Hannon, *Phys. Chem. Glas.* **41** (2000) 286–289.
  - [67] S. Kroeker, S. A. Feller, M. Affatigato, C. P. O. Brien, W. J. Clarida, M. Kodama, *Phys. Chem. Glas.* **44** (2003) 54–58.
  - [68] M. Lenoir, A. Grandjean, Y. Linard, B. Cochain, D. R. Neuville, *Chem. Geol.* **256** (2008) 316–325.
  - [69] F. Angeli, O. Villain, S. Schuller, T. Charpentier, D. de Ligny, L. Bressel, L. Wondraczek, *Phys. Rev. B*, **85** (2012) 54110.
  - [70] D. Möncke, G. Tricot, A. Winterstein-Beckmann, L. Wondraczek, E. I. Kamitsos, *Phys. Chem. Glas. Eur. J. Glas. Sci. Technol. Part B* **56** (2015) 203–211.
  - [71] D. Möncke, *Phys. Chem. Glas. Eur. J. Glas. Sci. Technol. Part B* **56** (2015) 235–247.
  - [72] G. R. Srinivasan, I. Tweer, P. B. Macedo, A. Sarkar, W. Haller, *J. Non-Cryst. Solids* **6** (1971) 221–239.
  - [73] N. Kreidl, *J. Non-Cryst. Solids* **129** (1991) 1–11.
  - [74] J. W. Cahn, *J. Chem. Phys.* **42** (1965) 93–99.
  - [75] M. Tomozawa, V. McGahay, J. M. Hyde, *J. Non-Cryst. Solids* **123** (1990) 197–207.
  - [76] D. Manara, A. Grandjean, D. R. Neuville, *Am. Mineral.* **94** (2009) 777–784.
  - [77] X. Zhao, J. Fukunaga, N. Yoshida, M. Ihara, *Ceram. Soc. Japan*, vol. 93, pp. 48–56, 1985.
  - [78] J. Fukunaga, X. Zhao, M. Ihara, R. Ota, Y. Onoda, *Soc. Mater. Sci. Japan*, **37** (1988) 87–93.
  - [79] T. Yano, N. Kunimine, S. Shibata, M. Yamane, *J. Non-Cryst. Solids* **321** (2003) 137–146.
  - [80] T. Yano, N. Kunimine, S. Shibata, M. Yamane, *J. Non-Cryst. Solids* **321** (2003) 157–168.
  - [81] D. Möncke, G. Tricot, D. Ehrt, E. I. Kamitsos, *J. Chem. Technol. Metall.* **50** (2015) 381–386.
  - [82] E. I. Kamitsos, M. A. Karakassides, G. D. Chryssikos, *Phys. Chem. Glas.* **30** (1989) 229–234.
  - [83] E. I. Kamitsos, G. D. Chryssikos, *J. Mol. Struct.* **247** (1991) 1–16.
  - [84] L. S. Du, J. F. Stebbins, *J. Non-Cryst. Solids* **315** (2003) 239–255.
  - [85] T. Furukawa, W. B. White, *J. Mater. Sci.* **16** (1981) 2689–2700.
  - [86] O. N. Koroleva, L. a. Shabunina, V. N. Bykov, *Glas. Ceram.* **67** (2011) 340–342.
  - [87] E. I. Kamitsos, M. a. Karakassides, G. D. Chryssikos, *Phys. Chem. Glas.* **28** (1987) 203–209.
  - [88] L. Cormier, O. Maj érus, D. R. Neuville, G. Calas, *J. Am. Ceram. Soc.* **89** (2006) 13–19.

- [89] Q. Zheng, M. M. Smedskjaer, R. E. Youngman, M. Potuzak, J. C. Mauro, Y. Z. Yue, *Appl. Phys. Lett.* **101** (2012) 1–5.
- [90] Q. J. Zheng, R. E. Youngman, C. L. Hogue, J. C. Mauro, M. Potuzak, M. M. Smedskjaer, Y. Z. Yue, *Phys. Rev. B* **86** (2012) 54203.
- [91] R. E. Youngman, B. G. Aitken, *Phys. Chem. Glas. Eur. J. Glas. Sci. Technol. B* **50** (2009) 183–188.
- [92] S. Kapoor, X. Guo, R. E. Youngman, C. L. Hogue, J. C. Mauro, S. J. Rzoska, M. Bockowski, L. R. Jensen, M. M. Smedskjaer, *Phys. Rev. Appl.* **7** (2017) 1–16.
- [93] B. G. Aitken, R. E. Youngman, R. R. Deshpande, H. Eckert, *J. Phys. Chem. C* **113** (2009) 3322–3331.
- [94] W. A. Buckermann, C. Mundus, P. Chemie, D. W. Wilhelms-universiti, D.-Munster, *J. Non-Cryst. Solids* **208** (1996) 217–227, 1996.
- [95] L. Zhang, H. Eckert, *J. Mater. Chem.* **15** (2005) 1640.
- [96] B. G. Aitken, R. E. Youngman, *Phys. Chem. Glas. Eur. J. Glas. Sci. Technol. Part B* **47** (2006) 381–387.
- [97] R. E. Youngman, B. G. Aitken, J. E. Dickinson, *J. Non-Cryst. Solids* **264** (2000) 111–116.
- [98] J. E. Dickinson, B. H. W. S. de Jong, *J. Non-Cryst. Solids* **102** (1988) 196–204.
- [99] S. G. Kosinski, D. M. Krol, T. M. Duncan, D. C. Douglass, J. B. MacChesney, J. R. Simpson, *J. Non-Cryst. Solids*, vol. 105, pp. 45–52, 1988.
- [100] K. J. D. Mackenzie, M. E. Smith, *Multinuclear Solid-State Nuclear Magnetic Resonance of Inorganic Materials*. Pergamon an Imprint of Elsevier Science, 2002.
- [101] D. Müller, E. Jahn, G. Ladwig, U. Haubenreisser, *Chem. Phys. Lett.* **109** (1984) 332–336.
- [102] S. Sen, R. E. Youngman, *J. Phys. Chem. B* **108** (2004) 7557–7564.
- [103] H. Gan, P. C. Hess, R. J. Kirkpatrick, *Geochim. Cosmochim. Acta* **58** (1994) 4633–4647.
- [104] H. Liu, M. M. Smedskjaer, H. Tao, L. R. Jensen, X. Zhao, Y. Z. Yue, *Phys. Chem. Chem. Phys.* **18** (2016) 10887–10895.
- [105] L. Koudelka, P. Mošner, *Mater. Lett.* **42** (2000) 194–199.
- [106] A. Winterstein-Beckmann, D. Möncke, D. Palles, E. I. Kamitsos, L. Wondraczek, *J. Non-Cryst. Solids* **405** (2014) 196–206.
- [107] H. Yamashita, K. Nagata, H. Yoshino, K. Ono, T. Maekawa, *J. Non-Cryst. Solids* **248** (1999) 115–126.
- [108] J. F. MacDowell, EP0202751 A1 (1986).
- [109] P. F. James, *J. Mater. Sci.* **10** (1975) 1802–1825.
- [110] S. Nishibu, S. Yonezawa, M. Takashima, *J. Non-Cryst. Solids* **351** (2005) 1239–1245.
- [111] R. El-Mallawany, A. H. Khafagy, M. A. Ewaida, I. Z. Hager, M. A. Poulain, M. J. Poulain, *J. Non-Cryst. Solids* **184** (1995) 141–146.

- [112] L. F. Santos, R. M. Almeida, V. K. Tikhomirov, A. Jha, *J. Non-Cryst. Solids* **284** (2001) 43–48.
- [113] Y. Hu, J. Qiu, Z. Song, Z. Yang, Y. Yang, D. Zhou, Q. Jiao, C. Ma, *J. Lumin.* **145** (2014) 512–517.
- [114] J. E. Shelby, *J. Am. Ceram. Soc.* **57** (1974) 436–439.
- [115] G. Cao, F. Lin, H. Hu, F. Gan, *J. Non-Cryst. Solids* **326–327** (2003) 170–176.
- [116] S. S. Bayya, B. B. Harbison, J. S. Sanghera, I. D. Aggarwal, *J. Non-Cryst. Solids* **212** (1997) 198–207.
- [117] H. Nii, K. Ozaki, M. Herren, M. Morita, *J. Lumin.* **76–77** (1998) 116–119.
- [118] H. Fan, G. Gao, G. Wang, J. Hu, L. Hu, *Opt. Mater.* **32** (2010) 627–631.
- [119] S. A. Polishchuk, L. N. Ignat’eva, Y. V. Marchenko, V. M. Bouznik, *Glas. Phys. Chem.* **37** (2011) 1–20.
- [120] J.-L. Adam, *J. Fluor. Chem.* **107** (2001) 265–270.
- [121] J. Akola, S. Kohara, K. Ohara, A. Fujiwara, Y. Watanabe, A. Masuno, T. Usuki, T. Kubo, A. Nakahira, K. Nitta, T. Uruga, J. K. R. Weber, C. J. Benmore, *Proc. Natl. Acad. Sci. USA* **110** (2013) 10129–34.
- [122] W. J. Chung, J. Heo, *J. Am. Ceram. Soc.* **84** (2004) 348–52.
- [123] W. H. Dumbaugh, *Opt. Eng.* **24** (1985) 242257.
- [124] L. Cormier, D. R. Neuville, G. Calas, *J. Non-Cryst. Solids* **274** (2000) 110–114.
- [125] A. C. Hannon, J. M. Parker, *J. Non-Cryst. Solids* **274** (2000) 102–109.
- [126] C. Benmore, J. K. R. Weber, *J. Phys. Condens. Matter.* **15** (2003) S2413–S2423.
- [127] Q. Mei, C. J. Benmore, S. Sampath, J. K. R. Weber, K. Leinenweber, S. Amin, P. Johnston, J. L. Yarger, *J. Phys. Chem. Solids* **67** (2006) 2106–2110.
- [128] L. Kerns, M. C. Weinberg, S. Myers, R. Assink, *J. Non-Cryst. Solids* **232–234** (1998) 86–92.
- [129] J. F. Stebbins, J. V. Oglesby, S. Kroeker, *Am. Mineral.* **86** (2001) 1307–1311.
- [130] J. Allwardt, S. K. Lee, J. F. Stebbins, *Am. Mineral.* **88** (2003) 949–954.
- [131] B. T. Poe, P. F. Mcmillan, B. Cote, S. G. Recherche, D. Massiot, J. Coutures, *J. Am. Ceram. Soc.* **77** (1994) 1832–1838.
- [132] P. F. McMillan, W. T. Petuskey, B. Cote, D. Massiot, C. Landron, J. Coutures, *J. Non-Cryst. Solids* **195** (1996) 261–271.
- [133] D. R. Neuville, L. Cormier, D. Massiot, *Chem. Geol.* **229** (2006) 173–185.
- [134] P. McMillan, B. Piriou, A. Navrotsky, *Geochim. Cosmochim. Acta* **46** (1982) 2021–2037.
- [135] P. McMillan, B. Piriou, *J. Non-Cryst. Solids*, vol. 55, pp. 221–242, 1983.
- [136] L. Cormier, D. Ghaleb, D. R. Neuville, J.-M. Delaye, G. Calas, *J. Non-Cryst. Solids* **332** (2003) 255–270.
- [137] E.-T. Kang, S.-J. Lee, A. C. Hannon, *J. Non-Cryst. Solids* **352** (2006) 725–736.

- [138] R. N. Mead, G. Mountjoy, *J. Phys. Chem. B* **110** (2006) 14273–14278.
- [139] C. Xu, C. Wang, J. Yu, R. Zhang, J. Ren, X. Liu, J. Qiu, *J. Am. Ceram. Soc.* **100** (2017) 2852–2858.
- [140] J. W. E. Drewitt, S. Jahn, V. Cristiglio, A. Bytchkov, M. Leydier, S. Brassamin, H. E. Fischer, L. Hennet, *J. Phys. Condens. Matter* **23** (2011) 155101.
- [141] F. Kargl, C. Yuan, G. N. Greaves, *Int. J. Microgravity Sci. Appl.* **32** (2015) 320200.
- [142] D. Langstaff, M. Gunn, G. N. Greaves, A. Marsing, F. Kargl, *Rev. Sci. Instrum.* **84** (2013) 12.
- [143] E. V. Uhlmann, M. C. Weinberg, N. J. Kreidl, A. A. Goktas, *J. Am. Ceram. Soc.* **76** (1993) 449–453.
- [144] Y. -M. Sung, S. -J. Kwon, *J. Mater. Sci. Lett.* **18** (1999) 1267–1269.
- [145] I. Daniel, P. F. McMillan, P. Gillet, B. T. Poe, *Chem. Geol.* **128** (1996) 5–15.
- [146] M. Licheron, V. Montouillout, F. Millot, D. R. Neuville, *J. Non-Cryst. Solids* **357** (2011) 2796–2801.
- [147] D. R. Neuville, G. S. Henderson, L. Cormier, D. Massiot, *Am. Mineral.* **95** (2010) 1580–1589.
- [148] B. Mysen, D. Virgo, I. Kushiro, *Am. Mineral.* **66** (1981) 678.
- [149] F. Seifert, B. Mysen, D. Virgo, *Am. Mineral.* **67** (1982) 696.
- [150] P. N. Sen, M. F. Thorpe, *Phys. Rev. B* **15** (1977) 4030–4038.
- [151] F. L. Galeener, *Phys. Rev. B* **19** (1979) 4292–4297.
- [152] G. A. Rankin, *Am. J. Sci.* **s4-39** (1915) 1–79.
- [153] G. Eriksson, A. D. Pelton, *Metall. Trans. B* **24** (1993) 807–816.
- [154] V. M. Fokin, E. D. Zanolto, N. S. Yuritsyn, J. W. P. Schmelzer, *J. Non-Cryst. Solids* **352** (2006) 2681–2714.
- [155] N. Karpukhina, R. G. Hill, R. V. Law, *Chem. Soc. Rev.* **43** (2014) 2174.
- [156] M. Weinberg, E. D. Zanolto, S. Manrich, *Phys. Chem. Glasses* **33** (1992) 99–102.
- [157] J. W. P. Schmelzer, A. S. Abyzov, V. M. Fokin, C. Schick, E. D. Zanolto, *J. Non-Cryst. Solids* **429** (2015) 24–32.
- [158] L. M. Martinez, C. A. Angell, *Nature* **410** (2001) 663–667.
- [159] W. Kauzmann, *Chem Rev* **43** (1948) 219–256.
- [160] Y. Z. Yue, J. D. Christiansen, S. L. Jensen, *Chem. Phys. Lett.* **357** (2002) 20–24.
- [161] X. Guo, M. Potuzak, J. C. Mauro, D. C. Allan, T. J. Kiczanski, and Y. Z. Yue, *J. Non-Cryst. Solids* **357** (2011) 3230–3236.
- [162] J. C. Mauro, R. J. Loucks, P. K. Gupta, *J. Phys. Chem. A* **111** (2007) 7957–7965.
- [163] R. G. Palmer, *Adv. Phys.* **31** (1982) 669–735.
- [164] O. Maj érus, L. Cormier, G. Calas, B. Beuneu, *Phys. Rev. B* **67** (2003) 1–7.
- [165] P. Richet, M. Ali Bouhifd, P. Courtial, C. T áquí, *J. Non-Cryst. Solids* **211** (1997) 271–280.

- [166] H. B. Ke, P. Wen, W. H. Wang, *AIP Adv.* **2** (2012) 1–20.
- [167] W. H. Wang, *Prog. Phys.* **33** (2013) 5–177.
- [168] F. Angeli, T. Charpentier, D. De Ligny, C. Cailleteau, *J. Am. Ceram. Soc.* **93** (2010) 2693–2704.
- [169] S. Sen, *J. Non-Cryst. Solids* **253** (1999) 84–94.
- [170] J. F. Stebbins, S. E. Ellsworth, *J. Am. Ceram. Soc.* **79** (1996) 2247–56.
- [171] J. Wu, J. Deubener, J. F. Stebbins, L. Grygarova, H. Behrens, L. Wondraczek, Y. Z. Yue, *J. Chem. Phys.* **131** (2009) 104504.
- [172] J. Wu, J. F. Stebbins, *J. Non-Cryst. Solids* **356** (2010) 2097–2108.
- [173] K. J. Rao, *Structural Chemistry of Glasses* **125** (2002).
- [174] J. E. Shelby, C. M. Shaw, M. S. Spess, *J. Appl. Phys.* **66** (1989) 1149–1154.
- [175] P. L. Higby, R. J. Ginther, I. D. Aggarawal, E. J. Friebele, *J. Non-Cryst. Solids* **126** (1990) 209–215.
- [176] L. Cormier, D. R. Neuville, G. Calas, *J. Am. Ceram. Soc.* **88** (2005) 2292–2299.
- [177] A. G. Kalampounias, N. K. Nasikas, Y. Pontikes, G. N. Papatheodorou, *Phys. Chem. Glas. - Eur. J. Glas. Sci. Technol. Part B* **53** (2012) 205–209.
- [178] A. S. M. Rao, K. Narender, *J. Thermodyn.* **2014** (2014) 123478.
- [179] S. Jonas, F. Nadachowski, D. Szwagierczak G. Wójcik, *J. Eur. Ceram. Soc.* **26** (2006) 2273–2278.
- [180] S. Jonas, F. Nadachowski, D. Szwagierczak, *Science* **25** (1999) 77–84.
- [181] R. W. Whatmore, C. O'Hara, B. Cockayne, G. R. Jones, B. Lent, *Mater. Res. Bull.* **14** (1979) 967–972.
- [182] C. T. Moynihan, S. K. Lee, M. Tatsumisago, T. Minami, *Thermochim. Acta* **280–281**(1996) 153–162.
- [183] R. W. Douglas, W. L. Armstrong, J. P. Edward, D. Hall, *Glas. Technol.* **6** (1965) 52–55.
- [184] Y. Z. Yue, R. Von der Ohe, S. L. Jensen, *J. Chem. Phys.* **120** (2004) 8053–8059.
- [185] J. C. Mauro, Y. Z. Yue, A. J. Ellison, P. K. Gupta, D. C. Allan, *Proc. Natl Acad. Sci. USA* **106** (2009) 19780–19784.
- [186] C. Zhang, L. Hu, Y. Z. Yue, J. C. Mauro, *J. Chem. Phys.* **133** (2010) 014508.
- [187] C. Zhou, L. Hu, Q. Sun, H. Zheng, C. Zhang, Y. Z. Yue, *J. Chem. Phys.* **142** (2015) 064508.
- [188] G. Adam, J. H. Gibbs, *J. Chem. Phys.* **43** (1965) 139–146.
- [189] P. K. Gupta, J. C. Mauro, *J. Chem. Phys.* **130** (2009) 094503.
- [190] J. C. Mauro, P. K. Gupta, R. J. Loucks, *J. Chem. Phys.* **130** (2009) 234503.
- [191] J. C. Mauro, R. J. Loucks, *Phys. Rev. E* **78** (2008) 021502.
- [192] R. J. Araujo, J. C. Mauro, *J. Am. Ceram. Soc.* **93** (2010) 1026–1031.
- [193] M. T. Rinke, H. Eckert, *Phys. Chem. Chem. Phys.* **13** (2011) 6552.
- [194] D. Zielniok, C. Cramer, H. Eckert, *Chem. Mater.* **19** (2007) 3162–3170.
- [195] T. Yazawa, K. Kuraoka, T. Akai, U. Norimasa, D. Wei-Fang, *J. Chem. Phys. B* **104** (2000) 2109–2116.

- [196] M. J. Toplis, D. B. Dingwell, K. U. Hess, T. Lenci, *Am. Mineral.* **82** (1997) 979–990.
- [197] J. W. E. Drewitt, L. Hennet, A. Zeidler, S. Jahn, P. S. Salmon, D. R. Neuville, H. E. Fischer, *Phys. Rev. Lett.* **109** (2012) 235501.
- [198] J. W. E. Drewitt, A. C. Barnes, S. Jahn, S. C. Kohn, M. J. Walter, A. N. Novikov, D. R. Neuville, H. E. Fischer, L. Hennet, *Phys. Rev. B* **95** (2017) 064203.
- [199] S. Kohara, K. Suzuya, K. Takeuchi, C.-K. Loong, M. Grimsditch, J. K. R. Weber, J. A. Tangeman, T. S. Key, *Science* (80-. ), vol. 303, no. March, pp. 1649–1652, 2004.
- [200] T. Kasuga, Y. Abe, *J. Non-Cryst. Solids* **243** (1999) 70–74.
- [201] S. Sen, J. Tangeman, *Am. Mineral.* **93** (2008) 946–949.
- [202] M. H. Cohen, D. Turnbull, *Nature* **189** (1961) 131–132.
- [203] S. R. Nagel, J. Tauc, *Phys. Rev. Lett.* **35** (1975) 380–383.
- [204] S. H. Whang, *Mater. Sci. Eng.* **57** (1983) 87–95.
- [205] J. W. P. Schmelzer, *J. Chem. Phys.* **136** (2012) 074512.
- [206] Z. Evenson, T. Schmitt, M. Nicola, I. Gallino, R. Busch, *Acta Mater.* **60** (2012) 4712–4719.
- [207] S. Lan, Y. Ren, X. Y. Wei, B. Wang, E. P. Gilbert, T. Shibayama, S. Watanabe, M. Ohnuma, X.-L. Wang, *Nat. Commun.* **8** (2017) 14679.
- [208] K. Ito, C. T. Moynihan, C. A. Angell, *Nature* **398** (1999) 492–495.
- [209] V. Vasisht, S. Sastry, *Liquid Polymorphism*. Wiley (2013).
- [210] S. Sastry, C. A. Angell, *Nat. Mater.* **2** (2003) 739–743.
- [211] E. A. Jagla, *J. Phys. Condens. Matter* **11** (1999) 10251–10258.
- [212] H. Tanaka, *J. Phys. Condens. Matter* **15** (2003) L703–L711.
- [213] I. Saika-Voivod, F. Sciortino, P. H. Poole, *Phys. Rev. E* **69** (2004) 41503.
- [214] C. Way, P. Wadhwa, R. Busch, *Acta Mater.* **55** (2007) 2977–2983.
- [215] H. W. Sheng, H. Z. Liu, Y. Q. Cheng, J. Wen, P. L. Lee, W. K. Luo, S. D. Shastri, E. Ma, *Nat. Mater.* **6** (2007) 192–197.
- [216] O. Mishima, L. D. Calvert, E. Whalley, *Nature* **314** (1985) 76–78.
- [217] P. F. McMillan, *J. Mater. Chem.* **14** (2004) 1506.
- [218] G. N. Greaves, M. C. Wilding, S. Fearn, D. Langstaff, F. Kargl, S. Cox, Q. V. Van, O. Majérus, C. J. Benmore, R. Weber, C. M. Martin, L. Hennet, *Science* **322** (2008) 566–570.
- [219] L. Hennet, I. Pozdnyakova, A. Bychkov, D. L. Price, G. N. Greaves, M. Wilding, S. Fearn, C. M. Martin, D. Thiaudire, J. F. Brar, N. Boudet, M. L. Saboungi, *J. Chem. Phys.* **126** (2007) 1–5.
- [220] M. T. Cicerone, M. D. Ediger, *J. Chem. Phys.* **103** (1995) 5684–5692.
- [221] A. I. Mel’cuk, R. A. Ramos, H. Gould, W. Klein, R. D. Mountain, *Phys. Rev. Lett.* **75** (1995) 2522–2525.
- [222] E. Vidal Russell, N. E. Israeloff, *Nature* **408** (2000) 695–698.
- [223] L. Hornbøll, Y. Z. Yue, *J. Non-Cryst. Solids* **354** (2008) 350–354.
- [224] L. Hornbøll, T. Knusen, Y. Z. Yue, X. Guo, *Chem. Phys. Lett.* **494** (2010) 37–40.



- [225] Y. Zhang, G. Yang, Y. Z. Yue, *J. Am. Ceram. Soc.* **96** (2013) 3035-3037.
- [226] Y. Z. Yue, *J. Non-Cryst. Solids* **345–346** (2004) 523–527.
- [227] T. D. Bennett, J.-C. Tan, Y. Z. Yue, C. Ducati, N. Terril, H. H. M. Yeung, Z. Zhou, W. Chen, S. Henke, A. K. Cheetham, G. N. Greaves, *Nat. Commun.* **6** (2015) 8079.

ISSN (online): 2446-1636  
ISBN (online): 978-87-7210-137-8

AALBORG UNIVERSITY PRESS